Kinematic Simulation for Turbulent Particle-Laden Flows

KINEMATIC SIMULATION FOR TURBULENT PARTICLE-LADEN FLOWS

BY

STEPHEN A. MURRAY, M.Sc.

A THESIS
SUBMITTED TO THE DEPARTMENT OF MECHANICAL ENGINEERING
AND THE SCHOOL OF GRADUATE STUDIES
OF MCMASTER UNIVERSITY
IN PARTIAL FULFILMENT OF THE REQUIREMENTS
FOR THE DEGREE OF
DOCTOR OF PHILOSOPHY

Doctor of Philosophy (2016) McMaster University
(Mechanical Engineering) Hamilton, Ontario, Canada

TITLE: Kinematic Simulation for Turbulent Particle-Laden Flows

AUTHOR: Stephen A. Murray
M.Sc. (Mathematics & Statistics)
McMaster University, Hamilton, Ontario, Canada
B.Sc. (Mathematics & Computer Science)
Mount Allison University, Sackville, New Brunswick, Canada

SUPERVISOR: Dr. Marilyn Lightstone and Dr. Stephen Tullis

NUMBER OF PAGES: xxi, 128

To my parents, for their many years of unwavering support

Abstract

Kinematic simulation (KS) is a means of generating a turbulent-like velocity field, in a manner that enforces an input Eulerian energy spectrum. Such models have also been applied in particle-laden flows, due to their ability to enforce spatial organization of the fluid velocity field when simulating the trajectories of individual particles. A critical evaluation of KS is presented; in particular, its ability to reproduce single-particle Lagrangian statistics is examined. Also the ability of KS to reproduce the preferential concentration of inertial particles is explored. Some numerical results are presented, in which fluid tracers and inertial particles are transported alternatively by (1) simulated turbulence generated by direct numerical simulation (DNS) of the incompressible Navier-Stokes equations, and (2) KS. The effect of unsteadiness formulation in particular is examined. It is found that even steady KS qualitatively reproduces the continuity effect, clustering of inertial particles, elevated dispersion of inertial particles and the intermittent turbulence velocity signal. A novel method is then motivated and formulated, in which, for input RANS parameters, a simulated spectrum is used to generate a KS field which enforces a target Lagrangian timescale. This method is then tested against an existing experimental benchmark, and good agreement is obtained.

0.1 Acknowledgements

I would like to acknowledge:

- My supervisors, Dr. M. F. Lightstone, and Dr. S. Tullis
- The Natural Sciences and Engineering Research Council of Canada, for financial support
- Compute Canada and the Shared Hierarchical Academic Research Computing Network (SHARCNet) for the provision of high-performance computing facilities and support
- My former colleagues, Matthew Cernick and Cathy Strutt, for their work on the particle tracking tools
- Dr. Nicholas Kevlahan (McMaster), for the provision of the parallelized DNS distribution
- Dr. Diego Ayala (Michigan) and Dr. Sergey Mashchenko (McMaster), for their assistance with the operation of the DNS distribution on the SHARCNet architecture

Notation and Abbreviations

Acronyms

CTE	Crossing trajectories effect
DNS	Direct numerical simulation
KS	Kinematic simulation
RANS	Reynolds-average Navier-Stokes
SSF	Stochastic separated flow
TLKS	Target Lagrangian integral timescale Kinematic Simulation

Roman letters

B_{ij}	Large-scale anisotropy tensor
C	Courant number
$\mathcal{D}_2$	Correlation dimension
$\overline{\mathcal{D}_2}$	Asymptotic correlation dimension
$E(\kappa)$	Eulerian energy spectrum
$\mathscr{E}(\kappa)$	Cumulative distribution of energy in spectral space
$f(r)$	Lateral Eulerian two-point velocity autocorrelation
$g(r)$	Longitudinal Eulerian two-point velocity autocorrelation
k	Turbulent kinetic energy
L	DNS domain length
L_E, L_{11}	Integral length scale
N_κ	Number of KS modes
$R_{ij}^E(\mathbf{r}, \tau)$	Eulerian velocity autocorrelation tensor
$R_{ij}^L(\tau)$	Lagrangian velocity autocorrelation tensor
Re	Taylor-scale Reynolds number
$S^E(r)$	Eulerian second-order structure function of velocity
$S^L(\tau)$	Lagrangian second-order structure function of velocity
St	Stokes number
T_L	Lagrangian integral timescale
t	Time
$\mathbf{u}_f$	Fluid velocity
$\mathbf{u}_p$	Particle velocity
u_{rms}	Root mean squared turbulent fluctuating velocity
$\mathbf{x}_p$	Particle position

Greek letters

γ_u	Skewness of velocity field
Δt	Time step
ϵ	Energy dissipation
η	Kolmogorov length scale
κ	Wavenumber in spectral space
κ_n	Sequence of wavenumbers used in kinematic simulation
$\tilde{\kappa}_1$	Lowest wavenumber of input spectrum for Target-Lagrangian integral timescale Kinematic Simulation
$\tilde{\kappa}_N$	Highest wavenumber of input spectrum for Target-Lagrangian integral timescale Kinematic Simulation
λ	Unsteadiness parameter in KS
μ	Dynamic viscosity
ν	Kinematic viscosity
ρ_f	Fluid density
ρ_p	Particle density
τ_η	Kolmogorov timescale
τ_p	Particle relaxation time
ω_n	"Turnover" frequency of the n-th KS mode

Diacritics and brackets

$\langle \ \rangle$	The spatial average (in the Eulerian frame of reference), and over the ensemble of realizations OR average over particle locations (in the Lagrangian frame of reference), and over the ensemble of realizations
[ ]	Average over ensemble of realizations
$\hat{()}$	Fourier transform

Contents

Contents

List of Figures

Chapter 1

Introduction

1.1 Background and objectives

Particle-laden flows are a class of two-phase flows in which one of the phases is a continuously connected fluid, and the other phase is comprised of small, immiscible, dilute particles dispersed throughout the fluid. The modelling of turbulent particle-laden flows can be applied to a tremendous range of phenomena of environmental and industrial interest, such as the dispersion of pollutants in the atmosphere, fluidization and turbulent mixing in combustion processes, deposition of medicinal aerosols in the human body, processing and transport of liquid/solid nuclear waste and water droplet formation within clouds. Many physical/chemical processes depend upon the transport and clustering properties of the dispersed species, hence the utility of computational models of these processes depends on the ability to reproduce preferential concentration and dispersion.

Even single-phase turbulent flows pose enormous challenges for researchers; the nonlinearity of the governing Navier-Stokes equations renders them resistant to analytical treatments. In practice, filtered or averaged equations are solved (with appropriate closure models) to achieve a reasonable computational cost. These difficulties are exacerbated with the addition of a particle phase, since a balance must be sought in simulating the turbulence in a manner which is computationally tractable, but does not sacrifice the detailed, spatially and temporally-correlated information that is "seen" by the dispersed particles. If the particles are treated in the Lagrangian frame of reference, and if the only fluid information available is the time-averaged statistics (as in the Reynolds-averaged Navier-Stokes (RANS) context), one can stochastically generate a history of correlated fluid velocities seen by individual particles, (via a discretized solution of a governing stochastic differential equation) in a manner which reflects these statistics - this information is then used to integrate the (Lagrangian) momentum equation to simulate an individual particle trajectory. This algorithm is applied to a whole ensemble of computational dispersed particles. Such methods are known as stochastic separated flow (SSF) models (Gosman & Ioannides (1983); MacInnes & Bracco (1992)).

SSF approaches, however, lack the ability to reproduce key hallmarks of *turbulence structure* in a comprehensive manner (this is addressed in detail in Sec. 2.2.3). A potential alternative method of enforcing spatial structure of the turbulence is to stochastically generate an entire turbulent-like flow field (rather than synthesizing velocities independently for each particle), in a manner which reflects the expected Eulerian second-order statistics - this is the idea behind kinematic simulation (KS), a method which has its foundation in the work of Kraichnan (1970) and Fung *et al.*

(1992), and has since attracted much attention from both pure and applied fluid dynamicists. While there exists a body of literature in which the Lagrangian properties of KS turbulent-like flows are examined, its applicability to fundamentally important features of particle dynamics (*single-particle* dispersion, as well as clustering), along with its potential utility as a complement to RANS treatments, have received little attention.

The specific questions addressed here are:

- If realistic Eulerian second-order statistics are known, to what extent does KS reproduce the single-particle Lagrangian properties of turbulence, the Lagrangian properties of inertial particles (in particular in the presence of gravity), and the clustering properties of inertial particles? In particular, what is the effect of the unsteadiness formalism in KS?
- Can a link between Eulerian and Lagrangian statistics of KS be formalized? If so, does this hold any utility as a complement to RANS treatments of particle-laden flows?

1.2 Thesis outline

The thesis is structured as follows: in Chapter 2, the appropriate background material and literature review are presented. In Chapter 3, the methodology for the comparison between KS and direct numerical simulation is given, the results of which are given in Chapter 4. In Chapter 5, a novel link between Eulerian and Lagrangian properties of KS are established, and a methodology for a new Target Lagrangian integral timescale Kinematic Simulation (TLKS) is proposed. Also in Chapter 5, the TLKS method is tested against the experimental benchmark of Snyder & Lumley (1971). A summary of interpretations of the results, along with suggestions for future work, are given in Chapter 6.

Chapter 2

Background and Literature Review

2.1 Fluid phase

2.1.1 Governing fluid equations

The fluid dynamics are assumed to be governed by the traditional incompressible Navier Stokes equations:

$$\begin{aligned} \frac{\partial \mathbf{u}}{\partial t} + \mathbf{u} \cdot \nabla \mathbf{u} &= -\frac{1}{\rho} \nabla p + \nu \Delta \mathbf{u} \\ \nabla \cdot \mathbf{u} &= 0 \end{aligned} \tag{2.1}$$

Hence to model a fluid, these nonlinear partial differential equations must be appropriately rendered as a system of (algebraic) linear equations, whose rank scales as the number of grid points. A time-stepping numerical method (with sufficient resolution in space and in time to ensure stability and convergence) is called *direct numerical simulation* (DNS). However real turbulence encompasses a large range of length/timescales, and for many real-world (high Reynolds-number) applications, treatment with DNS remains far out of reach, even with today's best supercomputers.

Fortunately there exist alternatives to DNS; in *turbulence modelling*, one employs known statistical symmetries of real turbulence to reduce a given problem to that of finding a solution of the filtered or averaged Navier-Stokes equations. A common class of methods is the previously-mentioned RANS, in which a time-averaged version of (2.1) is modelled. In a widely applied sub-class of such models, the transport of turbulent kinetic energy (k) and its dissipation (ϵ) are modelled, which can in turn be used as inputs for particle modelling (as seen in Sec. 2.2.3).

2.2 Particle phase

2.2.1 Eulerian treatment of particle phase

The dispersed phase can be treated in either the Eulerian or Lagrangian framework. In the Eulerian framework, the particle phase is treated as a continuum, for which a transport equation of the scalar quantity Φ (local particle concentration) is assumed (as in Elghobashi (1994)):

$$\frac{\partial}{\partial t}(\Phi_p \rho_p) + \nabla \cdot (\rho_p \Phi_p \mathbf{u}_p) = 0 \tag{2.2}$$

$$\frac{D}{Dt}(\rho_p \Phi_p \mathbf{u}_p) = \nabla \cdot (\Phi_p \underline{\underline{\tau}}) + \rho_p \Phi_p \mathbf{g} \tag{2.3}$$

where ρ_p, $\mathbf{u}_p$ and $\underline{\underline{\tau}}$ represent the particle density, local particle velocity and "particle stress tensor" respectively. In other words, the particle phase is itself treated as a fluid.

Eulerian particle models bear the advantage of low computational cost, and they allow the particle statistics to be readily determined at a given location. Also, the interaction between the fluid and particle phases can be easily accommodated by the inclusion of momentum source/sink terms. These models are often applied to the modelling of low-inertia particles, such as in indoor pollutant modelling (Murakami *et al.* (1992), Posner *et al.* (2005), Zhao *et al.* (2005) and Zhao *et al.* (2008)).

However for heavier inertial particles, it then becomes necessary to resort to a great deal of empiricisms in order to determine an appropriate effective particle diffusivity, and in order to model the higher order terms which result from averaging. Even if this were achieved, gradient diffusion schemes - which are typically used to model higher order terms - are unable to account for inertia (Elghobashi (1994)). In addition, such approaches fail to capture the multifractal nature of particle clustering (Bec (2005)). Consequently such an approach is avoided here.

2.2.2 Lagrangian treatment of particle phase

Particles can be treated in the Lagrangian framework, in which the dynamics are analyzed from the point of view of an individual particle, rather than fixed positions in space. In realistic scenarios, one must track a large number of trajectories, in order to recover meaningful ensemble statistics, which renders such an approach generally more computationally expensive than its Eulerian counterpart, though it avoids the unphysical assumptions that underpin "diffusive" transport. The Lagrangian position equation for a given particle is:

$$\frac{d\mathbf{x}_p}{dt} = \mathbf{u}_p \tag{2.4}$$

where $\mathbf{x}_p$ and $\mathbf{u}_p$ respectively refer to the position and velocity of a particle. For a passively advected particle (like a fluid tracer), the velocity is simply recovered from the (directly numerically simulated or modelled) fluid velocity field, via an appropriate interpolation scheme. For an inertial particle (whose density differs from the fluid which contains it), its acceleration is proportional to a variety of forces acting upon it, the formulation of which is the subject of an expansive body of literature (Basset (1888), Boussinesq (1903), Oseen (1927), Tchen (1947), Corrsin & Lumley (1956), Buevich (1966), Maxey & Riley (1983)). The following is the general inertial particle momentum equation, along with the interpretation of the various terms (as given by Elghobashi & Trusedell (1992)):

$$\begin{aligned} m_p \frac{d\mathbf{u}_p}{dt} =& m_f \frac{D\mathbf{u}_f}{Dt} && \text{(force due to pressure gradient and viscous stresses)} \\ &+ \frac{m_f}{2}\Big(\frac{D\mathbf{u}_f}{Dt} - \frac{d\mathbf{u}_p}{dt}\Big) && \text{(added or “virtual” mass)} \\ &+ m_p \frac{f}{\tau_p}(\mathbf{u}_f - \mathbf{u}_p) && \text{(modified Stokes drag)} \\ &+ \frac{3}{2} d_p^2 \sqrt{\pi \rho_f \mu_f} \int_{-\infty}^{t} \frac{\frac{d}{d\tau}(\mathbf{u}_f - \mathbf{u}_p)}{\sqrt{t-\tau}}\, d\tau && \text{(Basset (history) force)} \\ &+ m_p \mathbf{F} && \text{(body force)} \end{aligned} \tag{2.5}$$

the variables have the following interpretations:

Parameter	Interpretation
m_p	particle mass
m_f	mass of displaced fluid
d_p	particle diameter
μ	fluid dynamic viscosity
$\mathbf{F}$	body force (typically due to gravity)
$\mathbf{u}_f$	fluid velocity
$\mathbf{u}_p$	particle velocity

In the Stokes' drag term of (2.5), τ_p is given as:

$$\tau_p = \frac{d_p^2}{18\nu}\frac{\rho_p}{\rho_f} \tag{2.6}$$

and is referred to as the *particle relaxation time.* This quantity is a timescale of the particle's reaction to changes in the fluid velocity field. Also in the Stokes drag term, f is given as

$$f = 1 + 0.15Re_p^{0.687} \tag{2.7}$$

and represents a high Reynolds number correction (Clift *et al.* (1978)), in which Re_p, the particle Reynolds number, is defined as:

$$Re_p = \frac{d_p|\mathbf{u}_f - \mathbf{u}_p|}{\nu} \tag{2.8}$$

For many practical purposes, in which the density of the particles greatly exceeds that of the fluid (which will be assumed here), only the forces due to Stokes drag and gravity are retained (Maxey & Riley (1983), Mei *et al.* (1991), Armenio & Fiorotto

(2001)), which yields a simplified momentum equation:

$$\frac{d}{dt}\mathbf{u}_p(t) = \frac{f}{\tau_p}\big(\mathbf{u}_f(\mathbf{x}_p(t), t)) - \mathbf{u}_p(t)\big) + \mathbf{F} \tag{2.9}$$

A parameter of interest, which will be encountered later, is the *Stokes number*, defined as:

$$St = \frac{\tau_p}{\tau_\eta} \tag{2.10}$$

where τ_η is the *Kolmogorov timescale*, that is, the smallest length scale of the turbulent cascade. The interface between the (modelled or directly simulated) flow field and the inertial particle motion is given by the fluid velocity at the inertial particle location, $\mathbf{u}_f(\mathbf{x}_p(t), t)$, and is seen in the drag term of (2.5).

Broadly speaking, inertial particles can either dissipate or enhance the fluid turbulence, depending on their size and mass loading. If the fluid influences the particles, and vice versa, this is referred to as *two-way coupling*. If the fluid influences the particles and the opposite is not true (which can be assumed if the particles are sufficiently small and dilute (Elghobashi (1994))), then one has *one-way coupling* - this will be assumed throughout this investigation. In addition, the particle phase is assumed to be sufficiently dilute, such that particle collisions can be neglected.

2.2.3 Particle modelling within a RANS context

A great deal of particle-laden flow modelling occurs in flows for which only the time-averaged fluid information is given. Mathematically, a RANS decomposition is given as $\mathbf{u}_f = \overline{\mathbf{u}}_f + \mathbf{u}'_f$, where $\overline{\mathbf{u}}_f$ is the mean velocity (given from the RANS solution) and $\mathbf{u}'_f$ is the fluctuating velocity, which must in turn be modelled. In SSF models, the trajectories of individual Lagrangian particles are simulated via the integration of an appropriately formulated stochastic differential equation, which constructs an appropriate distribution of $\mathbf{u}'_f$ over the particle ensemble.

For example, a widely applied variety of SSF employs the Langevin equation (Thomson (1984); Bocksell & Loth (2006); Dehbi (2011)):

$$d\mathbf{u}_f = -\frac{\mathbf{u}_f}{T}dt + d\boldsymbol{\xi}(t) \tag{2.11}$$

where $\boldsymbol{\xi}$ is a random function (with appropriate moments, such that the expected variance of the random variable $\mathbf{u}_f$ is enfroced), and T is an appropriate timescale of the decorrelation of fluid velocities (often assumed to be the Lagrangian integral timescale, defined in Sec. 2.2.5). To resolve the trajectory of an individual Lagrangian particle, a discretized version of (2.11) is solved, say:

$$\mathbf{u}_f(t + \Delta t) = R(\Delta t)\mathbf{u}_f(t) + \boldsymbol{\eta} \tag{2.12}$$

where $R(t) = \exp(-\Delta t/T)$, and $\boldsymbol{\eta}$ is a random variable with variance $(1 - R(\Delta t))^2$. Despite the widespread application of such models, there exists a number of significant drawbacks:

- As is inevitably the case with models, one is presented with dilemmas regarding which physically realistic aspects of particle transport one wishes to reproduce. For instance, one must choose to either satisfy a well-mixed condition, or forcing with the appropriate higher-order moments to ensure an appropriate distribution of particle velocities (Thomson (1984, 1987)).

- The treatment of particle velocity histories as random processes may not be applicable in real turbulence (Thomson (1987)). In particular, inertial particles drifting through real turbulence exhibit a certain "memory" of the spatial structure, which manifests itself in the Lagrangian statistics - for example, the continuity effect (defined in Sec. 2.2.5). Various authors have proposed modifications to recreate, in some sense, this impact on Lagrangian statistics (Lu *et al.* (1993); Wang & Stock (1993); Oesterlé & Zaichik (2004); Hennick & Lightstone (2000)), while appealing to heuristic arguments about the expected behaviour of particle statistics in certain situations. Such models have been modestly successful. Notwithstanding, the distribution and temporal structure of turbulent-like velocities arising from random processes only approximately conform to the properties of real turbulence (Thomson (1984); Lightstone (2007)).

- Each particle experiences a unique and independent series of simulated turbulent fluid velocities, generated from something like (2.12). Thus a given particle does not "know" what another particle sees, even if they are very close to one another, hence any type of sensible *spatial correlation*, and consequently preferential concentration, cannot be reproduced by such methods.

The difficulty in reproducing realistic particle behaviour is often attributed to the inability of SSF models to reproduce turbulence *structure* - such a statement merits some unpacking. What properties of an ensemble of Lagrangian particles are a result of "turbulence structure", and which are not? Of course there does not exist "structure"-less turbulence, so the meaning of this statement is not immediately evident. The foundation of stochastic Lagrangian treatments of particle motion is the representation of particle velocities as random variables. The properties of these random variables should, in a sense, conform to properties of corresponding Eulerian random variables, which are assumed to characterize the turbulent flow - but it certainly cannot be said that this is the *raison d'être* of such models. Indeed the point of stochastic Lagrangian models is to achieve results that simpler models cannot; in particular, the *correlation* between the random variables, and all statistics for which the correlation is the foundation. "Structure" is interpreted is being manifested in the timescales of such correlations, and the only arbiter for the robustness of a particular stochastic Lagrangian model is whether or not structure - in this sense - is reproduced.

2.2.4 Kinematic simulation

Rather than surmising a relationship between velocity random variables underpinned by *Lagrangian* autocorrelations, as is done in SSF models, the particle velocity histories can be implicitly related to an underlying stochastically-generated flow field, in a manner that enforces, in a sense, the appropriate *Eulerian* autocorrelations. An illustration of KS and SSF is given in Fig. 2.1. Fortunately, the behaviour of the Eulerian second-order statistics in turbulence is well-documented; in particular, the Eulerian energy spectrum is known to exhibit a universal behaviour over the inertial range of scales, due to the self-similar transfer of energy from larger to smaller eddies (see Fig. 2.2). It is emphasized that KS is still a stochastic Lagrangian model; when the trajectory of a given particle is simulated, the turbulent-like field is reconstructed only at the particle location.

A KS field is constructed by summing randomly oriented sines and cosines of varying spatial scales, and whose amplitudes are determined by this input spectrum

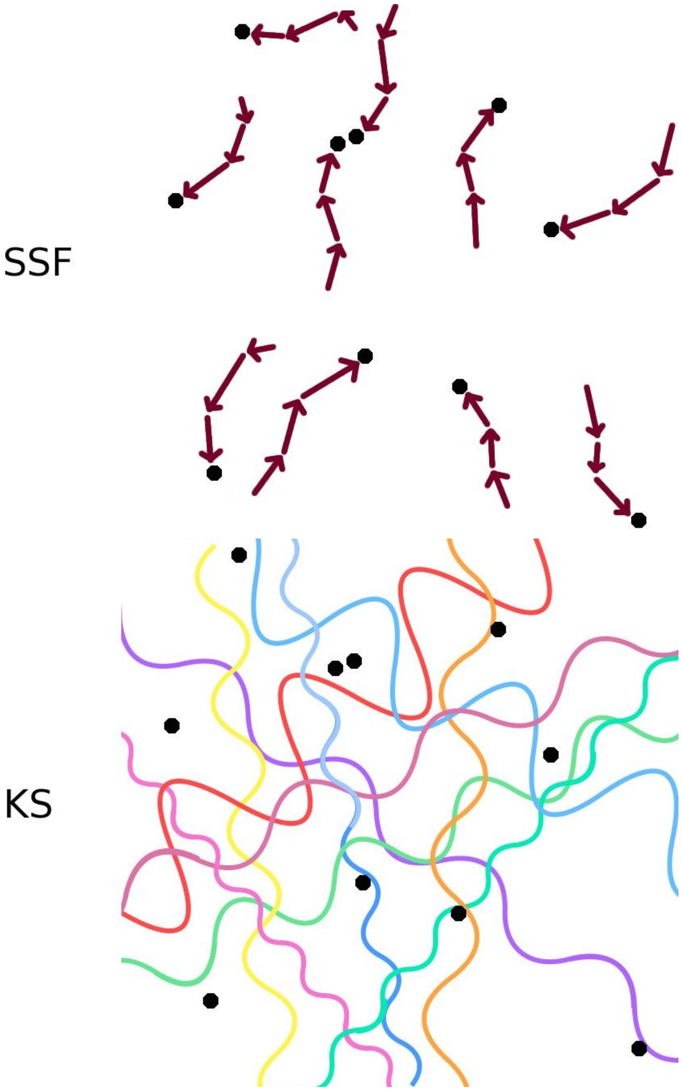

Figure 2.1: An ensemble of particles, transported by two alternative methods of simulating the turbulent flow that contains them. In the top panel, the chains of arrows represent histories of the simulated turbulent fluctuating velocity. The processes for generating these velocities are independent for each particle, so particles can experience very different "turbulent" fluid velocities, even if they are very close to one another. In the bottom panel, turbulent-like velocity vector fields are reconstructed via summation of trigonometric functions (which are referred to here as KS modes) of varying wavelengths, amplitudes and orientations. For the purpose of visualization, they are here depicted as waves, though in fact they are defined on an entire 3D domain. The simulated velocities are reconstructed from the summation of KS modes only at the particle locations, for the purpose of simulating Lagrangian particle transport.

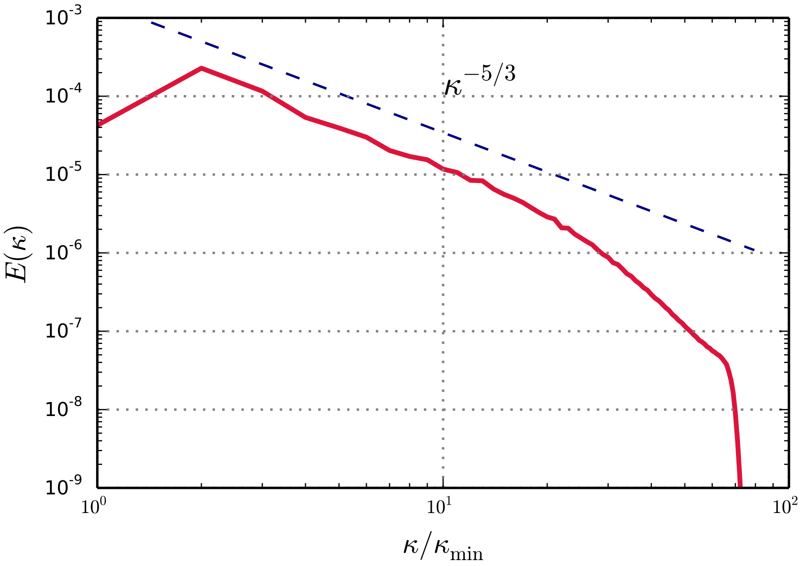

Figure 2.2: A typical Eulerian energy spectrum for homogeneous, isotropic turbulence in a periodic domain (taken from a DNS, described in Sec. 3.1)

- this is akin to the manner in which a physical-space field is reconstructed from its Fourier series. While there exist slight variations of KS techniques (which is discussed in further detail in Sec. B.1), this investigation will adhere to a commonly applied version in which the energy is enforced in every KS realization: (as in Thomson & Devenish (2005); Nicolleau & Abou El-Azm Aly (2012)):

$$\mathbf{u}_f(\mathbf{x},t) = \sum_{n=1}^{N_\kappa} \mathbf{a}_n \cos(\boldsymbol{\kappa}_n \cdot \mathbf{x} + \omega_n t) + \mathbf{b}_n \sin(\boldsymbol{\kappa}_n \cdot \mathbf{x} + \omega_n t) \tag{2.13}$$

where the $\boldsymbol{\kappa}_n$ are randomly sampled vectors, whose orientations are uniformly distributed over a sphere. Also $\mathbf{a}_n$ and $\mathbf{b}_n$ are chosen with random orientations, but under the constraint that they be perpendicular to $\boldsymbol{\kappa}_n$:

$$\mathbf{a}_n \cdot \boldsymbol{\kappa}_n = 0 \text{ and } \mathbf{b}_n \cdot \boldsymbol{\kappa}_n = 0 \text{ for all } n \tag{2.14}$$

Also $|\boldsymbol{\kappa}_n| = \kappa_n$, where κ_n is the sequence of N_κ wavenumbers for which the spectrum is given. Consequently $E(\kappa_n)$ is the sequence of corresponding energy density values. The magnitudes of the vectors $\mathbf{a}_n$ and $\mathbf{b}_n$ should be chosen such that the appropriate energy density at each particular scale is enforced:

$$|\mathbf{a}_n|^2 = |\mathbf{b}_n|^2 = 2E(\kappa_n)\Delta\kappa_n \tag{2.15}$$

where $\Delta\kappa_n$ is the interval width associated with the wavenumber κ_n (See Sec. B.2 for a derivation of (2.15)). In the literature, $\Delta\kappa_n$ is commonly given as

$$\Delta\kappa_n = \begin{cases} \frac{\kappa_{n+1}-\kappa_n}{2} & \text{if } n = 1 \\ \frac{\kappa_{n+1}-\kappa_{n-1}}{2} & \text{if } 2 \leq n \leq N_\kappa - 1 \\ \frac{\kappa_n-\kappa_{n-1}}{2} & \text{if } n = N_\kappa \end{cases} \tag{2.16}$$

The given sequence of wavenumbers, κ_n, can be algebraic, geometric, or arithmetic - in any case the sequence should be sufficiently dense such that no mode (with a given orientation) dominates, and such that each dimensional component of the turbulent-like field enforces the appropriate fluctuating velocity. The definition of the term ω_n is somewhat open to interpretation, but it is generally meant to enforce the unsteadiness of the turbulence - this is discussed in further detail in Sec. 2.3.1.

2.2.5 Lagrangian statistics

Much literature has focused on whether KS can reproduce *pairwise dispersion* of fluid particles, defined as:

$$\langle|\Delta\mathbf{l}(t)|^2\rangle \tag{2.17}$$

where $\Delta\mathbf{l}(t) = \mathbf{l}(t) - \mathbf{l}(0)$, and $\mathbf{l}(t) = \mathbf{x}_p^{(1)}(t) - \mathbf{x}_p^{(2)}(t)$, with each $\mathbf{x}^{(1)}$ and $\mathbf{x}^{(2)}$ referring to the positions of a particular particle pair with some imposed initial separation l_0, which gives $|\Delta\mathbf{l}(0)| = |\mathbf{x}_p^{(1)}(0) - \mathbf{x}_p^{(2)}(0)| = l_0$. In this area, some results have reproduced good agreement with either benchmark DNS's and/or theoretical scaling relations (Malik (1996); Malik & Vassilicos (1999); Nicolleau & Vassilicos (2003); Nicolleau & Abou El-Azm Aly (2012)), however this topic is not without controversy, with others disputing the ability to reproduce key benchmark scale relations, notably Richardson's law of pairwise dispersion (Thomson & Devenish (2005); Eyink & Benveniste (2012)).

The scope of this investigation will encompass *single-particle Lagrangian statistics*, in particular *single-particle dispersion*, or simply *dispersion*. This is defined as the mean-squared displacement from the initial particle position. Mathematically, the i-th component of displacement from initial position is defined as:

$$y_{p,i}(\tau) = x_{p,i}(t+\tau) - x_{p,i}(t) \tag{2.18}$$

the mean-corrected displacement from initial position will be denoted as $Y_{p,i}(\tau)$:

$$Y_{p,i}(\tau) = y_{p,i}(\tau) - \langle y_{p,i}(\tau)\rangle \tag{2.19}$$

where $\langle\cdot\rangle$ denotes the average over an ensemble of particles, and over the ensemble of flow realizations. "Dispersion" will refer to the mean square of this quantity, or the variance of displacement from initial position:

$$\langle Y_{p,i}^2(\tau)\rangle = \left\langle \big(y_{p,i}(\tau) - \langle y_{p,i}(\tau)\rangle\big)^2 \right\rangle \tag{2.20}$$

Closely linked to dispersion is the *Lagrangian velocity autocorrelation* tensor:

$$R^L_{ij}(\tau) = \frac{\langle u_{p,i}(\mathbf{x}_p(t),t)u_{p,j}(\mathbf{x}_p(t+\tau),t+\tau)\rangle}{\sqrt{\langle (u_{p,i}(\mathbf{x}_p(t),t))^2\rangle}\sqrt{\langle (u_{p,j}(\mathbf{x}_p(t+\tau),t+\tau))^2\rangle}} \tag{2.21}$$

Here, u_i is the i-th component of the particle velocity vector $\mathbf{u}_p$. When no significant difference is expected between the diagonal components of R^L_{ij}, the related scalar quantity, R^L, will be employed, which is defined with inner products:

$$R^L(\tau) = \frac{\langle \mathbf{u}_p(t+\tau)\cdot\mathbf{u}_p(t)\rangle}{\sqrt{\langle |\mathbf{u}_p(t+\tau)|^2\rangle}\sqrt{\langle |\mathbf{u}_p(t)|^2\rangle}} \tag{2.22}$$

and similarly for all subsequently defined Lagrangian statistics. As proven in the classical work of Taylor (1921), the relationship between the autocorrelation and dispersion is given as:

$$\frac{d}{d\tau}\langle Y^2_{p,i}(\tau)\rangle = 2\langle u^2_{p,i}\rangle \int_0^\tau R^L_{ii}(\tau')\,d\tau' \tag{2.23}$$

For long times, the previous equation reduces to:

$$\Lambda_i(\tau) = \langle u^2_{p,i}\rangle T_{L_i} \tag{2.24}$$

where $\Lambda_i(\tau) = \frac{1}{2}\frac{d}{d\tau}\langle y^2_{p,i}(\tau)\rangle$ is the *diffusivity*, and T_{L_i}, the *Lagrangian integral timescale*, is defined as:

$$T_{L_i} = \int_0^\infty R^L_{ii}(\tau)\,d\tau \tag{2.25}$$

where the double appearance of the i subscript does not imply summation, rather the diagonal components of the autocorrelation tensor.

Closely linked to the autocorrelation tensor is the *structure function tensor*, defined as:

$$S_{ij}^L(\tau) = \Big\langle \big(u_{p,i}(\mathbf{x}_p(t+\tau), t+\tau) - u_{p,j}(\mathbf{x}_p(t), t)\big)^2 \Big\rangle \tag{2.26}$$

For homogenous, stationary turbulence, this relates to $R^L(\tau)$ as:

$$S_{ii}^L(\tau) = 2\langle u_{p,i}^2 \rangle \big(1 - R_{ii}^L(\tau)\big) \tag{2.27}$$

Also of interest is the *Lagrangian frequency spectrum*, $\Phi^L(\omega)$, which is related to the autocorrelation as:

$$\Phi_i^L(\omega) = \langle u_{p,i}^2 \rangle \int_0^\infty R_{ii}^L(s) e^{-i\omega s}\, ds \tag{2.28}$$

Further information is revealed in even higher order moments of the Lagrangian velocity signal, such as the *flatness* tensor, defined as:

$$F_{ij}^L(\tau) = \frac{\Big\langle \big(u_{p,i}(\mathbf{x}_p(t), t) - u_{p,j}(\mathbf{x}_p(t+\tau), t+\tau)\big)^4 \Big\rangle}{\Big\langle (u_{p,i}(\mathbf{x}_p(t), t) - u_{p,j}(\mathbf{x}_p(t+\tau), t+\tau))^2 \Big\rangle^2} \tag{2.29}$$

An important property of real turbulence is that it is intermittent, which, following Frisch (1995), occurs when a diagonal component of F increases above the Gaussian value of 3, as τ approaches 0. Loosely speaking, intermittency occurs when the mechanism of dispersion occurs in punctuated bursts, interspersed with periods over which particles exhibit relatively straight trajectories.

Crossing trajectories and continuity effects

In the Lagrangian treatment of the dispersed phase, it is assumed that a given inertial particle will tend to follow a different pathline than the collocated fluid particle at

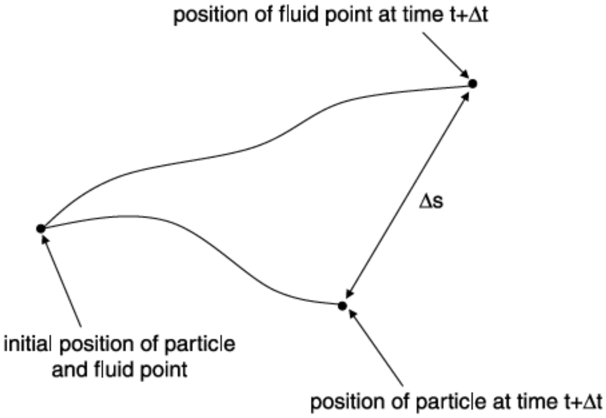

Figure 2.3: Illustration of the trajectories of inertial and fluid particles. Image reproduced from Lightstone (2007)

any given time (see Fig. 2.3). Mathematically, in general:

$$\mathbf{u}_f(\mathbf{x},t) \neq \mathbf{u}_p(\mathbf{x}_p(t),t) \tag{2.30}$$

The *Lagrangian autocorrelation of fluid velocities conditioned at inertial particle locations* is defined as:

$$R_{ij}^{f|p}(\tau) = \frac{\langle u_{f,i}(\mathbf{x}_p(t),t)u_{f,j}(\mathbf{x}_p(t+\tau),t+\tau)\rangle}{\sqrt{\langle (u_{f,i}(\mathbf{x}_p(t),t))^2\rangle}\sqrt{\langle (u_{f,j}(\mathbf{x}_p(t+\tau),t+\tau))^2\rangle}} \tag{2.31}$$

and for inertial particles, this quantity is nontrivially related to R^L - indeed an analytical link was proven in Csanady (1963). It has been observed (Reeks (1977)) that the effect of particle inertia, for drifting particles, is to accelerate the decay of $R^{f|p}$ (and also R^L), which in turn reduces dispersion - this is the *crossing trajectories effect* (CTE). There exists an important manifestation of the CTE; when inertial particles are subjected to a sufficiently strong body force, and exhibit a high mean drift. As a particle moves through an eddy, it tends to see a turbulent velocity, shortly followed

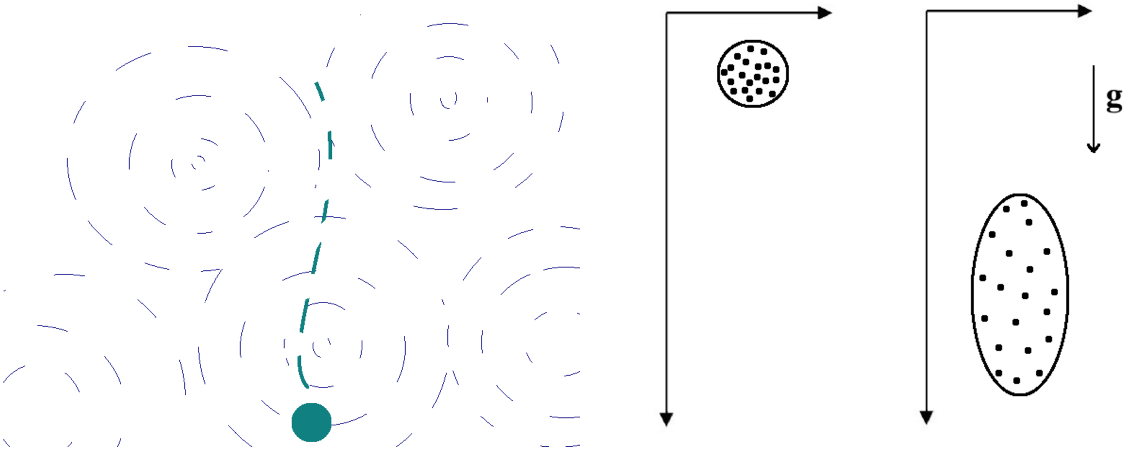

Figure 2.4: Left: A downward-drifting inertial particle experiences a turbulent velocity, then its reverse as it traverses an eddy. Right: This manifests itself in the reduction of dispersion in the direction perpendicular to the mean drift, relative to the parallel with the mean drift. The gravity vector is indicated by **g**. Image adapted form Cernick (2013).

by its opposing “backflow” counterpart within the same eddy - a manifestation of the incompressibility of the fluid. Hence inertial particle dispersion is reduced in the direction perpendicular to the mean drift, compared with parallel to the mean drift - this is the *continuity effect* (see Fig. 2.4). This phenomenon has been predicted analytically (Townsend (1980); Csanady (1963)) and has been observed experimentally (Wells & Stock (1983)) and numerically (Elghobashi & Trusedell (1992)). For a sufficiently high drift velocity, the lateral diffusivity can be reduced to half the longitudinal diffusivity: $\Lambda_{\perp} \approx \frac{1}{2}\Lambda_{\parallel}$.

2.2.6 Structure of particle ensemble

Also of great interest in particle-laden flows research is clustering phenomena, since many natural phenomena are dependent upon the local concentration of the particle ensemble. Naturally if one wishes to reproduce this structure appropriately, it seems necessary to recreate the appropriate structure of the fluid field, complete with eddying, streaming and straining regions - and KS has been demonstrated to (qualitatively) achieve this (Fung *et al.* (1992); Fung & Vassilicos (1998)), though the length of vortex filaments is underpredicted.

A word of caution is required when discussing “structure” of the particle phase: when the particle phase is treated as an ensemble of points in the Lagrangian frame of reference, an appropriate manner of translating their (gridless) positions into a temporally (and spatially) varying concentration distribution is not entirely straightforward. Often in the KS literature, “structure” is discussed within the context of the Fokker-Planck transport mechanism for pairwise Lagrangian statistics (as mentioned in Flohr & Vassilicos (2000)), though this may offer an incomplete picture in some scenarios, primarily for three reasons:

- This link is commonly employed for a subgrid complement to the convection-diffusion equation of the particle phase; a treatment which might not be suitable, especially for heavier inertial particles (Shotorban & Balachandar (2007)), as was discussed in Sec. 2.2.1.

- The bridge between concentration variance and pairwise dispersion is constructed with highly nonlocal information (as noted in Flohr & Vassilicos (2000)), thus limiting the scope of applicability of such an analysis to stationary, homogeneous flows.

- Appeal to the Fokker-Planck mechanism employs the *box index* definition of concentration, (see Chen *et al.* (2006)) which is sensitive to the choice of box size. In practice, particle clusters can exhibit nontrivial multi-scale behaviour (Bec (2005)).

In this study, preferential concentration is quantified by the *correlation dimension*, a scale-independent metric extensively applied in dissipative dynamical systems theory (Grassberger & Procaccia (2004); Monchaux *et al.* (2012)). This dimensionless quantity describes, loosely speaking, the extent to which the particle phase is space-filling. More rigorously, it is given by:

$$\mathcal{D}_2 = \lim_{r \to 0} \frac{d \log(P_2(r))}{d \log(r)} \tag{2.32}$$

where $P_2(r)$ is a measure of the number of particles within r of one another (hence it is a cumulative distribution function). If particles are uniformly distributed in three-dimensional space, then $\mathcal{D}_2 = 3$, whereas if they are uniformly distributed along a plane, then $\mathcal{D}_2 = 2$. For inertial particles in turbulence, this quantity is expected to settle between 2 and 3, which can be interpreted as resulting from the localized clustering of particles into "sheet"-like structures.

The structure of an ensemble of particles is known to exhibit *dissipative* dynamics in phase-space, meaning trajectories converge to an *attractor* characterized by an asymptotic correlation dimension (Bec *et al.* (2007*b*)). As such, the development of correlation dimension is well described as a decaying exponential, allowing the asymptotic correlation dimension (which is denoted here as $\overline{\mathcal{D}}_2$) to be inferred from an exponential of best fit applied to a history of $\mathcal{D}_2(\tau)$. See Sec. C.6 for further details.

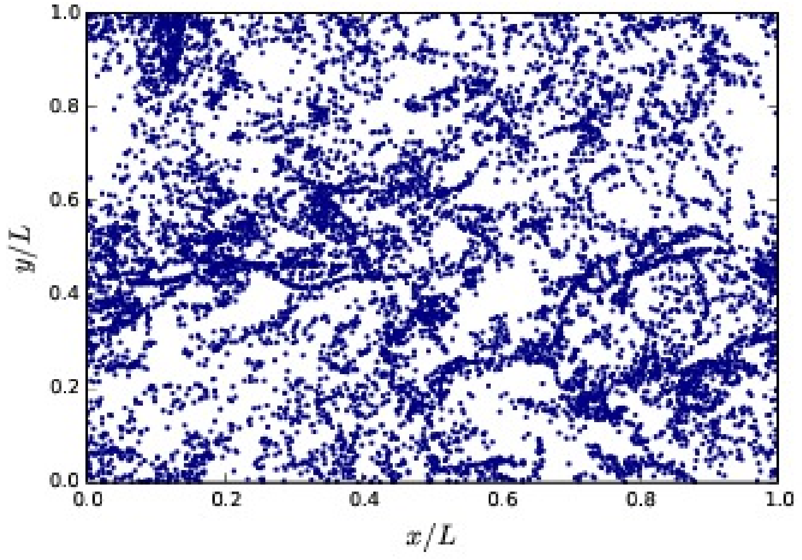

Figure 2.5: Preferential concentration of $St \sim 1$ inertial particles, from a $0.04L$-thick slice of particle-laden DNS. See details of simulation in 3.1.

2.3 Survey of known properties of KS

2.3.1 Unsteadiness

Since real turbulence is not steady, a wavenumber-dependent unsteadiness is modelled with the inclusion of the $\omega_n t$ term in (2.13). The precise feature of real turbulence enforced by the unsteadiness parameter is somewhat open to interpretation, but the traditional reasoning is as follows: eddies of size κ^{-1} have an associated velocity scale according to the Eulerian energy spectrum as $v_\kappa \sim \sqrt{\kappa E(\kappa)}$, so $(v_\kappa \kappa)^{-1}$ is generally regarded to be representative of the time it takes for an eddy of size κ to deform or “turn over”. Therefore ω_n can be set to capture this “eddy turnover time” corresponding to κ_n:

$$\text{(Type A KS): } \omega_n = \lambda \sqrt{\kappa_n^3 E(\kappa_n)} \tag{2.33}$$

where $\lambda \sim 1$. There exists an alternative, considerably less widespread formulation of unsteadiness (Turfus & Hunt (1987); Fung & Vassilicos (1998)), which, in a sense, enforces the rate of variation of small-scale velocities to be proportional to a characteristic "advection" velocity, and inversely proportional to their scale - this is meant to simulate the dynamic sweeping of small scales by the large. Osborne *et al.* (2005) demonstrated that under this formulation, the expected inertial and ballistic range scalings of the Eulerian one-point, two-time second-order velocity structure function (defined in Sec. B.3) are restored. This is hereafter referred to as Type B KS, and ω_n is alternatively given as:

$$\text{(Type B KS): } \omega_n = \lambda u_{rms} \kappa_n \tag{2.34}$$

where, once again, $\lambda \sim 1$. Both Types A and B KS are informed by heuristics transposed from classical turbulence phenomenology, and their applicability to KS is somewhat suspect. Ultimately the validity of such heuristics hinges upon the results they yield. There exists a modest body of literature on the subject of the effect of unsteadiness formulation on statistics of interest; the following is a summary:

- For Type A KS, there is no significant dependency of the pairwise Lagrangian statistics on λ for $0 < \lambda < 1$. (Malik & Vassilicos (1999))
- According to a simple dimensional analysis (and corroborated by numerical evidence), $S^L(\tau) \sim \tau$ and $\Phi^L(\omega) \sim \omega^{-2}$ scalings are expected. In Type A KS, this behaviour is recovered only for large λ, in particular, $\lambda \sim 5$. (Khan & Vassilicos (2003); Osborne *et al.* (2005))
- The clustering of inertial particles is contingent upon the presence of *persistent*

coherent structures in the turbulence. If the temporal variation of the field is improperly enforced (i.e. high λ) the effect on the particle ensemble is that, unsurprisingly, clustering (in the 2D case) is not reproduced. (Chen *et al.* (2006))

- With the adoption of Type B KS, an improvement in the $\Phi^L(\omega)$ scaling is noted, but $R^L(\tau)$ remains highly unrealistic (Osborne *et al.* (2005)).

These results unfortunately do not endue KS models with the banner of broad applicability, because particle behaviour is contingent on more than the scaling, but also on the degree of proportionality (as was pointed out for pairwise dispersion by Flohr & Vassilicos (2000)).

2.3.2 Preferential concentration

Preferential concentration in KS has most often been treated within the context of pairwise dispersion, which may offer a limited scope for the reasons discussed in Sec. 2.2.6. There exists only one assessment of correlation dimension for inertial particles in 3D KS (Ijzermans *et al.* (2010)), in which good qualitative agreement was obtained with the well-established relation of $\overline{\mathcal{D}}_2$ vs St in DNS (for example, see Bec *et al.* (2007*a*)). There exists a modest body of literature on the multi-scale properties of clusters of inertial particles in 2D KS (Goto & Vassilicos (2006), Goto & Vassilicos (2008), Chen *et al.* (2006)), though there is little reason to expect such conclusions to be transferable to the 3D case.

2.3.3 Lagrangian integral timescale

At the heart of Lagrangian statistics lies the integral timescale, T_L - indeed the favourable comparisons of even many *pairwise* statistics between DNS and KS are predicated upon non-dimensionalization of time by T_L (Malik & Vassilicos (1999)). In the pursuit of a broadly applicable KS modelling tool, perhaps the most important question one can ask regarding KS is, can it reproduce T_L? And even if it can (for fluid tracers), does this extend to cases where T_L is considerably more elusive, to wit, inertial particles exhibiting the continuity effect? The answer is, of course, it depends on whether one is using the "correct" input. Unfortunately the only guidance in the literature regarding these questions is summarized as follows:

- In a seminal study on KS (Fung *et al.* (1992)), it is observed that $T_L u_{rms}/L_{11} \approx 0.5$ (where L_{11} is the integral length scale, defined in App. A), for their particular version of KS (which is not widely applied). The authors note that their results for non-dimensionalized T_L starkly contrast those in experimental observations.

- In Osborne *et al.* (2005), favourable comparison of T_L to experiments is obtained, for the case of fluid tracers in very high Reynolds number flow, though with a modified input energy spectrum.

To summarize, these investigations (along with those mentioned in 2.3.1 and 2.3.2) do provide some hints on how to judiciously apply KS - though it appears statistics of interest have, broadly speaking, been investigated in isolation. Consequently, there is a need to develop a systematic manner of applying KS such that both single-particle Lagrangian statistics and correlation dimension are realistically reproduced - and a natural first step in this endeavour is to observe the performance of KS for input Eulerian statistics that are, in some sense, realistic. Such statistics could be furnished by a DNS, which could also be used as a benchmark for comparison.

2.4 Summary

SSF models are widely-applied particle-laden flow models that, in a variety of senses, have difficulty synthesizing the impact of turbulence structure on the particle ensemble. KS is a method for enforcing the second-order Eulerian statistics, which hints at the potential for prediction of realistic particle behaviour. Despite various indications in the literature that, when applied in a particular fashion, KS can realistically restore isolated properties of particle statistics, a broadly applicable model is sought, which can achieve reasonable reproduction of single-particle Lagrangian statistics and correlation dimension.

KS will be evaluated against a DNS benchmark, for fluid tracers, and inertial particles with a variety of St. Simulations will be run with and without gravity. The effect of different types of unsteadiness (Types A and B), with varying unsteadiness parameters, λ, will be investigated. Even if such a “realistic”-input strategy yields an unfavourable comparison, such an investigation will nonetheless provide clues on an appropriate strategy for the development of KS as a modelling tool.

Chapter 3

Assessment of KS: Methodology

3.1 DNS solver

A parallelized DNS solver was used to solve the incompressible Navier-Stokes equations, within a periodic box geometry. The solver was pseudospectral, meaning all terms were solved in spectral space, with the exception of the nonlinear convective term, which was solved in physical space. A simple de-aliasing scheme was applied, in which all modes above 2/3 the maximum wavenumber were zeroed after the computation of the nonlinear term, in order to eliminate the spurious amplification of energy at small scales. The energy was kept nearly constant with a simple forcing scheme (Chen *et al.* (1993)): the energy at low-wavenumber components of the field (namely at Fourier modes such that $1 < |\kappa/\kappa_{min}| < 3$) was maintained constant, and such that the $-5/3$ scaling of $E(\kappa)$ vs. κ was enforced over these wavenumber shells. An approximate initial velocity field was generated (in a KS manner) according to an approximate spectrum, and the DNS was allowed to evolve until the $-5/3$ scaling

Parameter/statistic	Value
Number of grid points, N^3	256^3
Domain length in DNS, L	1
Maximum resolved wavenumber, κ_{min}	2π
Maximum resolved wavenumber, κ_{max}	128π
Cutoff wavenumber (for de-aliasing)	$\frac{2}{3}k_{max}$
Time step length, Δt	0.001
Simulation length, t_{end}	8
Mean Taylor scale Reynolds number, Re	~ 90
Skewness of $\frac{\partial u_i}{\partial x_j}$, γ_u	~ 0.5

Table 3.1: Relevant parameters and output statistics for the incompressible DNS

propagated through much of the inertial range, and until the skewness of the velocity derivatives reached approximately 0.5 (as was done in Elghobashi & Trusedell (1992)), indicating fully developed turbulence. The relevant parameters and averaged statistics of the DNS are given in Table 3.1. Further details on the DNS are given in App. A.

3.2 KS solver

The energy spectrum is defined as the derivative with respect to wavenumber:

$$E(\kappa) = \frac{d}{d\kappa}\mathscr{E}(\kappa) \tag{3.1}$$

where $\mathscr{E}(\kappa)$ is the measure of energy over all scales at or below κ. In practice for a discretized DNS, this is simply the sum of the norms of Fourier coefficients of velocities, at all wavenumbers whose norm does not exceed κ:

$$\mathscr{E}(\kappa) = \frac{1}{2}\sum_{|\boldsymbol{K}|\leq\kappa} \langle \hat{\mathbf{u}}(\boldsymbol{K}) \cdot \hat{\mathbf{u}}^*(\boldsymbol{K})\rangle \tag{3.2}$$

where $(^*)$ denotes complex conjugate. For the DNS method in question, the cumulative spectrum is evaluated for an arithmetic sequence of wavenumbers (denoted as γ_m, where $\gamma_m = \kappa_{\min} m = 2\pi m$, and κ_{min} is the minimum resolved wavenumber). Therefore $\mathscr{E}(\kappa)$ is a step function, and correspondingly $E(\kappa)$ is the sum of Dirac-delta distributions.

Therefore it is prudent to simply set the wavenumber sequence to that which is determined by the input DNS, therefore let $\kappa_n = \gamma_n$ for all n (that is, let $\kappa_n = 2\pi n$). A more appropriate rendering of (2.15) is thus:

$$|\mathbf{a}_n|^2 = |\mathbf{b}_n|^2 = \begin{cases} 2(\mathscr{E}(\kappa_n) - \mathscr{E}(\kappa_{n-1})) & \text{if } n > 1 \\ 2\mathscr{E}(\kappa_n) & \text{if } n = 1 \end{cases} \tag{3.3}$$

A variety of choices for unsteadiness parameter were employed for both unsteadiness formulations (Types A and B KS), in line with those tested in the literature: $\lambda = 0, 0.5, 1$ and 5. (For instance, Malik (1991) tested pairwise dispersion for Type A KS, with $0 \leq \lambda \leq 10$). $\lambda = 0$ corresponds to a steady flow, in which case there is no difference between Types A and B KS.

As mentioned, there exists much literature on pairwise dispersion results in KS, which serves as a basis for verifying the KS solver - these results are presented in App. D.

3.3 Lagrangian particle tracking solver

The DNS and KS were interfaced with a fourth-order, explicit Adams-Bashforth solver of the Lagrangian momentum equation (2.9). For both DNS and KS, a fixed time step was employed, an appropriate choice of which should be significantly smaller than the smallest relevant time scale of the flow; namely, the Kolmogorov timescale (τ_η). The general rule of thumb is to enforce $\Delta t < 0.01\tau_\eta$ (Osborne *et al.* (2006); Thomson & Devenish (2005); Malik (2014)). In real turbulence, the Kolmogorov timescale is controlled by, among other things, the viscosity, whereas all properties of the cascade are explicitly defined for KS - consequently "Kolmogorov timescale" does not have a clear meaning for a kinematically defined cascade. Consequently, to corroborate this estimate, a sensitivity analysis was carried out - it was determined that for particle tracking, $\Delta t = 0.001$ granted confidence in all statistics of interest (See App. C).

Simulations were carried out for a variety of inertial particle Stokes numbers (namely 0.25, 0.5, 0.75, 1, 1.5, 2, 5 and 10). Of particular interest is the behaviour of the inertial particle ensemble for $St \sim 1$, since the maximal clustering of such particles is well documented both experimentally and numerically (Squires & Eaton (1990); Wang & Maxey (1993); Fessler *et al.* (1994); Bec *et al.* (2007*a*)). Note that for particles in the DNS, Stokes numbers are approximate, since they are dependent on the Kolmogorov timescale (by (2.10)), and in DNS (as in real turbulence), this quantity does not remain perfectly constant (as was pointed in Monchaux *et al.* (2012)).

For the particle-laden DNS, the assumption of one-way coupling allows an entire DNS to be carried out separately. Here, the DNS field (corresponding to the appropriate timestep) was then read into the particle-tracking method, and the fluid velocities at the (continuously-defined) particle locations were recovered via 3rd-order Hermite polynomial interpolation. Alternatively for KS, the fluid velocities at the appropriate locations and times are simply recovered by (2.13). Since a KS field is a superposition of real-valued trigonometric functions, it is *gridless*, and numerical errors arising from interpolation are avoided.

The inertial particle simulations were run with and without gravity. When gravity was present, the acceleration was varied according to St, to ensure the drift velocity exceeded the root mean squared turbulent velocity (a necessary condition for the observation of the continuity effect (Wells & Stock (1983))), but not so large that the solver was rendered unstable. For further details, see Sec. C.4

Ensuring confidence of statistics

If only Lagrangian statistics are sought, it is enough to allow the sample space of particle positions to be arbitrarily large, to ensure the velocities sampled at the particle locations are truly representative of what is determined by the KS parameters. This is termed Type I KS. When considering the *structure* of the ensemble of particles, it becomes important to constrain the particles to a sufficiently small domain, such that enough particles interact with the same turbulence structures. To satisfy this requirement, a high mean concentration of particles is needed to minimize the sample error of $P_2(r)$ for small values of r (since the correlation dimension is evaluated from $P_2(r)$ near 0). Since the evaluation of $\mathcal{D}_2$ scales as the square of the number of particles (because every particle must be compared to every other particle), this places a severe constraint on the size of domain in terms of computational cost.

Constraining the simulation to a finite domain has the following drawback: if the orientation of $\boldsymbol{\kappa}_n$ is distributed uniformly over a sphere, periodicity is not guaranteed for a given KS realization, therefore particles cannot be allowed to leave one edge of the domain and enter the other, as is done in the (periodic) DNS, since the fluid velocity history seen by a given particle could be rendered highly discontinuous. Previous authors (Flohr & Vassilicos (2000); Ijzermans *et al.* (2010)) applied a mildly modified formulation, in which the sample space of orientations, and indeed choice of κ_n, are constrained such that periodicity is enforced. This strategy is avoided here, in order to avoid potentially spurious effects of the alignment of the large-scale motions.

An alternative solution to the aperiodicity problem is to impose an absorbing boundary condition (that is, particles which exit the boundary are simply dropped from the simulation). This in turn means a simulation constantly "bleeds" particles, potentially skewing the particle statistics. A solution is to employ an extended domain; an 'outer' domain throughout which the particles are initially uniformly distributed and advected (and whose boundary is given the absorbing boundary condition), and an 'inner' subdomain over which the statistics of the particle ensemble are evaluated - this scenario is roughly depicted in Fig. 3.1. Care must be taken so that the inner domain contains roughly the same number of particles ($N_p(t)$) over the length of the simulation (see Sec. D.2). This strategy of constraining the evaluation of particle statistics to a limited domain is termed Type II KS. Also the domain over which statistics are evaluated is termed the *sample domain* - for the DNS and Type I KS, the sample domain is the whole domain, and for Type II KS, it is the inner domain. In the case of KS with gravity (in which particles are drifting downward), the sample domain was placed near the bottom of the outer domain, once again to maintain a roughly constant mean concentration in the sample domain. For all Type II KS here, the length of the outer domain was twice that of the inner domain.

The restriction of the KS to a small bounded domain poses an additional problem: if the length of the domain is comparable to the largest scales of the KS, the

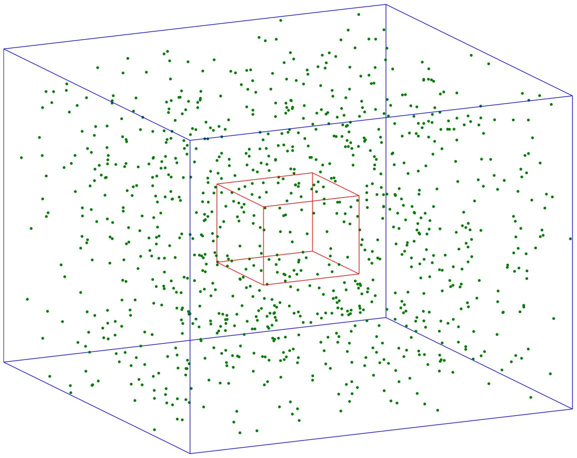

Figure 3.1: Illustration of particle-laden Type II KS. The computational domain consists of an outer domain with an absorbing boundary condition, and a smaller inner subdomain in which the statistics of the particles are calculated. The ensemble of particles is depicted as dots. In contrast, Type I KS occurs on an arbitrarily large spatial domain.

fluid energy averaged over the inner subdomain can be quite different from the imposed energy. Hence *multiple* realizations were carried out for a set of KS input parameters, and the averaged results were considered (in other words, *serial farming* was employed). The case for multiple realizations is strengthened by additional considerations: the ensemble of realizations is on average isotropic (whereas a single realization can be highly anisotropic), and the sensitivity of particle clustering on the mutual orientation of the largest scales is reduced (See Sec. B.4 for a semi-analytical derivation of large-scale anisotropy tensor).

Multiple realizations of particle tracking were carried out in parallel also for the particle-laden DNS, to lower the simulation runtime. For either DNS or KS, the total number of particles vastly exceeds the amount required for statistical significance of Lagrangian statistics (Strutt *et al.* (2011); Cernick *et al.* (2015)). The key particle tracking parameters are summarized in Table 3.3.

Statistic	KS Type
Single-particle Lagrangian, without gravity	I
Single-particle Lagrangian, with gravity	II
Correlation dimension, without gravity	II
Correlation dimension, with gravity	II

Table 3.2: KS Type for various statistics of interest.

It should be noted that in Type II KS (bounded domain), the tendency of the domain to bleed particles to the absorbing boundary condition implies a limited period during which the mean concentration of particles in the inner domain remains roughly constant. For Type I KS (unbounded domain), there exists no such concern, and for single-particle Lagrangian statistics, long simulations are preferred to ensure all particles have “forgotten” their ballistic range behaviour. All single-particle Lagrangian statistics (in the no-gravity case) were simulated in Type I KS. In the gravity case, particles which rapidly traverse a periodic domain in the DNS will see a spuriously highly correlated fluid field (Cernick (2013)), thus there exists no benefit in running a very long simulation for the corresponding KS case. Consequently for Lagrangian statistics in KS with gravity, Type II KS was employed. All correlation dimension values were calculated in Type II KS, again due to the need for a high mean concentration to obtain meaningful measurements of clustering. This is summarized in Table 3.2.

Time units have been non-dimensionalized against the Kolmogorov timescale, τ_η (defined as $\tau_\eta = (\nu/\epsilon)^{1/2}$, where ϵ is formally related to the spectrum as $2\nu \int_0^\infty \kappa^2 E(\kappa)\, d\kappa$) and dispersion has been non-dimensionalized by the square of the domain length, L.

Parameter	DNS Value	KS Value
Number of particles in sample domain, per realization	200 000	$\sim$ 50000
Number of realizations	15	300
Timestep	0.001	0.001
Number of timesteps	8000	8000

Table 3.3: Relevant parameters for particle tracking methods.

Chapter 4

Assessment of KS: Results

4.1 Eulerian statistics

Since KS is designed to enforce the Eulerian energy spectrum, a natural starting point for a general assessment of KS is to test whether a variety of Eulerian statistics are reproduced, and to compare to other results in the literature. Fortunately, many such statistics can be evaluated analytically; see App. B for derivations of the turbulent kinetic energy (as a verification of the choice of mode amplitudes in equation (2.15)), two-point, one-time (and one-time, two-point) velocity autocorrelations, and large-scale anisotropy.

4.2 Tracers

4.2.1 Pairwise dispersion

There exist many results in the literature on pairwise dispersion of passively-advected tracers in KS, which naturally provide a basis for verification of the KS solver. In particular, in Malik & Vassilicos (1999), the authors observed the pairwise dispersion in steady ($\lambda = 0$) Type A KS, whose input spectrum roughly matches the energy spectrum from the DNS results of Yeung (1994), and for a variety of initial separations of pairs of particles. This result is reproduced in App. D.

4.2.2 Single-particle Lagrangian statistics

For brevity, fluid particles are referred to as *tracers* in the results. For incompressible flow, the Eulerian-averaged and Lagrangian-averaged energies coincide (Tennekes & Lumley (1972)), thus a simple starting point for the assessment of Lagrangian statistics in KS is to ensure that the energy (conditioned on fluid tracers) is equal to that which is determined by the input spectrum. In Fig. 4.1, the history of $\langle |\mathbf{u}_p|^2 \rangle$ in KS is given, for a variety of unsteadiness parameters (normalized by the constant $2 \sum E(\kappa_n)\, \Delta\kappa_n$), and excellent agreement with the expected value of unity is observed. This indicates that the output energy conditioned on tracer locations recovers the input energy.

In Fig. 4.2, the dispersion histories of tracers is shown, for a variety of λ, for Types A and B KS. Beyond the ballistic range of times, the linear scaling of both DNS and steady ($\lambda = 0$) KS is evident, in accordance with the predictions of Taylor (1921). In all cases, the dispersion is underpredicted, and indeed the larger λ is,

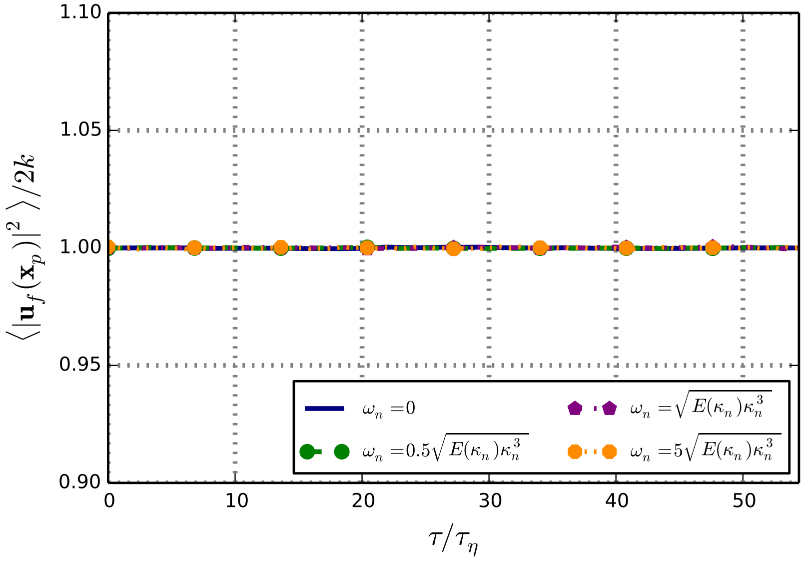

Figure 4.1: The mean squared velocity of tracers, $\langle|\mathbf{u}_f(\mathbf{x}_p)|^2\rangle$, in type A KS, for a variety of unsteadiness parameters, non-dimensionalized by twice the input energy (evaluated as $k = \sum E(\kappa_n)\,\Delta\kappa_n$).

the more severe the extent of underprediction. Consistent with the observations of Malik (1991), dispersion is noticeably reduced for even a weakly unsteady field ($\lambda = 0.5$ for either Type A or Type B); this stands in contrast to pairwise Lagrangian statistics, which are largely insensitive to λ, for roughly $\lambda < 1$ (Malik (1991); Malik & Vassilicos (1999)). The difference in asymptotic dispersion rate (diffusivity) is a consequence of the differing integrals of $R^L(\tau)$ as follows from (2.23) (and that the energy evaluated by the Lagrangian average is independent from the unsteadiness). An interpretation of this is that in a strongly unsteady field, a tracer travels only a very short distance before encountering a new "eddy", resulting in a decrease of the Lagrangian autocorrelation (see Fig. 4.3 for Type A KS. Type B KS results are similar).

In Fig. 4.4, the τ-separation of one diagonal component of the flatness tensor of the

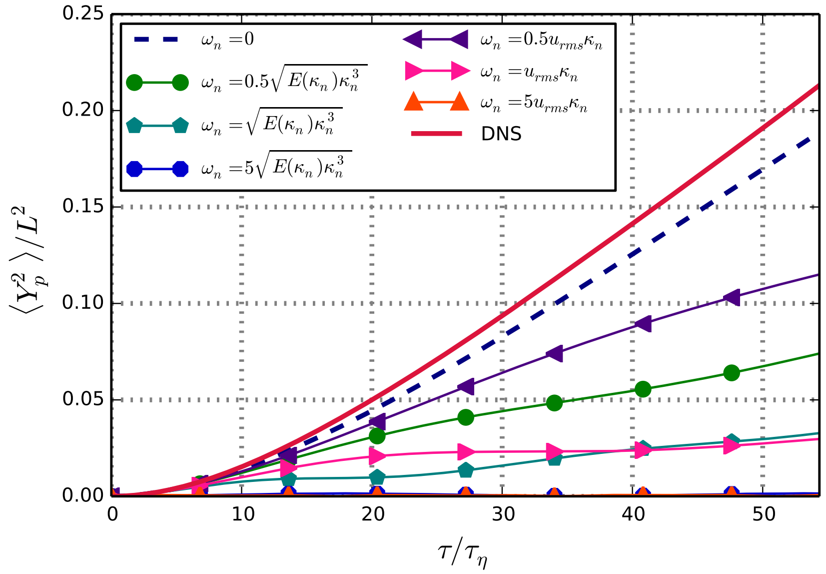

Figure 4.2: Dispersion of fluid tracers in Types A and B KS, with a range of unsteadiness parameters $\lambda = 0, 0.5, 1, 5$. DNS results are shown for comparison.

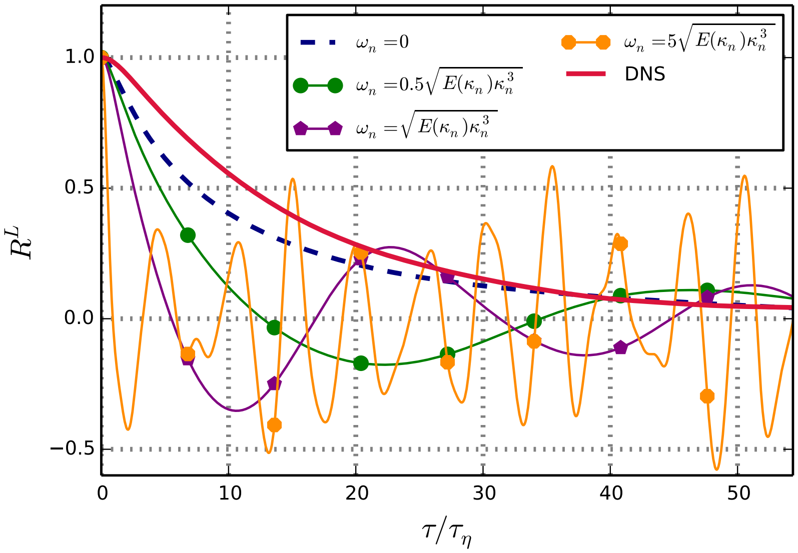

Figure 4.3: Lagrangian autocorrelation of fluid tracers in Type A KS, with $\lambda = 0, 0.5, 1, 5$, with comparison to DNS results. Type B results are similar.

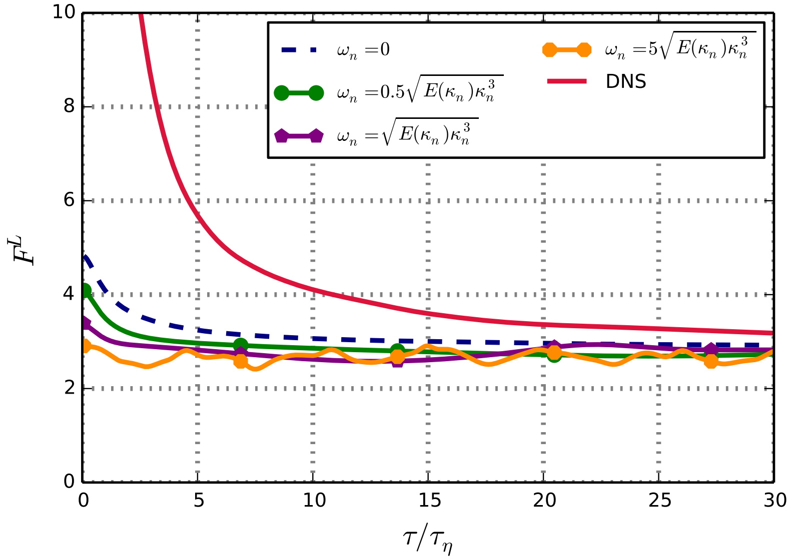

Figure 4.4: $F_{11}^L(\tau)$ (component of the flatness of the Lagrangian velocity) for fluid tracers for DNS, and for Type A KS, with $\lambda = 0, 0.5, 1, 5$. For the DNS case, $F_{11}^L(0) \sim 24$.

Lagrangian velocity is shown for DNS and Type A KS. KS underpredicts the flatness of velocity histories in all cases, though $\lambda = 0$ yields the most intermittent velocity histories. More insight is offered by visualizations of typical particle trajectories in DNS and KS; the curves in the DNS case are considerably smoother, and are characterized by long stretches of relatively steady velocity, interspersed with fewer rapid changes than the KS (Fig. 4.5).

It has been reported (Fung *et al.* (1992), Khan & Vassilicos (2003), Osborne *et al.* (2005)) that in low-λ (weakly unsteady) KS, the Lagrangian structure function scales as $S^L(\tau) \sim \tau^{2/3}$ in the intermediate range of times, in contrast to the Kolmogorov scaling $S^L(\tau) \sim \tau$ for real turbulence. $S^L(\tau)$ is reported in Fig. 4.6 for DNS and steady ($\lambda = 0$) KS, and the case for neither $S^L(\tau) \sim \tau^{2/3}$ in KS, nor $S^L(\tau) \sim \tau$ in DNS is particularly convincing. This is likely a result of a relatively small separation

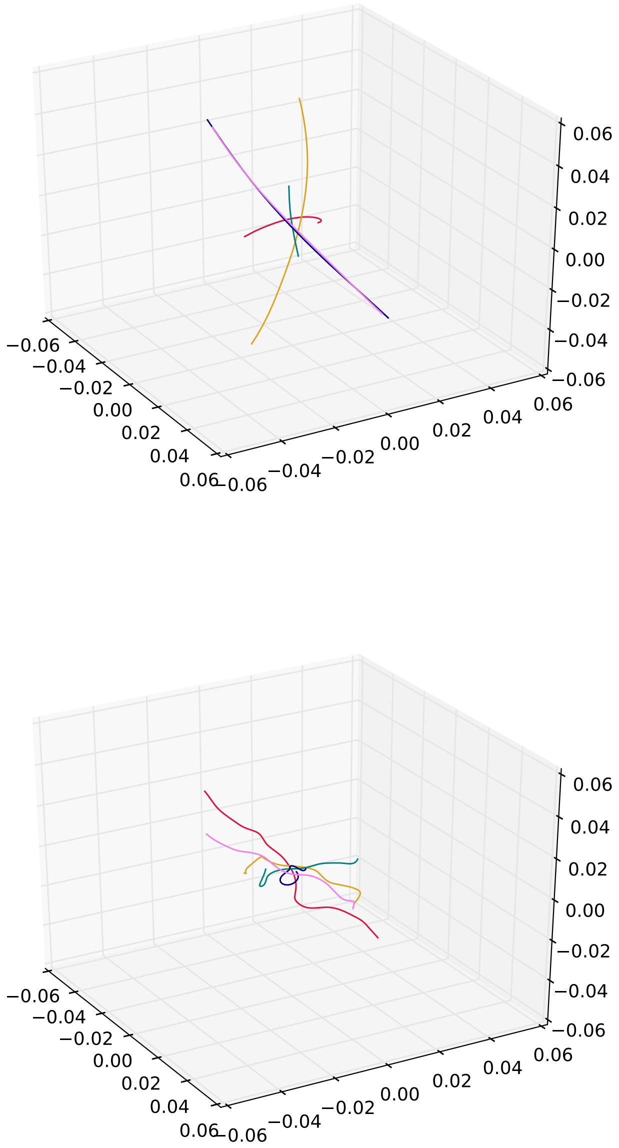

Figure 4.5: Sample of particle paths in DNS (above) and the steady ($\lambda = 0$) KS (below). The width of each dimension of the box in the visualization is approximately four times the Kolmogorov microscale.

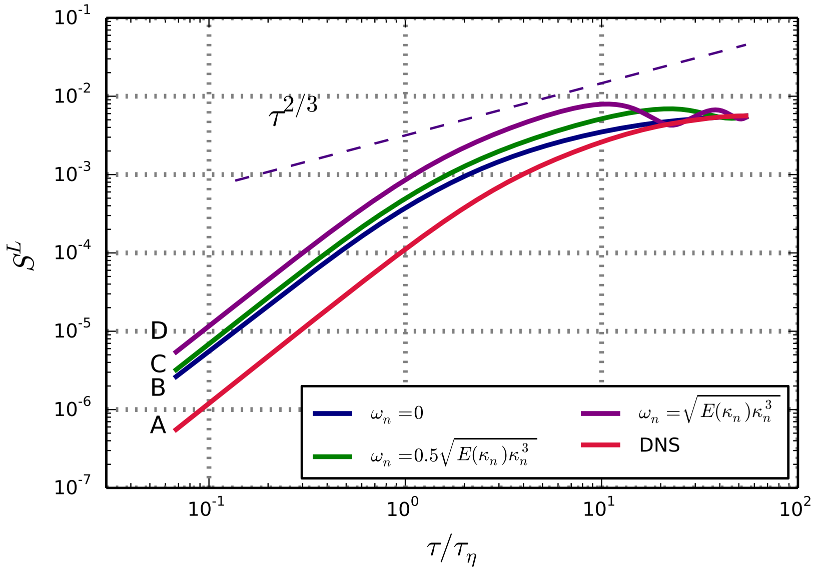

Figure 4.6: The Lagrangian structure function, $S^L(\tau)$, for fluid tracers for DNS (line A) and for KS, with $\lambda = 0$ (B), $\lambda = 0.5$ (C) and $\lambda = 1$ (D).

of scales that characterizes low Reynolds number flows. This suspicion is confirmed by the restoration of this scale relation for a wider inertial range (see Sec. 5.1.2).

In Fig. 4.7 the Lagrangian frequency spectrum is shown for steady ($\lambda = 0$) KS. In accordance with the observations of Khan & Vassilicos (2003), the scaling $\Phi^L(\omega) \sim \omega^{-5/3}$ is roughly reproduced. In Fig. 4.8, the same result is shown for unsteady ($\lambda = 1$) KS, alongside the corresponding spectrum in DNS. In accordance with Osborne *et al.* (2005), the elevation of λ somewhat restores the scaling to $\Phi^L(\omega) \sim \omega^{-2}$, and there appears to be some evidence that this scale relation is also observed in the DNS. Indeed $\Phi^L(\omega) \sim \epsilon\omega^{-2}$ is expected according to the Kolmogorov scaling form (given by dimensional analysis) (Tennekes & Lumley (1972)), and is also observed in real turbulence (Lien *et al.* (1998); Mordant *et al.* (2001)). Due to the relative brevity of the simulations here, the numerical evaluation of the inner product in (2.28) (on a limited time domain) introduces error. Osborne *et al.* (2005) encountered the

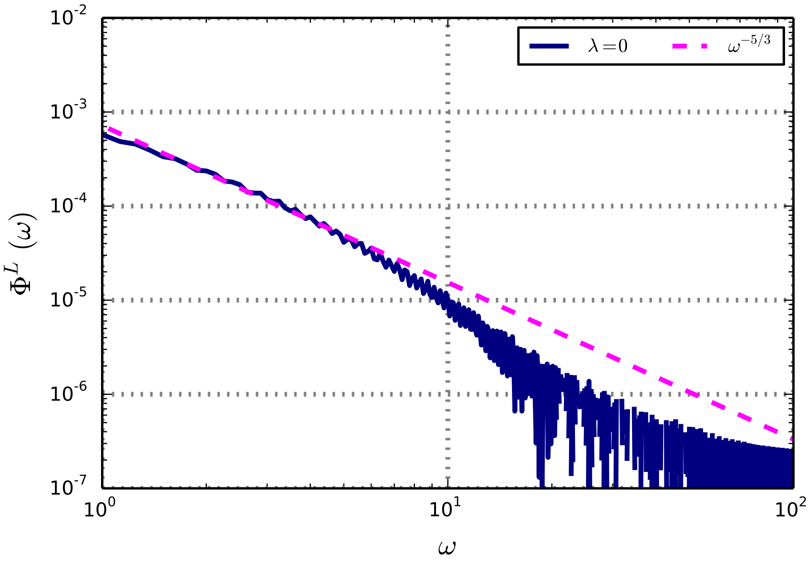

Figure 4.7: Lagrangian frequency spectrum, $\Phi^L(\omega)$, for steady KS ($\lambda = 0$)

same problem, and addressed it by filtering the result with a "simple sliding 10 Hz nonoverlapping averaging window", however this strategy is avoided here, since the convolution of a filter and even an analytically defined power function, say ω^r, will not preserve r. In any event, the same concern in the previous paragraph applies here; that due to the narrow inertial range in question, it may not be reasonable to expect either the KS or DNS scalings of the frequency spectra to agree exactly with observations in the literature.

Once again, KS is constructed such that the Eulerian energy spectrum in wavenumber space is exactly reproduced. The inclusion of the $\omega_n t$ term in (2.13) is informed by heuristic arguments about how long it takes eddies of given scales to "turn over" (Type A KS), or by a quasi-enforcement of the Eulerian frequency spectrum (Type B KS). However elsewhere (Fung *et al.* (1992)) the inclusion of $\omega_n t$ is motivated by the need to account for the change of velocity experienced by a material volume.

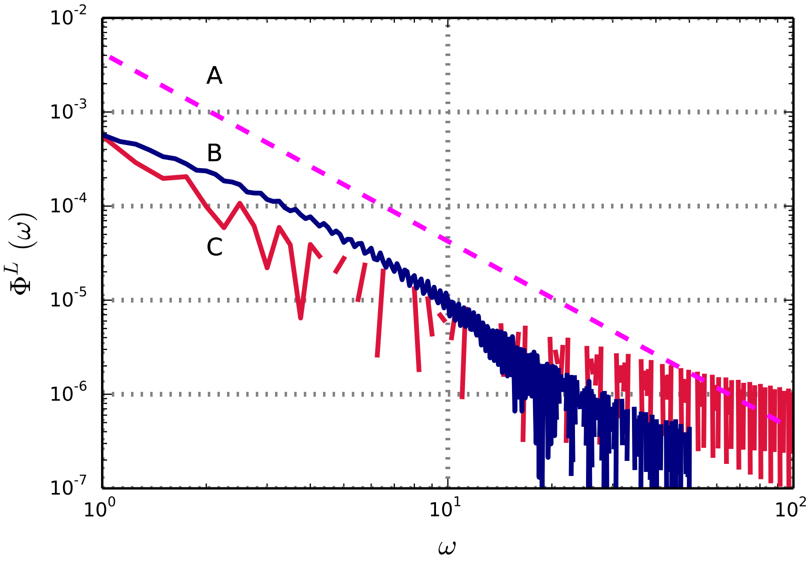

Figure 4.8: Lagrangian frequency spectrum, $\Phi^L(\omega)$, for KS, with $\lambda = 1$. Line A is the theoretical scale relation $\Phi^L(\omega) \sim \omega^{-2}$, Line B is from unsteady KS ($\lambda = 1$), and Line C is from the DNS.

This is most meaningfully interpreted as enforcing the proper integral scale of the Lagrangian velocity autocorrelation, however this analysis suggests that, under the traditional unsteadiness formulations, this does not occur for even moderate λ. Even though $\lambda = 0$ yields a field with unphysical steadiness in the Eulerian frame of reference, even very simple kinematic fields have been observed to yield qualitatively realistic, chaotic Lagrangian motion (Arnold (1965)) - indeed this was observed for the application of KS as a subgrid complement by Khan *et al.* (2010).

4.2.3 Correlation dimension

The theoretical value of 3 was approximately recovered for $\mathcal{D}_2$ at all times for tracers in DNS (in accordance with previous observations (Bec *et al.* (2007*a*); Strutt *et al.* (2011); Cernick (2013))), which provides further confidence in the numerical tools.

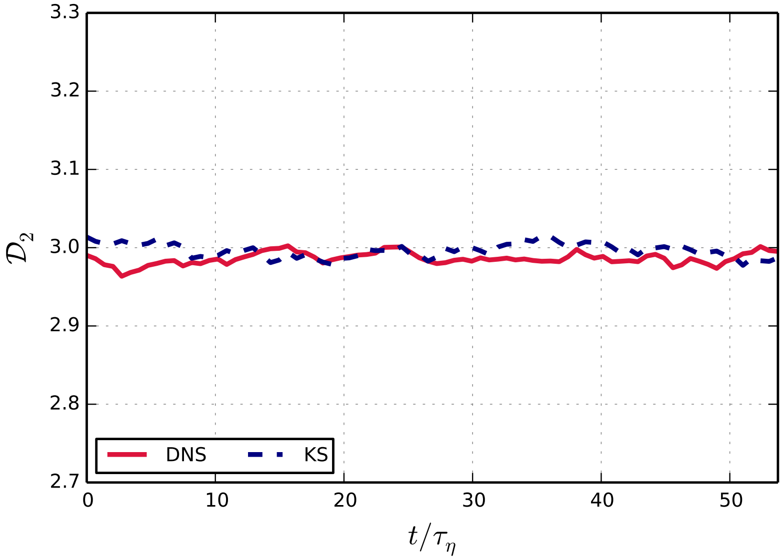

Figure 4.9: History of $\mathcal{D}_2$ for tracers, for DNS and steady ($\lambda = 0$) KS.

Steady ($\lambda = 0$) KS also very closely recovers 3 for tracers (see Fig. 4.9).

4.3 Inertial particles, without gravity

4.3.1 Single-particle Lagrangian statistics

The Lagrangian statistics for inertial particles exhibit largely the same dependence on unsteadiness; the best match between DNS and KS occurs when there is no imposed unsteadiness ($\lambda = 0$), in which case the dispersion is slightly underpredicted by KS.

The expected character of particle dispersion with gravity is verified for DNS. Consistent with the results of Squires & Eaton (1991), the long-range dispersion of all inertial particles *exceeds* that of tracers, and the dispersion is maximal for intermediate St (See Fig. 4.10). For steady ($\lambda = 0$) KS, the increased dispersion of

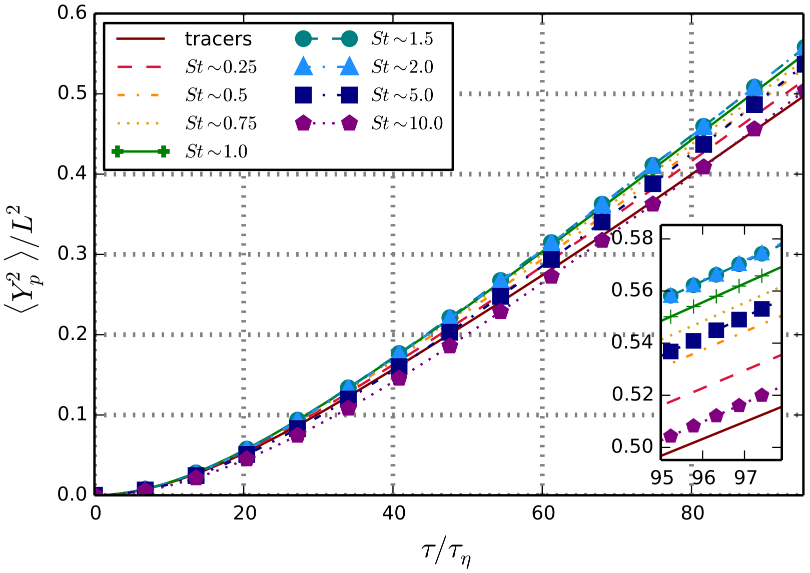

Figure 4.10: Dispersion in DNS, for tracers and all inertial particle types, without gravity. Inset plot is zoomed-in view of long-range dispersion.

inertial particles over tracers is also seen (Fig. 4.11), though the increase in long-range dispersion vs. St appears to be nearly monotonic. The long-range dispersion is compared between DNS and steady ($\lambda = 0$) KS in Fig. 4.12 and the best match occurs for high St inertial particles.

The dispersion of $St \sim 1$ particles in DNS and Types A and B KS is shown in 4.13, and the corresponding results for Lagrangian autocorrelation are shown in Fig. 4.14 (though for just DNS and Type A KS). As was observed for tracers, the most favourable match between KS and DNS occurs for the steady case, $\lambda = 0$.

4.3.2 Correlation dimension

As is the case with dispersion, the prediction of $\mathcal{D}_2(t)$ is exacerbated by unsteadiness, under either unsteadiness formulation, and indeed the extent of overprediction is

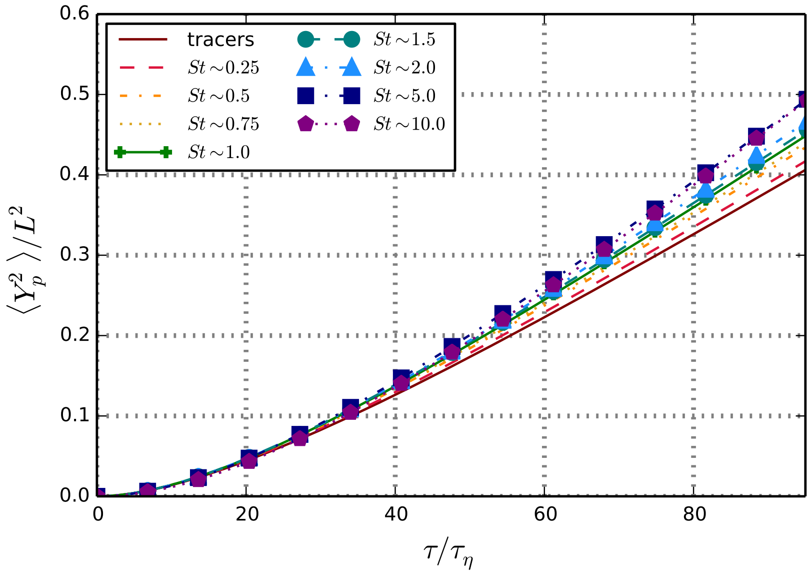

Figure 4.11: Dispersion in steady ($\lambda = 0$) KS, for tracers and all inertial particle types, without gravity.

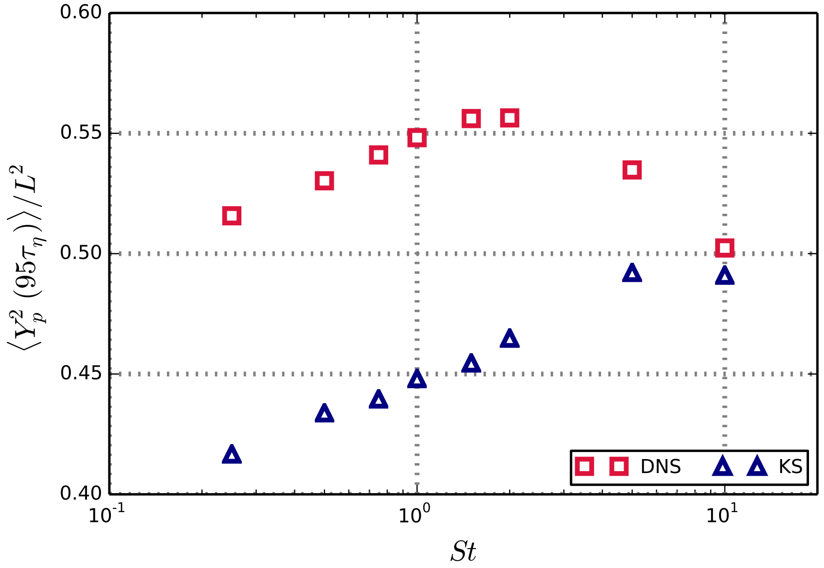

Figure 4.12: Long-range dispersion (evaluated at 95 τ_η), for DNS and steady ($\lambda = 0$) KS, for all inertial particles, without gravity.

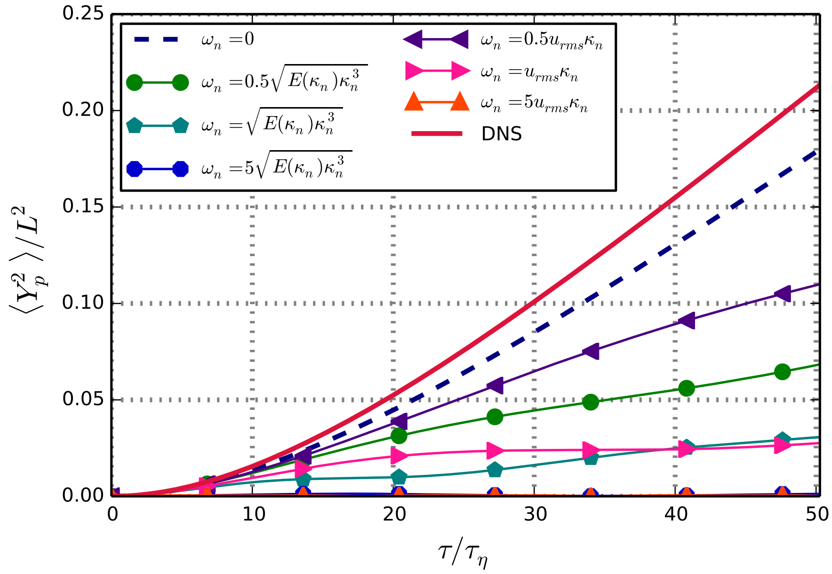

Figure 4.13: Dispersion of $St \sim 1$ particles in Types A and B KS, with a range of unsteadiness parameters $\lambda = 0, 0.5, 1, 5$. DNS results are shown for comparison.

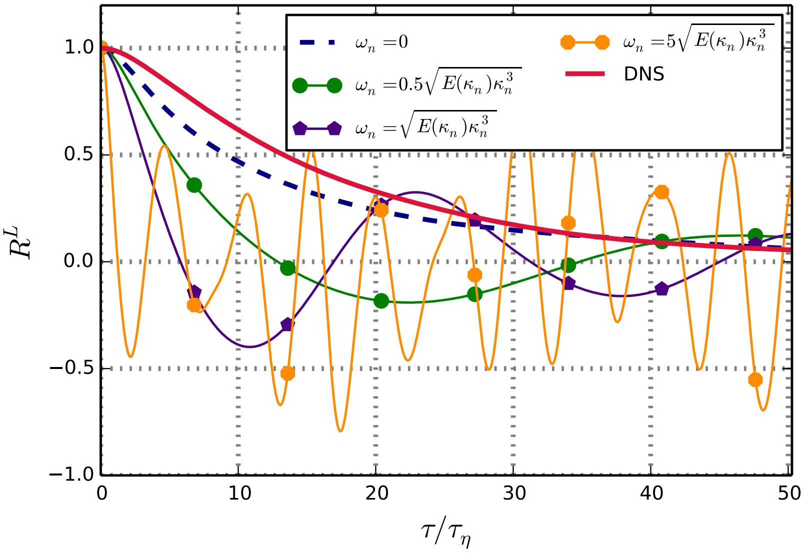

Figure 4.14: Lagrangian autocorrelation of $St \sim 1$ particles in Type A KS, with $\lambda = 0, 0.5, 1, 5$, with comparison to DNS results. Type B results are similar.

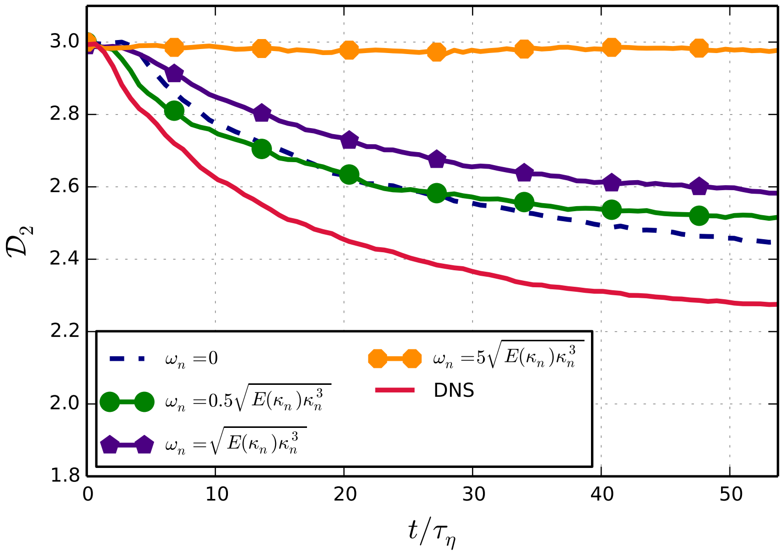

Figure 4.15: History of correlation dimension for Type A KS, with $\lambda = 0, 0.5, 1, 5$; for $St \sim 1$ inertial particles, with DNS shown for comparison.

proportional to λ. Once again, the best results are obtained for steady ($\lambda = 0$) KS (See Fig. 4.15 for Type A KS).

Indeed, as noted in Osborne *et al.* (2005), high unsteadiness causes a lack of persistence of the flow field, upon which depends the organization of the ensemble of particles. The asymptotic correlation dimension (denoted $\overline{\mathcal{D}}_2$) as a function of St, for DNS and KS, is shown in Fig. 4.16. The profiles show good qualitative agreement with observations in the literature, for both DNS (Bec *et al.* (2007*a*); Cernick (2013)) and KS (Ijzermans *et al.* (2010)), with the minimum $\overline{\mathcal{D}}_2$ occurring for moderate Stokes numbers ($St \sim 1$), within either DNS or KS - again low $\overline{\mathcal{D}}_2$ indicates greater clustering. A lack of quantitative agreement with previous DNS results may be explained by the inherent difficulty in estimating the Stokes number (as pointed out by Monchaux *et al.* (2012)), and qualitative differences in the spectra (perhaps arising from the choice of forcing method). The lack of quantitative agreement with pervious KS results may be

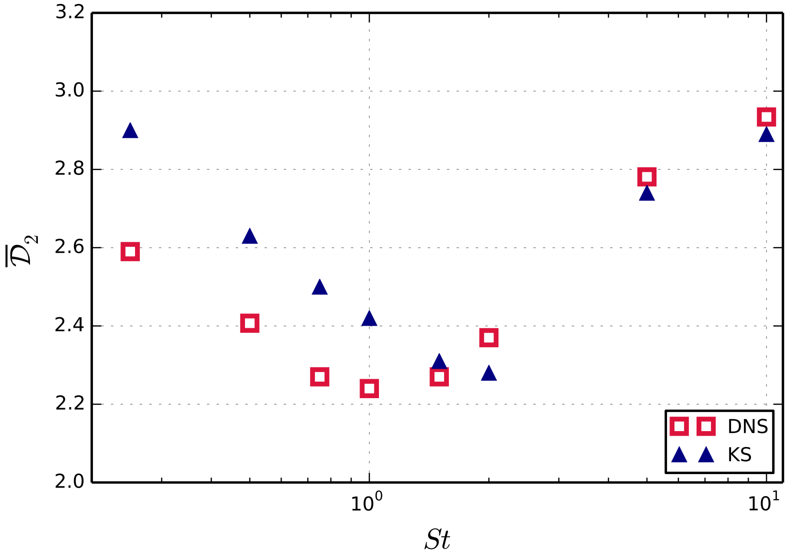

Figure 4.16: Correlation dimension ($\overline{\mathcal{D}}_2$) as a function of St, without gravity, for DNS and steady ($\lambda = 0$) KS.

explained by fundamental differences in the implementation of KS; Ijzermans *et al.* (2010) employed an unsteady field (corresponding to neither Type A nor Type B KS as described here), and enforced periodicity of the KS modes. All results hereafter are for steady ($\lambda = 0$) KS.

For either dispersion or preferential concentration, it appears the most favourable comparison between KS and DNS occurs for high-St particles. Insight into the reason is offered by the observation of Coleman & Vassilicos (2009), that KS fields produce a spurious *spectral broadening* of the energy spectrum in the frequency domain. Particle inertia has the effect of filtering out the high frequency turbulent motions (Csanady (1963)) and since the dynamics of high-St particles are dominated by the largest-scale eddies, they are not as susceptible to "seeing" the spurious interaction of the kinematic motions over a broad range of scales, and consequently the reproduced KS field is more faithful to the DNS original, *from the perspective of the particles.*

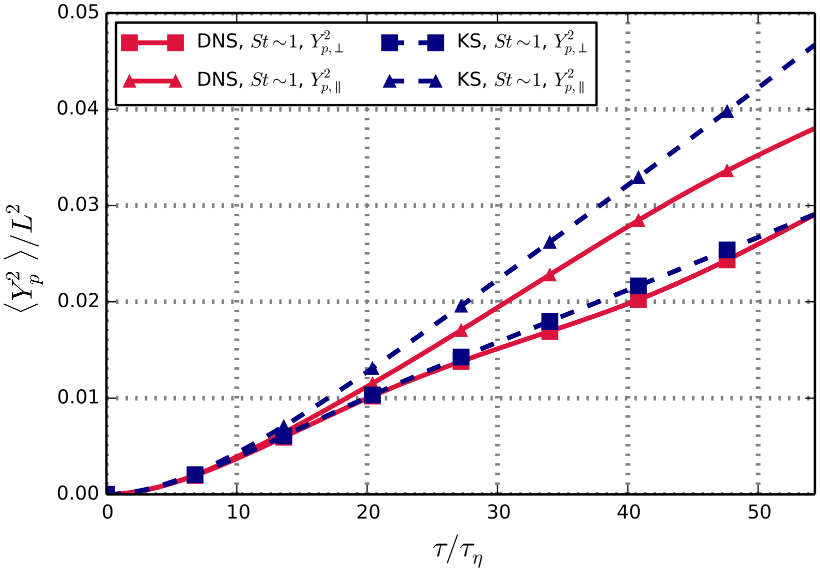

Figure 4.17: Lateral ($\langle Y^2_{p,\perp}\rangle$) and longitudinal ($\langle Y^2_{p,\parallel}\rangle$) dispersion, for $St\sim1$ particles, with gravity.

4.4 Inertial particles, with gravity

4.4.1 Single-particle Lagrangian statistics

The results for longitudinal and lateral (mean-drift-corrected) dispersion of $St\sim1$ inertial particles, in both DNS and KS, are shown in Fig. 4.17. There exists a clear reduction in lateral dispersion compared with longitudinal for steady ($\lambda = 0$) KS, indicating that KS indeed qualitatively reproduces the continuity effect. The corresponding DNS case is shown for comparison, though the nonlinear character of these dispersion histories indicates that any quantitative match between DNS and KS should be treated with extreme caution, since the lateral vs longitudinal dispersion in DNS is strongly influenced by the particular orientation of the large scales, over the times for which the DNS was run.

KS appears to yield a more favourable comparison of $\overline{\mathcal{D}}_2$ over the range of St (Fig.

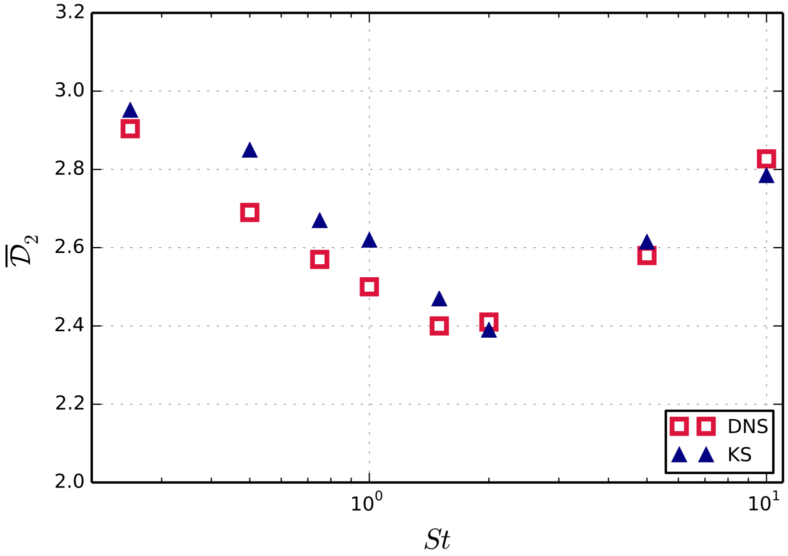

Figure 4.18: Correlation dimension as a function of St, with gravity, for DNS and steady ($\lambda = 0$) KS.

4.18), as compared with the case without gravity. As was noted in the no-gravity case, increasing particle inertia appears to reduce the sensitivity of particle behaviour to the spurious Lagrangian properties of a KS field, and drift appears to enhance this corrective effect.

It is well-documented in numerical results (Wells & Stock (1983); Hennick & Lightstone (2000)) and experimental results (Snyder & Lumley (1971)) that, in the presence of gravity, particle inertia causes a *reduction* in lateral dispersion, compared to fluid tracers, and indeed the lateral dispersion is inversely proportional to St - this is the opposite of the effect of particle inertia on dispersion in the no-gravity case (Fig. 4.10 for DNS and 4.11 for KS). The lateral dispersion of inertial particles is shown in Fig. 4.19 for DNS and in Fig. 4.20 for KS. There appears to be some evidence of the crossing trajectories effect (the reduction of dispersion in proportional to St) in the DNS, though the trend is less clear in steady KS - these results should also be treated

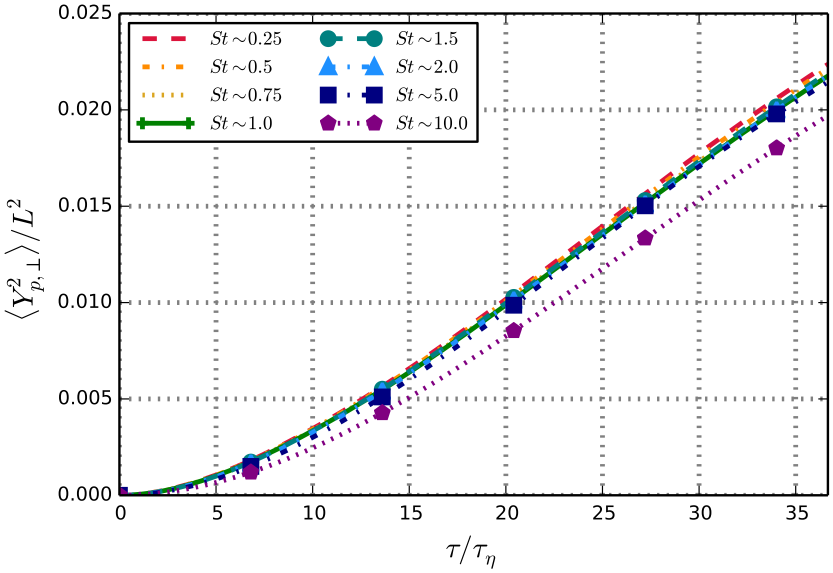

Figure 4.19: Lateral dispersion ($\langle Y_{p,\perp}^2\rangle$) vs St in DNS

with caution, since gravity was varied according to Stokes number, in order to enforce a target drift velocity. The trends observed in the aforementioned investigations are for particles experiencing the same body force - this condition is satisfied in the KS in Sec. 5.2, and indeed the reduction of lateral dispersion in proportion to St is observed.

In the case of high mean drift, the correlation of drift-normal fluid velocities conditioned on the (drifting) inertial particle locations ($R_\perp^{f|p}$) becomes dominated by the spatial component (by Taylor's frozen turbulence hypothesis), which is given as the one-time, two-point Eulerian velocity autocorrelation in the direction of the mean drift (mathematically, $R_{11}^E(r\mathbf{e}_3/(u_d\tau_\eta)$ - see Sec. B.3 for more information on this quantity), where u_d is the enforced drift speed ($u_d = 0.1$, which exceeds $u_{rms} = \sqrt{(2/3)k}$) and $\mathbf{e}_3$ is the unit vector in the downward direction - see Fig. 4.21). Again KS enforces *spatial* statistics of the DNS, hence the domination of autocorrelations

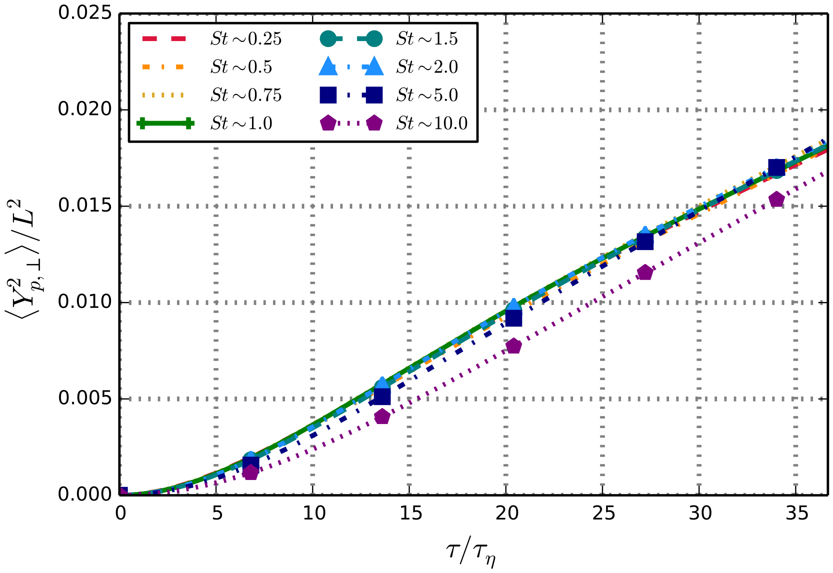

Figure 4.20: Lateral dispersion ($\langle Y^2_{p,\perp}\rangle$) vs St in steady KS

by the spatial component consequently improves the prediction of dispersion (see Fig. 4.22). Loosely speaking, the drift causes the inertial particles to “see” similar turbulence structure between the KS and DNS, hence they exhibit similar dynamics.

4.4.2 Correlation dimension

This corrective effect of drift is also manifested in correlation dimension estimates; KS appears to yield a more favourable comparison of $\overline{\mathcal{D}}_2$ over the range of St, as compared with the case without gravity, which achieved reasonable comparison only for high St. This is consistent with the main theme in the observations of the Lagrangian statistics; the interaction of particles with eddies becomes dominated by the properties of the Eulerian spatial structure, hence there is a greater resemblance between the clustering mechanisms in DNS and KS, and KS predictions of correlation dimension are improved.

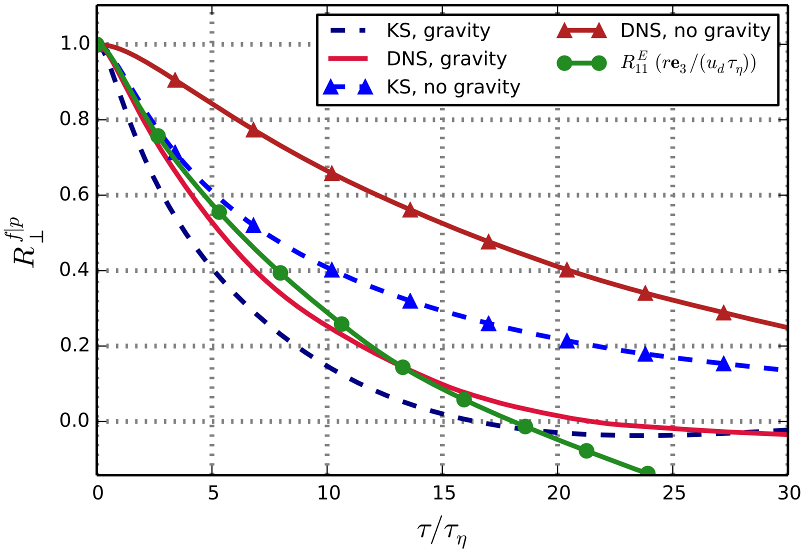

Figure 4.21: $R_\perp^{f|p}$ for $St \sim 1$ inertial particles, for DNS and steady KS in gravity, alongside $R_{11}^E(r\mathbf{e}_3/(u_d\tau_\eta))$.

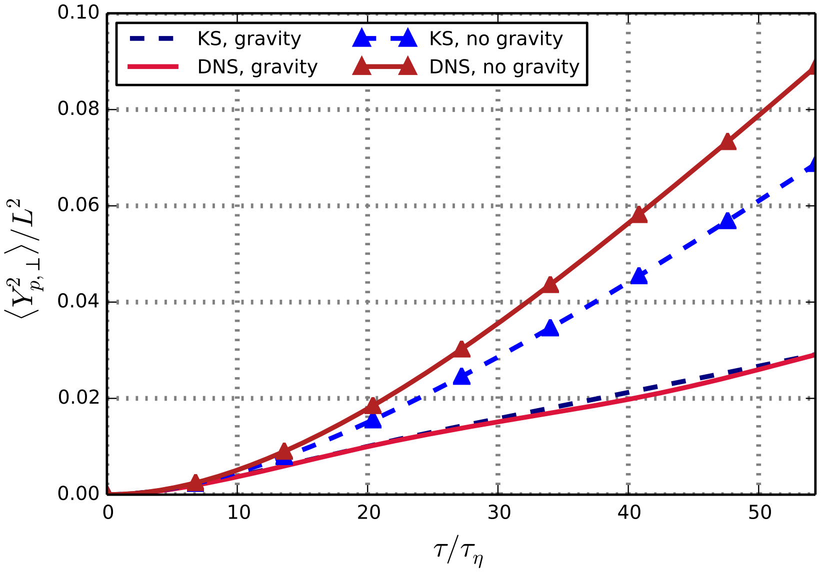

Figure 4.22: Lateral dispersion for $St \sim 1$ inertial particles, for DNS and steady KS, with and without gravity.

4.5 Discussion and further questions

The following is a summary of the results so far:

- KS qualitatively reproduces the turbulence structure, as it is manifested in intermittent velocity histories, the reduction of lateral diffusivity vs longitudinal diffusivity (the continuity effect), the elevation of the dispersion of inertial particles over tracers in the absence of gravity, and preferential concentration.

- The unsteadiness formalism negatively impacts predictions of single-particle Lagrangian statistics and structure; indeed the disparity between DNS and KS dispersion as well as correlation dimension is roughly proportional to the unsteadiness parameter λ. If KS is to be applied as a modelling tool for all scales of turbulent motion, λ can be dispensed with as a parameter, due to the open streamline topology of even steady KS fields (this was suggested in Malik (1996)).

- KS appears to hold particular utility for simulating high-St inertial particles exhibiting a mean drift, since particles “see” similar dynamics between the two cases.

Some results show close *quantitative* agreement between DNS and steady ($\lambda = 0$) KS, though some remarks of caution are warranted. In real turbulence, the manner in which Eulerian scales map to the Lagrangian scales is highly opaque, and is itself the subject of much literature. This appears to be true of KS as well, however the manner in which Eulerian scales map to Lagrangian scales is different between DNS and KS, as evidenced by the differing autocorrelations. When inertial particles “see” the narrower range of interacting Eulerian scales, the mapping to Lagrangian scales in DNS and

KS appears to converge - this suggests that the broader the range of scales seen by the inertial particles, the more the kinematic motions spuriously manifest themselves in the Lagrangian statistics. This suggests further that for broader inertial ranges than are tested here, the comparison between Lagrangian timescales in DNS and KS is likely to be less favourable. It is also noted that, like many other similar investigations, only one DNS benchmark was employed, which grants only an approximation of homogeneous, isotropic, stationary turbulence.

The ultimate goal is to develop KS as a modelling tool, and it should be remembered that in practice, one does not have the luxury of knowing the precise input spectrum. While one can estimate the shape of the Eulerian spectrum (with particular appeal to the Kolmogorov “five-thirds” scaling property of the spectrum in the inertial range), it is shown here and elsewhere (Malik & Vassilicos (1999)) that the Lagrangian statistics are highly sensitive to how to the largest scales are handled, the behaviour of which is far from universal and is consequently difficult to estimate. At first glance this is all bad news, however the previous analysis suggests that the ability of KS to recover the Lagrangian statistics of turbulence does not hinge upon realistic Eulerian statistics.

Chapter 5

Target Lagrangian Integral Timescale Kinematic Simulation (TLKS)

5.1 Motivation and formulation

The fundamental barrier to the broader applicability of KS as a modelling tool appears to be its inability to reproduce the correct Lagrangian timescales (even if the correct Eulerian second-order statistics are known - and in practice, they are not). Supposing one possesses some other means of reasonably estimating at least one property of the Lagrangian statistics (namely the Lagrangian integral timescale, T_L, as is common for SSF models), the more appropriate question might be as follows:

- For a target T_L, what is an appropriate choice of *input spectrum* for KS that recovers T_L?

At first glance, the knowledge of such a hypothetical input spectrum appears superfluous, since, if successful, it would simply recover the input T_L as output. But the results so far suggest that such a KS formulation would, in some sense, reproduce additional phenomena (for example, the continuity effect), in addition to recovering just T_L. Loosely speaking, with KS there exists the prospect of a "return on investment", which SSF approaches lack.

A method is sought, whose basic outline is given as follows:

- Step 1: Based on RANS statistics (turbulent kinetic energy (k) and the negative of its dissipation rate (ϵ)), estimate T_L;
- Step 2: For the target T_L and RANS parameters (k and/or ϵ), choose an appropriate Eulerian energy spectrum;
- Step 3: Use the *output* from Step 2 as input for the traditional KS method. If successful, T_L will be recovered, along with other statistics of interest.

This method will be referred to as *Target Lagrangian integral timescale Kinematic Simulation* (TLKS).

Fortunately Step 1 is already the topic of a great deal of literature, since this task is also a component of SSF methodologies. One particularly widely applied version is that of Zhou & Leschziner (1991), and is given as:

$$T_L = \beta \left(C_\mu^{0.75} \frac{k^{1.5}}{\epsilon} \right) \Big/ \left(\frac{2}{3} k \right)^{0.5} \tag{5.1}$$

and where $\beta = 0.8$ and $C_\mu = 0.09$. This method will be applied here.

It is less clear just how Step 2 should operate. How can an Eulerian spectrum be reverse engineered from T_L? At first glance, it is tempting to inform Step 2 by

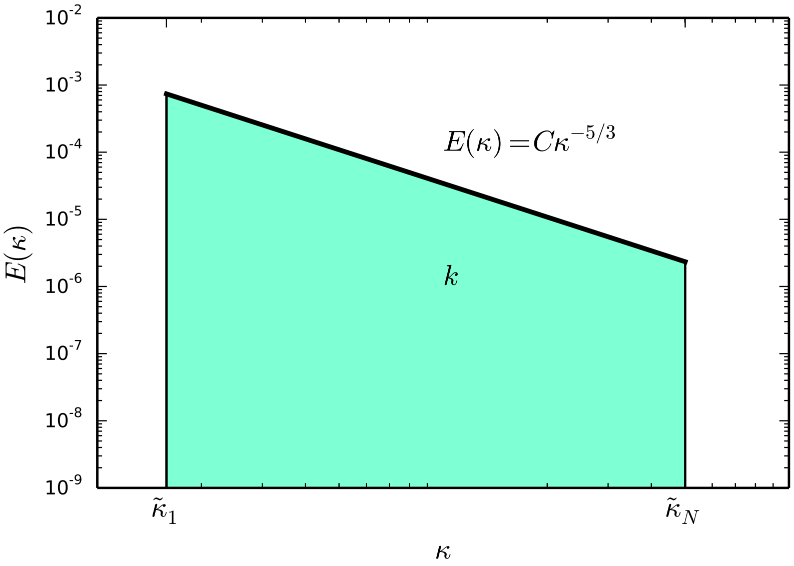

Figure 5.1: Energy spectrum, determined by the parameters k (or equivalently u_{rms}), $\tilde{\kappa}_1$, and $\tilde{\kappa}_N$

some link between Eulerian and Lagrangian statistics which is elucidated analytically. Unfortunately, the nonintegrability of streamlines in even simple kinematically defined fields suggests that any *a priori* connection between Eulerian and Lagrangian statistics in KS is opaque, just as it is for real turbulence.

In the absence of a clear analytical bridge between Eulerian and Lagrangian properties, the appropriate strategy appears to be to develop an *empirical* relationship by which some parameters pertaining to the output of Step 2 (input for Step 3) can be related to a target T_L. It is not immediately obvious what canonical form the Eulerian spectrum should be assumed to exhibit, and what the degrees of freedom should be. At the very least, spectra are characterized by the following properties:

- $\tilde{\kappa}_1$, smallest wavenumber of turbulent-like "cascade"
- $\tilde{\kappa}_N$ highest wavenumber of the cascade

- u_{rms}, root-mean-squared velocity (related to energy as $\frac{3}{2}u_{rms}^2 = k$)

It is assumed that the inertial range slope (in log-log coordinates) of such a spectrum adheres to the classical Kolmogorov scaling ($E(\kappa) \sim \kappa^{-5/3}$). Such a spectrum is visualized in Fig. 5.1. Once again, the input of any KS method is a sequence of wavenumbers, κ_n, the lowest wavenumber of which is κ_1, and the highest is κ_N, whereas $\tilde{\kappa}_1$ and $\tilde{\kappa}_N$ describe the bounds over which the simple spectrum (as depicted in Fig. 5.1) is assumed to be nonzero. It may appear superfluous to have $\kappa_1 < \tilde{\kappa}_1$ or $\kappa_N > \tilde{\kappa}_N$ (since such modes outside of the support would simply contribute zero energy), but choosing a wider than necessary sequence of input wavenumber provides flexibility in the event that $\tilde{\kappa}_1$ and $\tilde{\kappa}_N$ change - the need for such an accommodation becomes apparent in the inhomogeneous flow described in Sec. 5.2.2. There exist a variety of justified objections over the realism of such a spectrum; indeed real energy spectra exhibit a continuous rise and fall versus wavenumber, which, as seen in Fig. 5.1, is flagrantly violated at $\tilde{\kappa}_1$ and $\tilde{\kappa}_N$. Again, *synthesizing a flow whose Eulerian properties are realistic is not the primary objective of a stochastic Lagrangian particle model.* The objective is to map simple spectra to Lagrangian timescales, such that, for a target Lagrangian timescale, an appropriate Eulerian spectrum can be constructed that *recovers* the Lagrangian timescale.

5.1.1 Methodology for TLKS formulation

More precisely, the objective is to infer a relationship between the properties of a simple Eulerian spectrum (given by $\tilde{\kappa}_1$, $\tilde{\kappa}_N$, and u_{rms}) and the Lagrangian properties of the turbulent-like field (in particular T_L). In order to establish such a relationship, a variety of KS were carried out, all with simple spectra (visualized in Fig. 5.1), for

Sim.	u_{rms}	$\tilde{\kappa}_1$	Sim.	$\tilde{\kappa}_N/\tilde{\kappa}_1$
P	0.105	8	1	10^4
Q	0.105	7.5	2	$10^{3.75}$
R	0.105	7	3	$10^{3.5}$
S	0.105	6.5	4	$10^{3.25}$
T	0.075	7.76	5	10^3
U	0.085	7.76	6	$10^{2.75}$
V	0.095	7.76	7	$10^{2.5}$
W	0.105	7.76	8	$10^{2.25}$
			9	10^2
			10	$10^{1.75}$

Table 5.4: Parameters of KS simulations. The input spectrum is determined by u_{rms}, $\tilde{\kappa}_1$ and $\tilde{\kappa}_N$, hence a given simulation is determined by a letter and a numeral. For example, simulation V7 denotes $u_{rms} = 0.085$, $\tilde{\kappa}_1 = 7.76$ and $\tilde{\kappa}_N = 7.76 \times 10^{2.5} \approx 2454$.

a variety of input parameters, $\tilde{\kappa}_1$, $\tilde{\kappa}_N$, and u_{rms}. The parameters of each simulation are summarized in Table 5.4. Since there is no such requirement that particles "see" the same turbulent-like field, as would be the case when preferential concentration is of interest, every fluid tracer was assigned independent sequences $\mathbf{a}_n$ and $\mathbf{b}_n$ (see Eq. (2.13)) - in other words, every tracer experienced a unique turbulent-like "field". For each simulation, 300 000 tracers were tracked, to ensure confidence in Lagrangian statistics. Since the wider inertial ranges considered here are larger than that considered in Ch. 4, a longer sequence of wavenumbers, κ_n, is required to ensure isotropy and convergence of T_L (see Sec. D.3).

At first glance, it may appear that a spectrum defined by u_{rms}, $\tilde{\kappa}_1$ and $\tilde{\kappa}_N$ (visualized in 5.1) is overdetermined by the parameters, but this is not the case. To see how such a spectrum is constructed, first note that the formal expression of such a simple “cascade” is:

$$E(\kappa_n) = \begin{cases} c\kappa_n^{-5/3} & \text{if } \tilde{\kappa}_1 \leq \kappa_n \leq \tilde{\kappa}_N \\ 0 & \text{otherwise} \end{cases} \tag{5.2}$$

for some constant c. For such a spectrum, the total energy is given as:

$$k = c \int_{\tilde{\kappa}_1}^{\tilde{\kappa}_N} \kappa^{-5/3} \, d\kappa \tag{5.3}$$

For a KS simulation, the discrete version of (5.3) is applied:

$$k = c \sum_{n=1}^{N_\kappa} \kappa_n^{-5/3} \Delta\kappa_n \tag{5.4}$$

Therefore, for a given $\tilde{\kappa}_1$ and $\tilde{\kappa}_N$, the appropriate choice of c is one for which k is enforced:

$$c = k \Big/ \Big[\sum_{n=1}^{N_\kappa} \kappa_n^{-5/3} \Delta\kappa_n \Big] \tag{5.5}$$

Indeed the same strategy is employed in Osborne *et al.* (2005). In particular, for $\tilde{\kappa}_N \to \infty$, and assuming a sufficiently dense sequence of wavenumbers:

$$E(\kappa_n) = u_{rms}^2 \tilde{\kappa}_1^{2/3} \kappa_n^{-5/3} \tag{5.6}$$

for $\kappa_n > \tilde{\kappa}_1$ and 0 otherwise. Note that when the left-hand side of (5.6) is integrated from 0 to ∞, it yields k (by definition). When the right-hand side is integrated in the same manner, it yields $\frac{3}{2}u_{rms}^2$, as expected.

For the analysis in the previous chapters, an arithmetic sequence of input wavenumbers, κ_n, was assumed, and the method of weighting each KS mode was adjusted, all to allow the KS method to use the discrete-domain energy spectrum from the DNS. Since such considerations are not present here, a geometrically defined sequence of wavenumbers is assumed:

$$\kappa_n = \kappa_1 \left(\frac{\kappa_N}{\kappa_1} \right)^{(n-1)/(N-1)} \tag{5.7}$$

and also the traditional method for distributing the energy amongst the KS modes (given in (2.15)) is once again assumed.

5.1.2 Results

To begin, some general results for single-particle Lagrangian statistics in KS are shown, as a complement to the results in Ch. 4. As stated previously in Sec. 4.2.2, the Lagrangian structure function scaling $S^L(\tau) \sim \tau^{2/3}$ has been reported in the KS literature, though such a scaling was not convincingly reproduced in Ch. 4 (as shown in Fig. 4.6), due to the narrow inertial range. The simulations here exhibit a greater separation of scales (i.e. there exists a larger ratio between the largest and smallest resolved wavenumbers), hence it is of interest whether the expected scaling of $S^L(\tau)$ is restored in such cases. $S^L(\tau)$ is shown for selected simulations in Fig. 5.2 (simulations P1, P4, P7 and P10, all described in Table 5.4), and indeed the 2/3 scaling appears to be restored for a wide range of time scales - in fact, the higher $\tilde{\kappa}_N/\tilde{\kappa}_1$, the greater the interval over which the $S^L(\tau) \sim \tau^{2/3}$ scaling appears to be valid. The restoration of the expected scaling for steady KS (as observed in Fung *et al.* (1992); Khan & Vassilicos (2003); Osborne *et al.* (2005)) provides further confidence in the numerical tools.

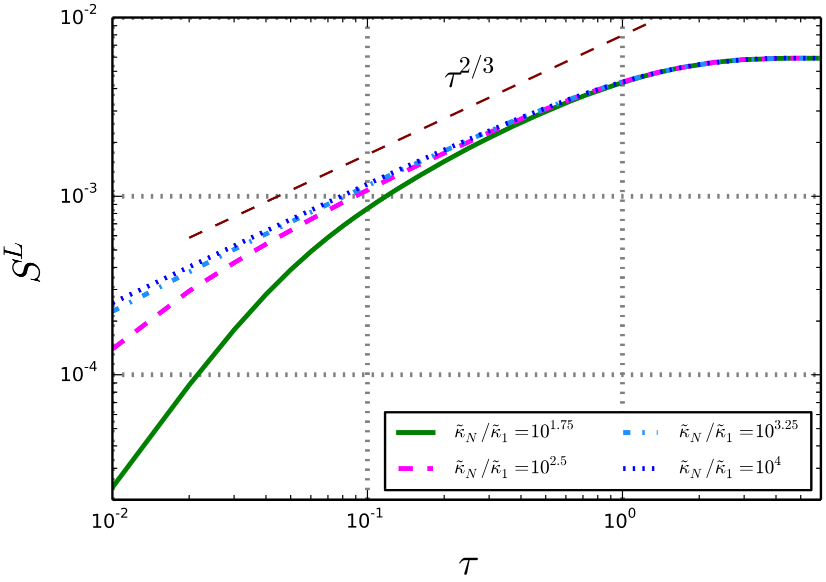

Figure 5.2: Lagrangian structure function, for selected KS cases (P1, P4, P7, P10), with varying $\tilde{\kappa}_N/\tilde{\kappa}_1$. Shown for comparison is $\tau^{2/3}$.

In Fig. 5.3, R^L is shown for the same selected cases, and for higher $\tilde{\kappa}_N/\tilde{\kappa}_1$, the autocorrelation appears to converge to a fixed form. Indeed such a convergence is expected; the addition of energy at ever smaller scales corresponds to a decrease in the marginal effect on particle dynamics. Beyond the ballistic range, the decay appears to be well approximated by $C_0(\tau - \tau^*)^6$, for some appropriate choice of C_0 and τ^*.

For the spectrum in the simulation P1, the *Eulerian velocity autocorrelation*, $R^E_{ii}(r)$, was evaluated (see Sec. B.3 for a definition), and is shown in Fig. 5.4. The Lagrangian autocorrelation is also plotted as a function of the scaled variable $\tilde{\tau} = \tilde{u}\tau$, where $\tilde{u} = \frac{1}{2}u_{rms}$. In the near range of times/separations, agreement is excellent, whereas for large times/separations, the Lagrangian autocorrelation exhibits $(\tau - \tau^*)^6$ decay, and the spatial autocorrelation exhibits a negative loop.

These results suggest the possibility that the Lagrangian autocorrelation can be

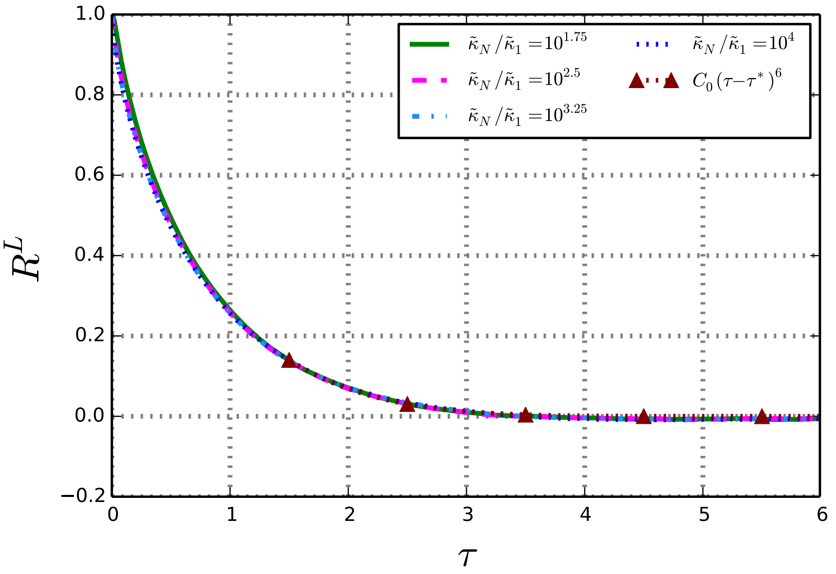

Figure 5.3: Lagrangian autocorrelation, for the same selected KS cases (with varying $\tilde{\kappa}_N/\tilde{\kappa}_1$). Shown for comparison is $C_0(\tau - \tau^*)^6$.

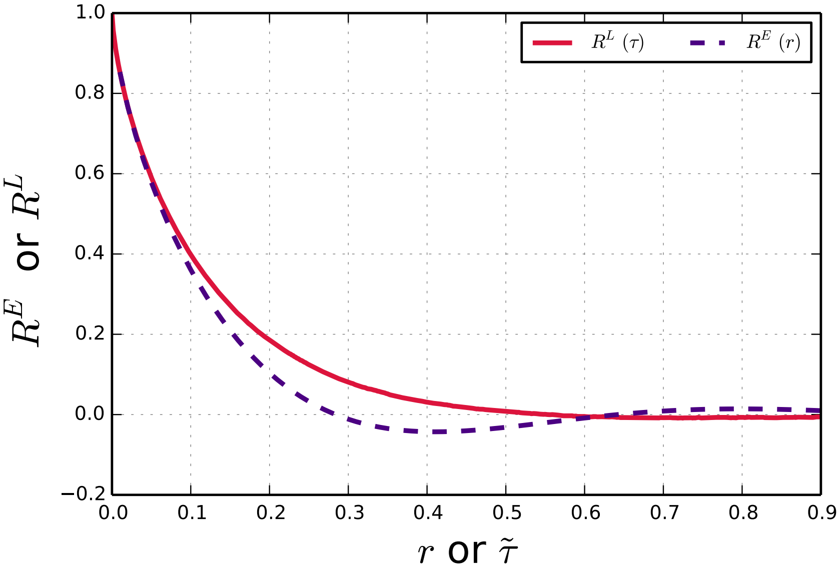

Figure 5.4: Eulerian autocorrelation, derived from the spectrum used in Sim. P1. Also shown is the Lagrangian autocorrelation for P1, as a function of a scaled time variable, $\tilde{\tau}$.

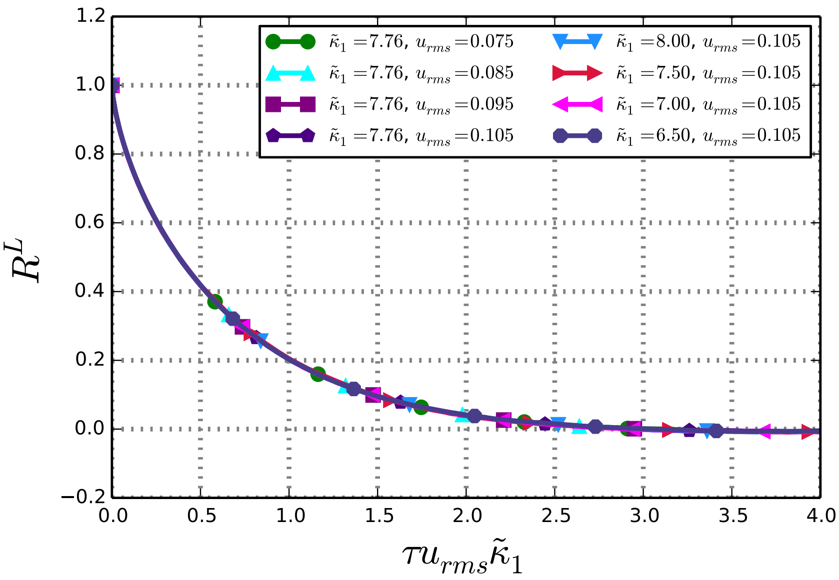

Figure 5.5: R^L vs non-dimensionalized time, for a variety of u_{rms} and $\tilde{\kappa}_1$. In all cases, $\tilde{\kappa}_N/\tilde{\kappa}_1 = 10^4$.

derived analytically from the input $E(\kappa)$, in the case of high $\tilde{\kappa}_N/\tilde{\kappa}_1$, but further investigation on this matter is left for future work. Nonetheless, perhaps a link between Eulerian and Lagrangian statistics can be established empirically. For a variety of wide inertial range cases ($\tilde{\kappa}_N/\tilde{\kappa}_1 = 10^4$), the Lagrangian autocorrelation is shown as a function of non-dimensionalized time, $tu_{rms}\tilde{\kappa}_1$ (Fig. 5.5). In all cases, the curves are nearly indistinguishable. This suggests that an appropriately non-dimensionalized Lagrangian integral timescale will converge to a fixed value, for sufficiently large $\tilde{\kappa}_N/\tilde{\kappa}_1$.

To find such a relationship, T_L was evaluated via numerical integration of $R^L(\tau)$ (by 2.25) for a variety of simulations with varying $\tilde{\kappa}_N/\tilde{\kappa}_1$, and varying u_{rms}. The non-dimensionalized timescale $T_L u_{rms}\tilde{\kappa}_1$ is shown as a function of $\tilde{\kappa}_N/\tilde{\kappa}_1$. In the same way that an increase in $\tilde{\kappa}_N/\tilde{\kappa}_1$ engenders a convergence in autocorrelation (Fig. 5.3), the increase in $\tilde{\kappa}_N/\tilde{\kappa}_1$ accordingly engenders a convergence of $T_L u_{rms}\tilde{\kappa}_1$ to a fixed value (approximately 0.58), and this appears to be independent of u_{rms} (Fig. 5.6). Similarly, $T_L u_{rms}\tilde{\kappa}_1$ was plotted for a variety of $\tilde{\kappa}_N/\tilde{\kappa}_1$ and $\tilde{\kappa}_1$, and $T_L u_{rms}\tilde{\kappa}_1$ appears to converge to nearly the same fixed value, regardless of $\tilde{\kappa}_1$ (Fig. 5.7). Thus for the wide inertial range case, (i.e. $\tilde{\kappa}_N/\tilde{\kappa}_1 > 10^3$), the following relationship is suggested:

$$T_L u_{rms}\tilde{\kappa}_1 = 0.58 \tag{5.8}$$

In Fung *et al.* (1992), it was observed that:

$$\frac{T_L u_{rms}}{L_E} \approx 0.5 \tag{5.9}$$

The Eulerian lengthscale for isotropic turbulence is given as (Monin & Yaglom (1975)):

$$L_E = \frac{3\pi}{4}\frac{\int_0^\infty \kappa^{-1}E(\kappa)\,d\kappa}{\int_0^\infty E(\kappa)\,d\kappa} \tag{5.10}$$

It follows from (5.6) and (5.10) that, for the wide inertial range KS employed here:

$$\frac{T_L u_{rms}}{L_E} = 0.62 \tag{5.11}$$

which differs from the estimate of Fung *et al.* (1992). An exact match is perhaps not expected, since the application of KS here differs from that of Fung *et al.* (1992) in a variety of key respects; they employed a narrow inertial range, and enforced unsteadiness. But nonetheless this provides some confidence in the relation (5.8). It is emphasized that neither the approach here nor that of Fung *et al.* (1992) is necessarily "correct"; it is conceivable that, for the method of Fung *et al.* (1992), a similar link between *input* Eulerian parameters and *output* Lagrangian statistics could

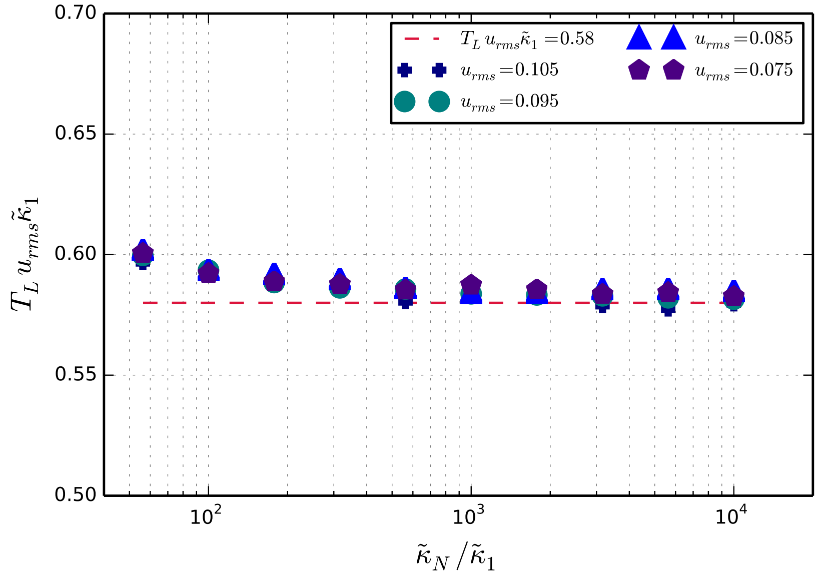

Figure 5.6: non-dimensionalized Lagrangian integral timescale, as a function of inertial range width ($\tilde{\kappa}_N/\tilde{\kappa}_1$) for a variety of u_{rms}.

also be formalized. The advantage of TLKS as developed here is that it achieves the desired Lagrangian timescale with few inputs.

To summarize, it was observed in Ch. 4 that KS qualitatively recovers a variety of important features of a particle ensemble, though it fundamentally lacks the ability to reproduce Lagrangian timescales. A novel method has been motivated for bridging the gap between Eulerian and Lagrangian statistics in KS; the TLKS model. The foundation of this method is relation (5.8), which, for a target T_L (and for a known u_{rms}), allows a spectrum to be constructed which recovers T_L. Whether this Eulerian spectrum is realistic is secondary; what matters is that it yields a turbulent-like field with particular Lagrangian properties. To assess the broader applicability of TLKS, it must be tested against a benchmark for which there exists hallmarks of turbulence structure beyond simply T_L for fluid tracers - for instance, the crossing trajectories and continuity effects.

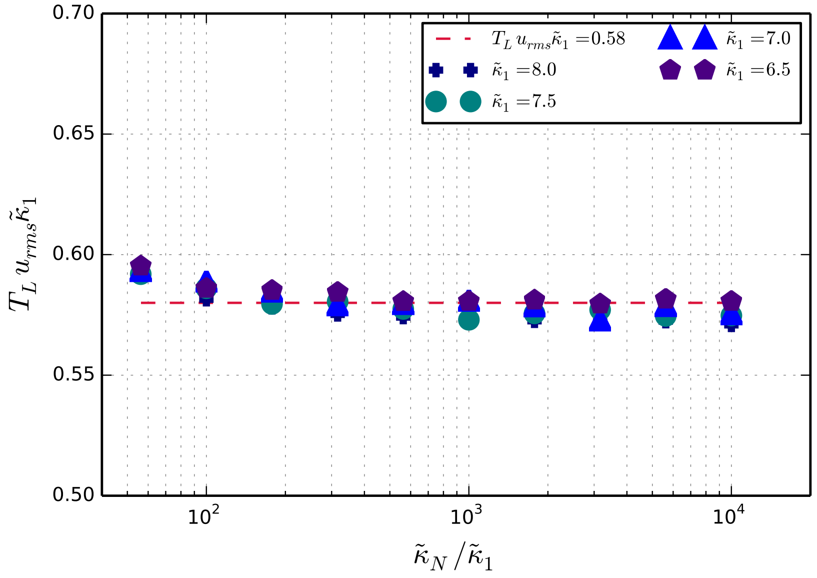

Figure 5.7: non-dimensionalized Lagrangian integral timescale, as a function of inertial range width ($\tilde{\kappa}_N/\tilde{\kappa}_1$), for a variety of $\tilde{\kappa}_1$.

5.2 Comparison to experimental results of Snyder & Lumley (1971)

5.2.1 Overview

One of the seminal experiments on the Lagrangian properties of inertial particles in turbulence is that of Snyder & Lumley (1971) (hereafter referred to as SL71). In this experiment, particles (with a variety of relaxation times) were released into grid-generated, decaying turbulence, and the particles' lateral position was recorded at regular intervals throughout a test section. See Fig. 5.8 for an illustration. In addition to dispersion, the authors extensively catalogued the turbulence statistics throughout the test chamber (which can be used as input for the TLKS), allowing for a robust assessment of the proposed TLKS model.

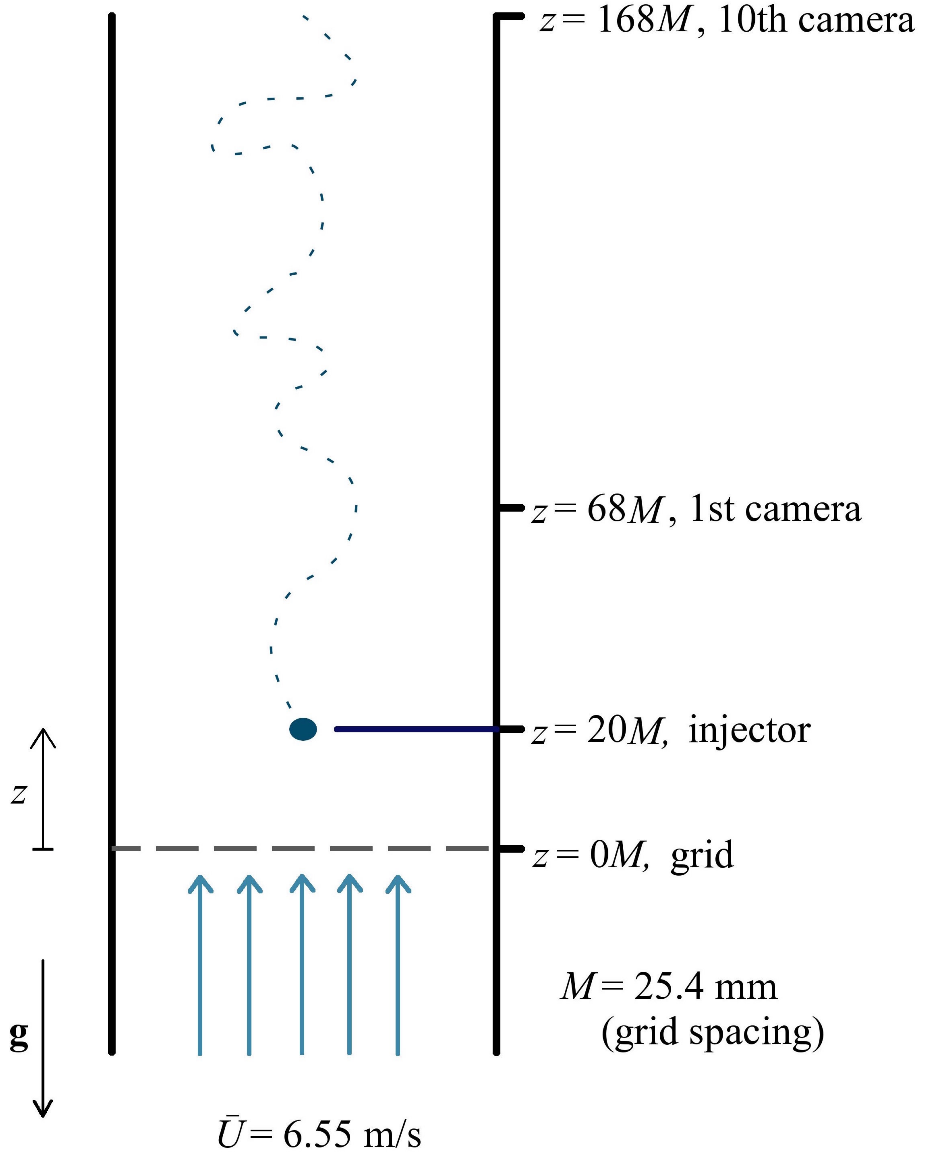

Figure 5.8: Schematic of the SL71 experiment. Particles were injected into grid-generated, spatially-decaying turbulence. Their lateral position was measured by 10 cameras placed along the wind tunnel.

Particle	d_p [m]	ρ_p [kg m^{-3}]	St	u_d [m s^{-1}]	Δt [s]
Hollow glass	4.65×10^{-5}	260	0.138	0.01635	0.001
Solid glass	8.7×10^{-5}	2500	4.64	0.437	0.01
Corn pollen	8.7×10^{-5}	1000	1.86	0.1932	0.001
Copper	4.65×10^{-5}	8900	4.72	0.477	0.01

Table 5.5: Particle properties in SL71. d_p is particle diameter, ρ_p is particle density, St is Stokes number, u_d is terminal velocity, and Δt is simulation timestep. The Stokes numbers are based on a Kolmogorov timescale of $\tau_\eta = 1.17 \times 10^{-2}$ m (evaluated at 73 grid spacing lengths downstream of the grid), a kinematic viscosity of $\nu = 1.5 \times 10^{-5}$ m^{2}s^{-1} and a fluid density of $\rho_f = 1.225$ kg m^{-3}.

5.2.2 Methodology for comparison to SL71

Since only the single-particle Lagrangian statistics were examined, Type I (unbounded domain) KS was employed. In SL71, four particle types were employed: copper, corn pollen, solid glass and hollow glass. The particle properties are summarized in Table 5.5.

There exist two features of the turbulence in the SL71 experiment that necessitate some mild changes in the KS method: mean flow and spatial decay.

Mean flow

The transport of turbulent eddies by the mean flow is incorporated into the traditional KS model with an appropriate change of variables:

$$\mathbf{u}_f(\mathbf{x}, t) = \sum_{n=1}^{N_\kappa} \mathbf{a}_n \cos(\boldsymbol{\kappa}_n \cdot \mathbf{X} + \omega_n t) + \mathbf{b}_n \sin(\boldsymbol{\kappa}_n \cdot \mathbf{X} + \omega_n t) \tag{5.12}$$

where $\mathbf{X} = \mathbf{x}_0 - \mathbf{U}t$, and where $\mathbf{U}$ is the mean flow vector. This is reminiscent of the *Kinematic Simulation Sweeping Model* of Fung *et al.* (1992). This parallel is discussed further in Ch. 6.

Spatial decay

Among the immense variety of statistics recorded in SL71 is the spatial variation of the root mean squared lateral component of the turbulent fluctuating velocity in the test chamber ($\overline{u_\perp^2}$), as a function of vertical position:

$$\frac{\bar{U}^2}{\overline{u_\perp^2}} = 39.4\Big(\frac{z}{M} - 12\Big) \tag{5.13}$$

where M is the grid spacing (2.54 $\times 10^{-2}$ m), $\bar{U}$ is the magnitude of the mean velocity (6.55 m s^{-1}), z is vertical position, and the overline denotes the Eulerian time average. Similarly the dissipation profile is given by:

$$\epsilon = -\overline{U}\frac{d}{dz}k \tag{5.14}$$

where the derivative is with respect to displacement along the length of the test chamber. Since the objective is to reproduce lateral dispersion, the energy is assumed to be given as:

$$k = \frac{3}{2}\overline{u_\perp^2} \tag{5.15}$$

and consequently Eq. (5.14) becomes:

$$\epsilon = -\overline{U}\frac{3}{2}\frac{d}{dz}\left[\frac{\bar{U}^2}{39.4\Big(\frac{z}{M} - 12\Big)}\right] \tag{5.16}$$

Since k and ϵ vary according to position, so does the estimate for T_L (by Step 1 of the TLKS), and accordingly so do the estimates for $\tilde{\kappa}_1$ and $E(\kappa_n)$ (by Step 2 of the TLKS).

Therefore, the turbulence statistics for a given particle are a function of that particle's precise streamwise position. Consequently, the TLKS is applied *independently* for each particle, such that every particle "sees" its own TLKS spectrum, constructed as follows:

$$\mathbf{u}_f(\mathbf{x}, t) = \sum_{n=1}^{N_\kappa} \mathbf{a}_n(z) \cos(\boldsymbol{\kappa}_n \cdot \mathbf{X} + \omega_n t) + \mathbf{b}_n(z) \sin(\boldsymbol{\kappa}_n \cdot \mathbf{X} + \omega_n t) \tag{5.17}$$

where

$$|\mathbf{a}_n(z)|^2 = |\mathbf{b}_n(z)|^2 = 2E(\kappa_n, z)\Delta\kappa_n \tag{5.18}$$

and where, by (5.13) and (5.15):

$$\sum_{n=1}^{N_\kappa} E(\kappa_n, z)\Delta\kappa_n = k(z) = \frac{\bar{U}^2}{\frac{2}{3}39.4\left(\frac{z}{M} - 12\right)} \tag{5.19}$$

Again since the sequences $E(\kappa_n, z)$ depend on streamwise position (z), they will be unique for each particle. In contrast, a single wavenumber sequence, as well as weights (κ_n and $\Delta\kappa_n$ respectively) were assumed for all particles - individual modes were activated and deactivated according to $\tilde{\kappa}_1$ for the given particle. Naturally such an approach possesses the same shortcoming as SSF models; all particles seeing independent fluid velocities cannot exhibit clustering. This does not impact the present simulations, for which only Lagrangian statistics are observed. In all cases, $\tilde{\kappa}_N$ should be sufficiently large such that the relation (5.8) applies - to simplify matters, a single $\tilde{\kappa}_N$ can be chosen such that $\tilde{\kappa}_N/\tilde{\kappa}_1 > 10^3$ for all particles throughout the simulation.

To ensure particles' independence from the initial conditions in the original experiment, particles were released from the same initial point, and the collection of particle data commenced after the particles had traveled downstream a distance of 20

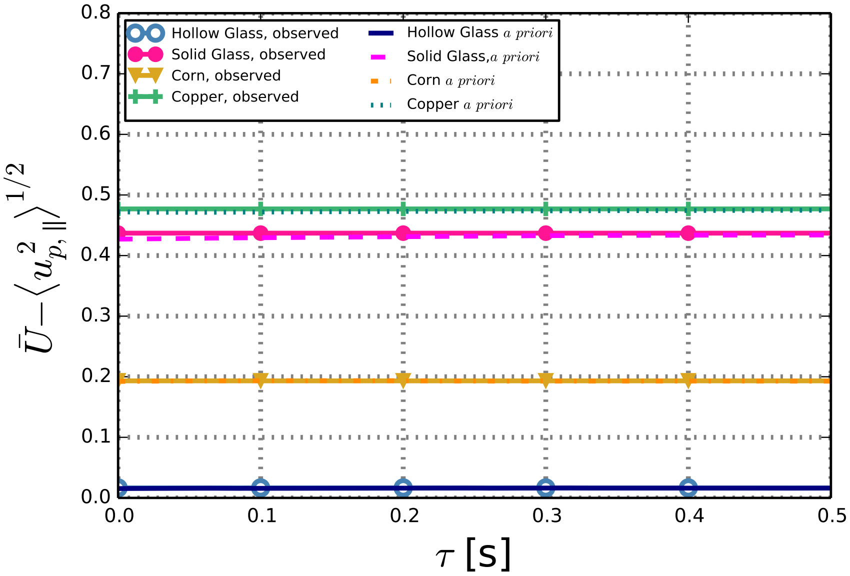

Figure 5.9: History of observed terminal velocities for a variety of particle types in TLKS-generated fields, compared with *a priori* estimates.

grid spacings. A similar strategy is employed here; an initial time for the evaluation of Lagrangian statistics, t^*, was estimated based on the particle terminal velocity (whose magnitude is given by u_d), which was evaluated from equations (2.7) (2.8), and (2.9) - see Sec. C.4. It was ensured that the average terminal velocity matched the *a priori* estimates throughout the simulation (See Fig. 5.9).

5.2.3 Results

The results of dispersion for a variety of particle types, compared with the experimental benchmarks, are shown in Fig. 5.10; indeed the comparison is remarkably good. In particular, the crossing trajectories effect (namely, reduced dispersion for high St particles) is observed. The mild discrepancy may, in part, be explained by the sample error of dispersion in the experiment. Following the method of Strutt *et al.* (2011), the confidence in dispersion results (as a function of number of particles sampled) is evaulated. In the *best case* in SL71, 846 corn pollen trajectories were tracked, and accordingly this corresponds to a 19.1% spread in the 95% confidence interval for dispersion. For all TLKS trials, 300 000 particles were tracked, corresponding to a 1% spread in the 95% confidence interval.

Though not observed in SL71, the longitudinal mean-corrected dispersion is shown in Fig. 5.11 (along with lateral dispersion), and the continuity effect is indeed captured for high St particles. As was predicted analytically (Csanady (1963)), and as was observed numerically (Squires & Eaton (1991)), the strength of the continuity effect (defined as the ratio of lateral diffusivity over longitudinal diffusivity) is roughly proportional to St, and in the limiting case of very high St, this ratio approaches $\frac{1}{2}$. This qualitative behaviour is recovered here (see Fig. 5.12).

The reciprocal of the mean-squared lateral particle velocity (non-dimensionalized by the square of the mean velocity) is shown in Fig. 5.13. The authors themselves noted: "The difference between the velocity of the glass and copper beads is somewhat surprising since their time constants were nearly the same and their dispersion curves were nearly identical. The tread [*sic*] however, is consistent." This mismatch between copper and solid glass is also reflected in the TLKS results. This is explained, in part, by the presentation of the data in reciprocal form; in Fig. 5.14 the non-reciprocal mean-squared lateral particle velocity is shown, and indeed the discrepancy between copper and hollow glass (for both SL71 and TLKS) appears less dramatic.

The generally loose agreement between SL71 and TLKS may be explained by the experimental uncertainty associated with position measurements, compounded with error introduced by the numerical evaluation of velocity in SL71. Their method is explained in detail in Ch. 5.2 of SL71, and is summarized here as follows: the mean-squared particle velocity (or particle "energy") was evaluated by observing the particle *position* data at the camera locations, and applying a filter to the Fourier coefficients of velocities, to compensate for energy lost due to the coarse sampling. The authors themselves noted: "It is likely that a significant portion of the energy of the hollow glass beads was lost due to the low sampling rate", explaining the discrepancy between the TLKS and SL71 for hollow glass. The discrepancy between TLKS and SL71 for heavy particles (solid glass and copper) is explained as follows: heavy particles exhibit low lateral dispersion, and consequently exhibit high relative (position) error. In turn, this is expected to amplify the error associated with numerical derivatives, likely causing an overestimate of such mean-squared lateral particle velocities. Notwithstanding these issues, it is borne in mind that such numerical errors are avoided in the more direct observation of dispersion, which is of primary interest. And it is here that good agreement is observed.

5.3 Summary

Perhaps the most fundamental expectation one can have of any worthwhile particle-laden flow model is whether it reproduces the expected Lagrangian integral timescale (T_L). Whether KS yields the desired T_L hinges upon whether one uses the "appropriate" input spectrum for KS, and in the literature there does not exist a systematic method for achieving this, based on the desired output T_L. Target Lagrangian integral timescale Kinematic Simulation (TLKS) was devised to address this need; the inputs of the method are RANS parameters (k and ϵ), which correspond to a certain T_L. This corresponds to a simple Eulerian spectrum (via an empirical relationship),

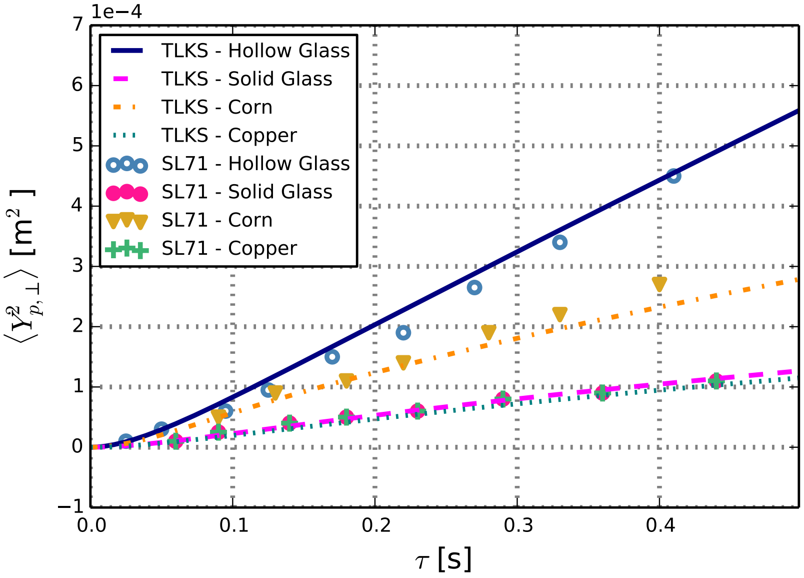

Figure 5.10: Dispersion for a variety of particle types in TLKS-generated fields, compared with the experimental results of SL71.

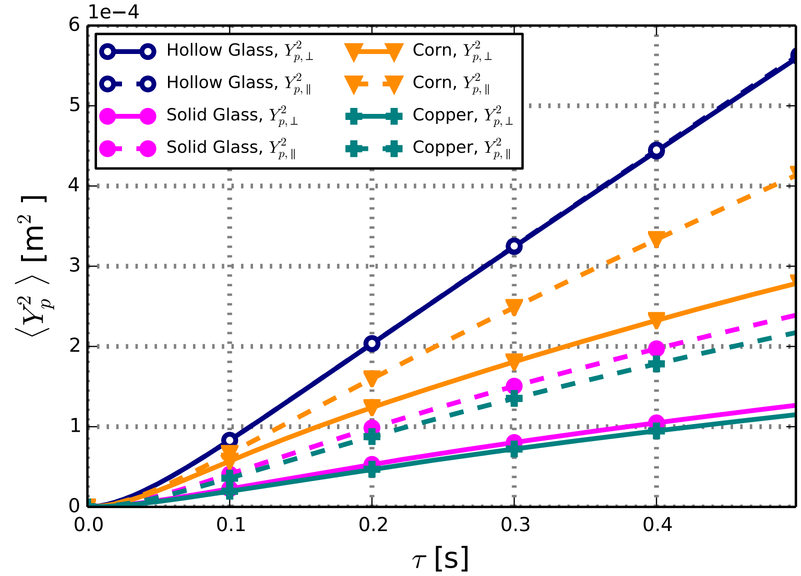

Figure 5.11: Lateral dispersion ($Y^2_{p,\perp}$) and mean-corrected longitudinal dispersion ($Y^2_{p,\parallel}$) for a variety of particle types in TLKS-generated fields.

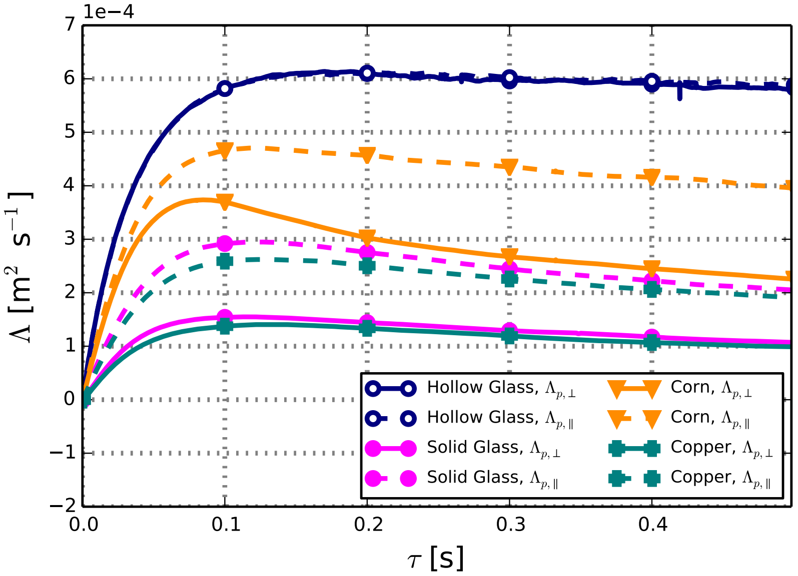

Figure 5.12: Lateral diffusivity ($\Lambda_{p,\perp}$) and mean-corrected longitudinal diffusivity ($\Lambda_{p,\parallel}$) for a variety of particle types in TLKS-generated fields.

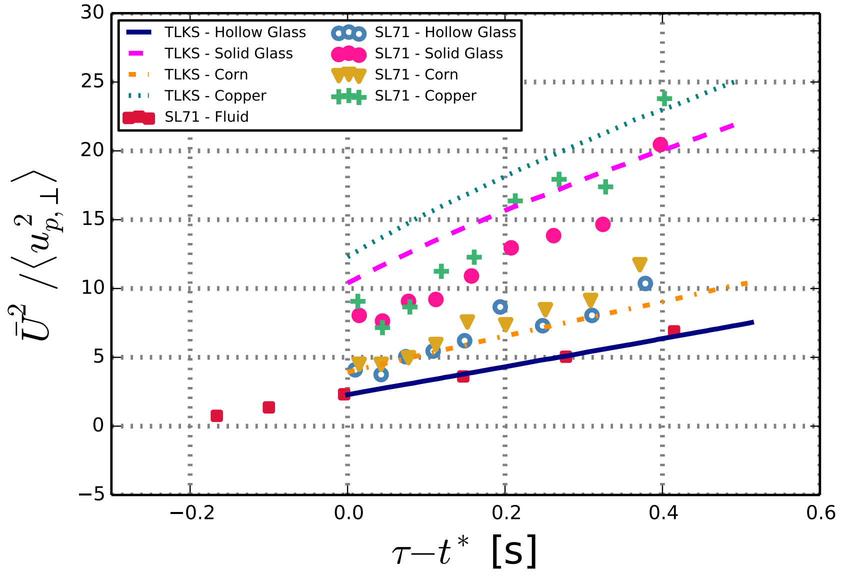

Figure 5.13: Non-dimensional reciprocal of mean-squared lateral particle velocity ($\bar{U}^2/\langle u_{p,\perp}^2\rangle$) for fluid tracers and inertial particles in TLKS-generated fields, compared with the experimental results of SL71. t^* corresponds to "station one" in the experimental results (the position at which particle statistics are first measured).

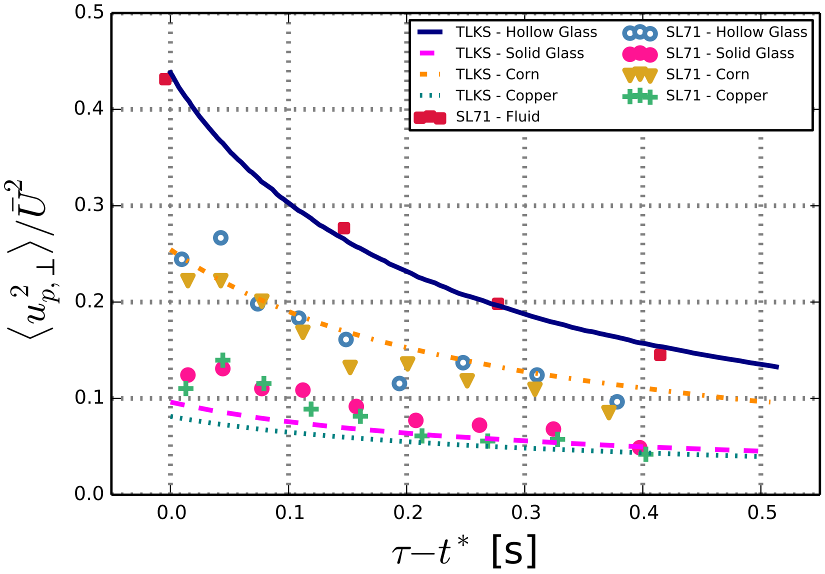

Figure 5.14: Non-dimensional mean-squared lateral particle velocity ($\langle u_{p,\perp}^2 \rangle / \bar{U}^2$) for fluid tracers and inertial particles in TLKS-generated fields, compared with the experimental results of SL71.

whose resulting turbulent-like field enforces T_L. If the objective were solely to formulate a method that enforces T_L, then the added expense of KS (relative to SSF) would not be justified. But it is demonstrated here that its utility extends to restoring the expected behaviour of *inertial particles* as well - namely the crossing trajectories and the continuity effects. This occurs without appeal to further empiricisms, as is the case for SSF approaches. It is also shown here that TLKS can effectively capture Lagrangian statistics, even if the flow is decaying.

Chapter 6

Summary and Recommendations

6.1 Summary of accomplishments

Particle-laden flow modelling can be applied to a wide range of real-world scenarios, and as such, computationally tractable simulation techniques are highly desired. A widely-applied technique is stochastic separated flow (SSF), which, very loosely speaking, models individual particles as random walks. The chief drawback of such models is their blindness to turbulence *structure*, in a variety of important senses. In parallel, there exists much literature devoted to exploring various properties of turbulent-like fields generated via kinematic simulation (KS), though this literature is primarily of theoretical interest, and there has lacked a comprehensive exploration of its applicability to reproducing turbulence *structure* as it is manifested in a variety of statistics of fundamental importance to modellers. Such an exploration was carried out here, and good qualitative agreement was obtained with a benchmark direct numerical simulation (DNS). It is noted that KS is foremost a *stochastic Lagrangian particle model*, therefore, the Lagrangian properties of KS "turbulence" must be at the foundation of any investigation into its utility as a modelling technique. Accordingly, a method was devised and tested in which a target Lagrangian integral timescale was enforced. This novel method casts an impression of structure on the particle ensemble in a manner that SSF models cannot easily achieve. The following is a more detailed summary:

- Various shortcomings of stochastic separated flow (SSF) applications to particle-laden flow modelling were identified, and KS was proposed as an alternative (Sec. 2.2.3 and 2.2.4).

- If preferential concentration is of interest for a particle-laden KS, there exist a variety of subtle yet important considerations for ensuring confidence in single-particle Lagrangian statistics and correlation dimension, while remaining true to the classical KS formulation. Such issues have not been addressed in the literature. A method for carrying out an ensemble of particle-laden KS realizations on an *extended domain* was motivated, and was shown to grant confidence in the statistics of interest (Sec. 3.3 and App. C).

- Various second-order statistics of turbulent-like KS fields were derived analytically (App. B).

- KS was tested against a DNS benchmark for fluid tracers, and the most favourable comparison between the Lagrangian statistics occurred when the turbulent-like field was steady ($\omega_n = 0$ for all n, in equation 2.13) (e.g. Fig. 4.2).

- KS was tested against a DNS benchmark for inertial particles for a range of St, with and without gravity. Without gravity, the most favourable comparison between DNS and KS occurred for high St (see Fig. 4.12 for long-range dispersion and Fig. 4.16 for correlation dimension). For the correlation dimension of $St \sim 1$ inertial particles (where St is the particle Stokes number), the most favourable comparison occurred for a steady flow (Fig. 4.13).

- Steady KS qualitatively reproduces the elevated dispersion of inertial particles in the absence of gravity (Fig. 4.11), in accordance with the DNS results, and in accordance with results elsewhere in the literature.

- In the presence of a sufficiently strong body force, the continuity effect is reproduced; that is, the lateral dispersion of inertial particles is reduced compared with the longitudinal dispersion (Fig. 4.17).

- Also in the presence of a body force, a generally favourable comparison between asymptotic correlation dimension is observed between DNS and KS for all St, but especially for $St > 1$ (Fig. 4.18). The improved performance is explained by the domination of Lagrangian properties by the Eulerian properties, by Taylor's frozen turbulence hypothesis (Fig. 4.21).

- A simple method for applying KS in a manner that enforces the target Lagrangian integral timescale was motivated (and was termed Target Lagrangian integral timescale Kinematic Simulation, or TLKS), and was tested against an experimental benchmark (the experimental results of Snyder & Lumley (1971)). Excellent agreement of dispersion was obtained; the crossing trajectories (Fig. 5.10) and continuity effects (Fig. 5.11) were reproduced.

6.2 Lack of sweeping?

Throughout the KS literature, shortcomings of KS have been identified in a variety of scenarios (according to varying expectations of what the model *should* achieve). Such shortcomings are often ascribed to the lack of dynamic sweeping of small scales by the large. This is reminiscent of the discussion in Sec. 2.2.3, in which the deficiencies of SSF models are attributed to their lack of consideration of *structure*. Turbulence results from the evolution of nonlinear dynamic equations, and as such, it is not clear how the concepts of *turbulence* and *sweeping* can be divorced. Consequently it is not immediately clear in what sense a given feature of Lagrangian statistics could be an *effect* of sweeping, since sweeping is inherent in turbulence.

This underlines a key danger in KS model development. Classical turbulence theory is based on heuristic arguments involving the properties of a hierarchy of "eddies", and such arguments have yielded conclusions that have been extensively verified by numerical and experimental evidence. Of course there do not exist isolated eddies in real turbulence, but nonetheless these heuristics *work*. KS formulations often appeal to these same heuristic arguments, and transpose the properties of "elements" of a cascade (eddies) onto the elements of KS (the individual terms in the generation of a turbulent-like field - see Eq. (2.13)). Naturally such an approach is predicated on the assumption that the "elements" of turbulence, in some sense, work in concert in the same manner in either real turbulence or KS, and of course they do not. For example, the unsteadiness formulation (Eq. (2.34)) is "based on an approximation of small-scale sweeping" (Osborne *et al.* (2005)). While bearing intuitive appeal in the Eulerian perspective, it is emphasized that the Lagrangian properties cannot be easily surmised from the properties of the individual elements of the turbulent-like field, even if they are sensible in the Eulerian perspective. In Osborne *et al.* (2005), it is shown that the "sweeping" heuristic succeeds in restoring a certain qualitative agreement with the expected Lagrangian frequency spectrum and autocorrelation, and this is seen as a certain validation of this heuristic. The danger in all this is that it could grant legitimacy to models that are deemed successful according to properties of secondary relevance.

The main consequence for this investigation is as follows: on the path to a widely-applicable KS model, there exist many red herrings. Once again, the relationship between Eulerian and Lagrangian properties in KS is opaque, therefore properties of a given KS formulation - that correspond to a certain intuitive idea of "realism" - are not necessarily manifested in the Lagrangian properties. The converse is also true; it is possible to reproduce the desired Lagrangian statistics, while violating one's expectations of how a turbulent-like field *should* behave in the Eulerian perspective. Indeed this was eminently demonstrated in Ch. 5; a successful model was constructed with *steady* KS fields (advected by a mean flow), and of course real turbulence is not steady. Indeed the only meaningful definition of success for a stochastic Lagrangian particle model (such as KS) is whether or not it reproduces the desired Lagrangian properties of a particle ensemble.

Is there a more meaningful sense in which the sweeping of small eddies by the large can be simulated in KS? Yes, if "large eddy" is interpreted as mean flow, as was done in Sec. 5.2.2. Fung *et al.* (1992) considered the question of whether this technique of deforming coordinate systems can be extended to simulate the interaction amongst the hierarchy of eddies. They proposed a somewhat more general version of (5.17):

$$\mathbf{u}_s(\mathbf{x},t) = \sum_{n=1}^{N_\kappa} \mathbf{a}_n \cos(\boldsymbol{\kappa}_n \cdot \mathbf{X} + \omega_n t) + \mathbf{b}_n \sin(\boldsymbol{\kappa}_n \cdot \mathbf{X} + \omega_n t) \tag{6.1}$$

where $\mathbf{X}$ is given by:

$$\mathbf{X}(t) = \mathbf{x}_0 + \int_0^t \mathbf{u}_l(\mathbf{x}(\tau),\tau)\, d\tau \tag{6.2}$$

Here, $\mathbf{u}_l$ does not necessarily correspond to a mean flow, but to an appropriately defined “large-scale motion”, perhaps given by large-eddy simulation.

Unfortunately, if $\mathbf{u}_l$ is anything more complicated than a homogenous mean flow - even if it contains a simple mean shear - the *continuity* of the overall velocity field is not preserved. While deforming coordinate systems can, in a sense, incorporate true sweeping motion, the fundamental problem remains; there is a lack of “communication” between the modes. In (6.1) and (6.2), the superposition of the small and large motions can yield small-scale gradients that, in real turbulence, would not be tolerated by viscosity. Indeed this shortcoming was recognized in Fung *et al.* (1992), and it appears their KS formulation has not been explored since.

6.3 Suggestions for future research

With respect to the TLKS method proposed and tested in Ch. 5, there exist a variety of promising avenues for the further development of this tool, namely:

- The clear scale relations observed in S^L and R^L for high-$\tilde{\kappa}_N/\tilde{\kappa}_1$ KS (in Sec. 5.1.2) hint at the possibility of deriving Lagrangian properties from an input Eulerian field (perhaps only for an infinitely wide inertial range).

- The method was constructed such that an input k (or u_{rms}) corresponds to a unique $\tilde{\kappa}_1$ (for recovering a desired T_L), and $\tilde{\kappa}_N$ was assumed to be effectively infinite. It was also observed that T_L depends on $\tilde{\kappa}_1$ and $\tilde{\kappa}_N$ (Figs. 5.6 and 5.7), which suggests the existence of a set of $(\tilde{\kappa}_1, \tilde{\kappa}_N)$ coordinates that can recover a target T_L (corresponding to a given k and ϵ). Let such a set be called $S_{k,\epsilon}$. While all members of $S_{k,\epsilon}$ restore T_L (by definition), some members may be better than others at restoring additional statistics of interest, for instance, Lagrangian flatness, or correlation dimension for inertial particles.

  Furthermore, one may assume the canonical input spectrum to be characterized by additional parameters. For instance, the value of p in $E(\kappa) = c\kappa^{-p}$ may not necessarily be 5/3 because, again, the primary goal is not to generate a field that is realistic from the Eulerian perspective. Indeed, there exists a precedent for the manipulation of p, with the goal of restoring reasonable Lagrangian behaviour (Khan & Vassilicos (2003)).

  Additionally the unsteadiness parameter, λ, (under either Type A or Type B KS) could be reintroduced. While the results in Ch. 4 show that high unsteadiness yields highly unrealistic Lagrangian properties, it should be emphasized that this corresponds to certain assumed Eulerian second-order statistics. Since the spectrum employed in TLKS does not enforce this Eulerian realism, the reintroduction of unsteadiness may enhance predictions in the same manner that the reintroduction of $\tilde{\kappa}_N$ might; increasing the dimension of parameter space offers the possibility of improving predictions of a greater variety of statistics of interest.

Notwithstanding these issues, the work presented here demonstrates that KS is applicable to simulating the full spectrum of motions that underlie particle behaviour. Such a modelling technique has been shown to broadly restore features of a particle ensemble that are fundamentally important for modellers, in a manner that SSF models are unable to comprehensively achieve.

Appendix A

DNS Verification

Unless otherwise stated, all time variables were non-dimensionalized by the large eddy turnover time, τ_{eddy}, defined as:

$$\tau_{eddy} = \frac{L_E}{u_{rms}} \tag{A.1}$$

where L_E is the longitudinal Eulerian length scale, defined as:

$$L_E = \frac{1}{3}(L_{11} + L_{22} + L_{33}) \tag{A.2}$$

where:

$$L_{11} = \int_0^{L/2} R_{11}^E(\mathbf{x} + \mathbf{e}_1 r)\, dr \tag{A.3}$$

and similarly for L_{22} and L_{33}. $R_{ii}^E(\mathbf{r})$, the Eulerian velocity autocorrelation, is defined in Sec. B.3.

To test for timestep independence, two decaying DNS were carried out with the same initial condition, but one with timestep $\Delta t = 0.0005$, and the other with

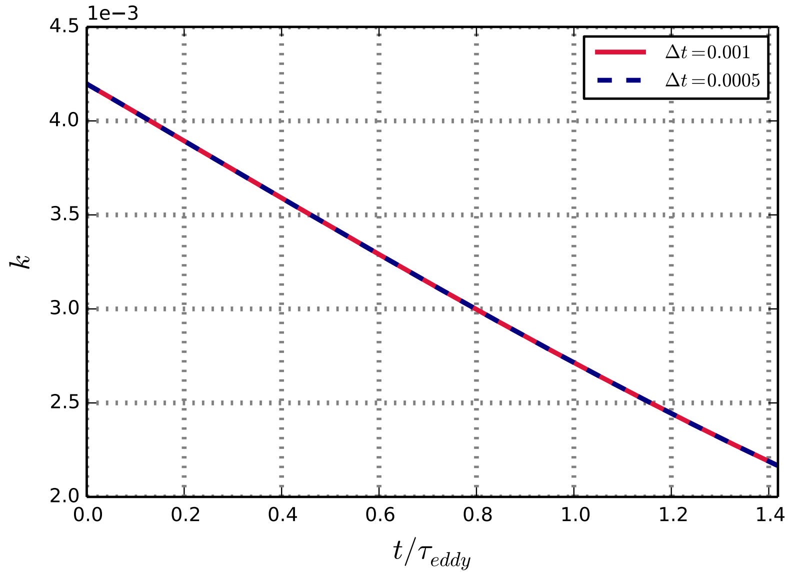

Figure A.1: Turbulent kinetic energy, k, for decaying DNS, for $\Delta t = 0.001$ and $\Delta t = 0.0005$.

timestep $\Delta t = 0.001$. The history of energy is compared between the two simulations, and is shown in Fig. A.1 - the two histories are coincident, indicating that $\Delta t = 0.001$ is suitable. It is noted that the large eddy turnover time (τ_{eddy}) does not remain fixed in a decaying DNS; here it was calculated for the initial field. Regardless of what constant τ_{eddy} assumes, the result is unaffected.

In order to generate flows in which the statistics are approximately stationary, it is necessary to inject energy on the large scales, to compensate for the energy dissipation at the small scales. Initially the method of Eswaran & Pope (1988) was considered, however the statistically stationary properties of the field are difficult to predict for a given set of forcing parameters. In forced DNS literature, the simple method of Chen *et al.* (1993) has become increasingly favoured, and it is the method applied here. This method operates by keeping the energy constant at large scales.

The energy contained within a band around κ_n in wavenumber space in given by:

$$E_n = \frac{1}{2} \sum_{\kappa_n \leq |\boldsymbol{K}| < \kappa_n + 1} \left\langle \hat{\mathbf{u}}_{\boldsymbol{K}}(t) \cdot \hat{\mathbf{u}}^*_{\boldsymbol{K}}(t) \right\rangle \tag{A.4}$$

where κ_n is a sequence of wavenumbers, given as $\kappa_n = 2\pi n$. For the simulations here, E_2 and E_3 were held fixed at each timestep, and were chosen such that $E_3/E_2 = (3/2)^{-5/3}$ (that is, the Kolmogorov scaling of the energy spectrum in this segment of wavenumber space was enforced). Contrary to its common application in the literature, E_1 was not held fixed, since it was found that excessive energy at the smallest wavenumber band increased the large-scale anisotropy (defined in (A.5)) to unacceptable levels.

Further results of the forced DNS (as carried out in Ch. 4) are presented here, and are compared to DNS results in the literature.

- A necessary condition to ensure numerical stability is that the Courant number, C, should remain under unity (Eswaran & Pope (1988)): indeed it was observed here that $C < 0.15$ throughout (Fig. A.2).
- As was noted in Sec. 3.1, it was ensured that $\eta\kappa_{\max} \geq 1$ throughout the simulation, which ensures sufficient spatial resolution of all length scales of the flow (Yeung & Pope (1988); Eswaran & Pope (1988)) (Fig. A.3).
- The large-scale anisotropy tensor B_{ij} is defined as:

$$B_{ij} = \frac{\langle u_i u_j \rangle}{2k} - \frac{1}{3}\delta_{ij} = \frac{\langle u_i u_j \rangle}{\langle u_k u_k \rangle} - \frac{1}{3}\delta_{ij} \tag{A.5}$$

The largest absolute value of any of the components was about 0.08 (See Fig.

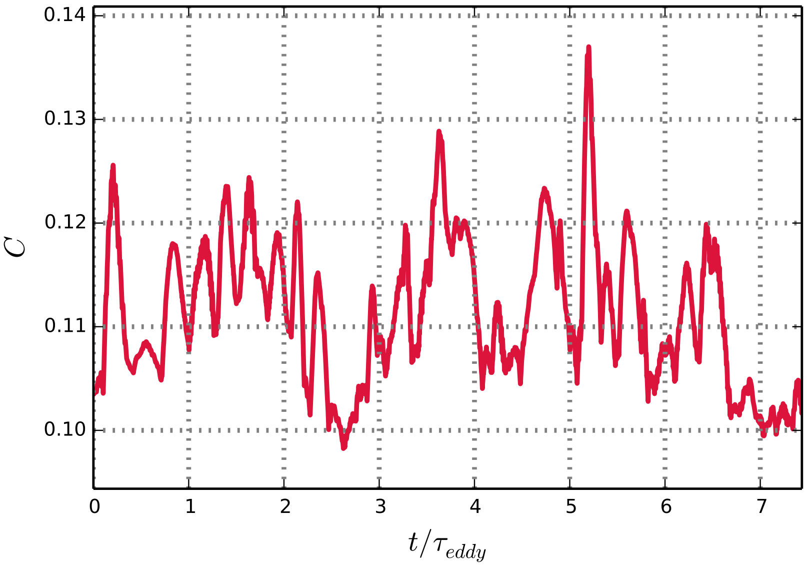

Figure A.2: History of the Courant number, C.

A.4) - this relatively high anisotropy is explained by the forcing method, in which the largest scales of motion (which bear the greatest contribution to the anisotropy) are continually amplified to maintain an approximately constant energy. This highlights the importance of considering, whenever possible, the Lagrangian statistics averaged over all components (see Sec. 2.2.5).

- The skewness of the velocity field (γ_u) is a measure of the nonlinear energy transfer from large to small scales. It is calculated as:

$$S_u = -\frac{\sum_{i=1}^{3} \langle (\frac{\partial u_i}{\partial x_i})^3 \rangle}{[\sum_{i=1}^{3} \langle (\frac{\partial u_i}{\partial x_i})^2 \rangle]^{3/2}} \tag{A.6}$$

Throughout the simulation here, γ_u was roughly 0.5, in line with the DNS results of Elghobashi & Trusedell (1992) and Cernick (2013) (see Fig. A.5).

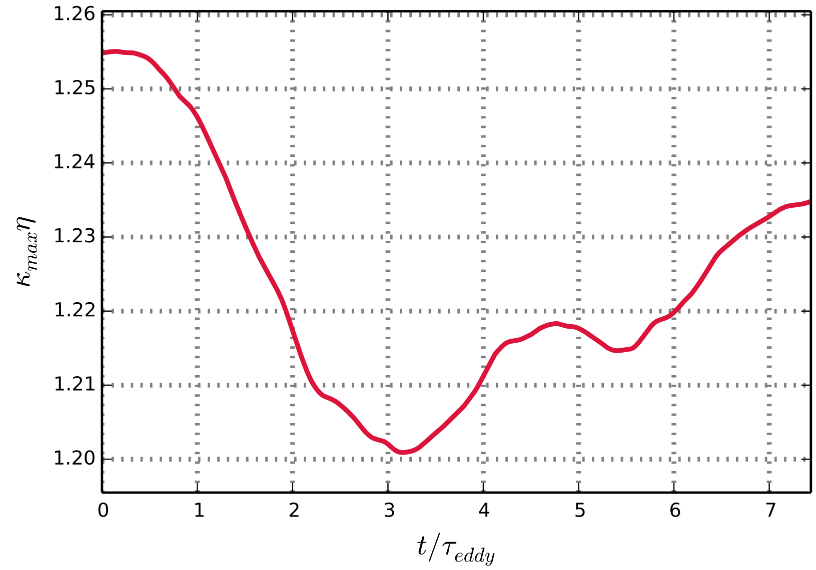

Figure A.3: History of $\eta\kappa_{\max}$, where η is the Kolmogorov microscale, and $\kappa_{\max}$ is the largest resolved wavenumber.

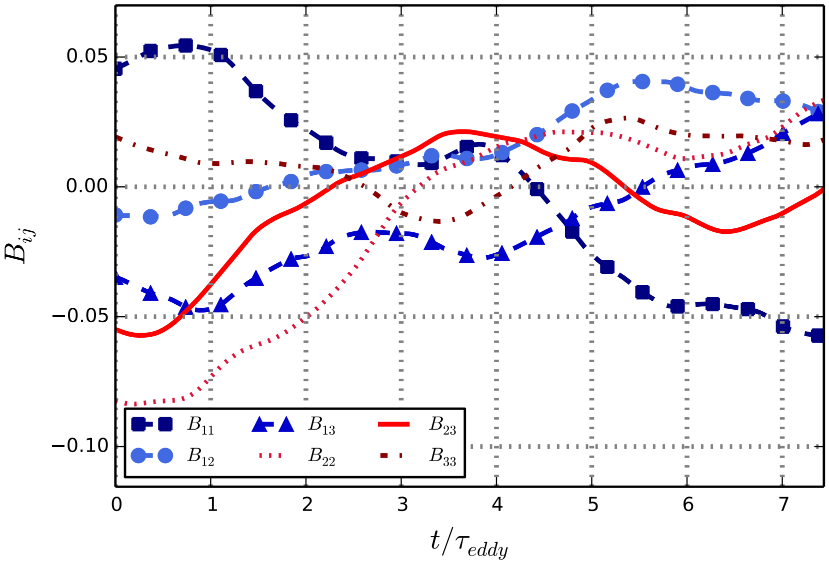

Figure A.4: History of components of the large-scale anisotropy tensor, B_{ij}.

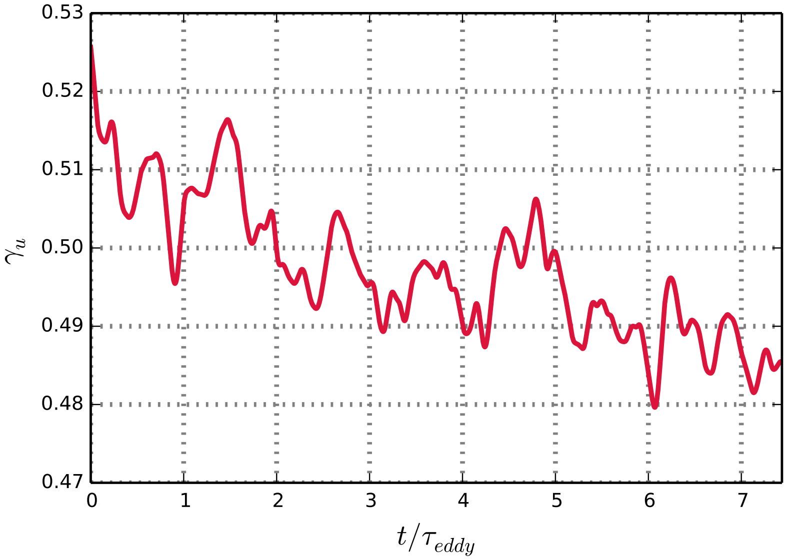

Figure A.5: History of the skewness of the velocity derivatives, γ_u.

Appendix B

Eulerian Second-Order Statistics in KS

B.1 Alternative KS formulations

In the KS literature, there exist many shades of KS formulations. One widely applied alternative is (as in Kraichnan (1970); Malik & Vassilicos (1999); Malik (2014)):

$$\mathbf{u}_f(\mathbf{x}, t) = \sum_{n=1}^{N_\kappa} \mathbf{a}_n \times \hat{\boldsymbol{\kappa}}_n \cos(\boldsymbol{\kappa}_n \cdot \mathbf{x} + \omega_n t) + \mathbf{b}_n \times \hat{\boldsymbol{\kappa}}_n \sin(\boldsymbol{\kappa}_n \cdot \mathbf{x} + \omega_n t) \tag{B.1}$$

where $\hat{\boldsymbol{\kappa}}_n$ is the unit vector given by $\hat{\boldsymbol{\kappa}}_n = \boldsymbol{\kappa}_n / \kappa_n$. Here, the cross product ensures incompressibility. For such a KS formulation, the magnitudes of $\mathbf{a}_n$ and $\mathbf{b}_n$ can be sampled from a distribution, such that over a very large ensemble of realizations, the spectrum is (on average) enforced. In order to obtain meaningful data on preferential concentration, a *single* realization must contain many particles, since many particles must "see" the same turbulent-like structures. A large number of particles per realization - combined with a very large number of realizations required to ensure confidence in energy - would likely be computationally intractable. Therefore, in the KS formulation in this study, $\mathbf{a}_n$ and $\mathbf{b}_n$ were chosen with fixed magnitudes, such that the energy density was enforced *exactly* for every KS realization (following Thomson & Devenish (2005) and Nicolleau & Abou El-Azm Aly (2012)).

B.2 Energy

It is now shown that the KS formulation in Sec. 2.2.4 gives the appropriate amplitude of each KS mode, such that the appropriate energy density at each wavenumber is enforced, for even a single realization. The energy is evaluated from (2.13) as:

$$\left\langle \frac{1}{2}|\mathbf{u}(\mathbf{x},t)|^2 \right\rangle = \left[\frac{1}{2|V|} \int_V \Big| \sum_{n=1}^{N_\kappa} \mathbf{a}_n \cos(\boldsymbol{\kappa}_n \cdot \mathbf{x}) + \mathbf{b}_n \sin(\boldsymbol{\kappa}_n \cdot \mathbf{x}) \Big|^2 \, dV \right] \tag{B.2}$$

where the [ ] parentheses indicate the average over an ensemble of realizations, and V is $\mathbf{R}^3$, or, all of three-dimensional space. Admittedly the use of $\frac{1}{|V|}$ is an abuse of notation, but it is implied that the integrals would be evaluated improperly. Also without loss of generality, t has been set to 0. First, consider the inner product:

$$\begin{aligned} \int_V \Big| \sum_{n=1}^{N_\kappa} \mathbf{a}_n \cos(\boldsymbol{\kappa}_n \cdot \mathbf{x}) \Big|^2 \, dV &= \int_V \sum_{m=1}^{N_\kappa} \mathbf{a}_m \cos(\boldsymbol{\kappa}_m \cdot \mathbf{x}) \cdot \sum_{n=1}^{N_\kappa} \mathbf{a}_n \cos(\boldsymbol{\kappa}_n \cdot \mathbf{x}) \, dV \\ &= \int_V \sum_{m=1}^{N_\kappa} \sum_{n=1}^{N_\kappa} (\mathbf{a}_m \cdot \mathbf{a}_n) \cos(\boldsymbol{\kappa}_m \cdot \mathbf{x}) \cos(\boldsymbol{\kappa}_n \cdot \mathbf{x}) \, dV \end{aligned} \tag{B.3}$$

Now the integral of the product of sines (or cosines) of different periods over an infinite domain is zero, hence the previous expression vanishes for $m \neq n$. Therefore:

$$\int_V \Big| \sum_{n=1}^{N_\kappa} \mathbf{a}_n \cos(\boldsymbol{\kappa}_n \cdot \mathbf{x}) \Big|^2 \, dV = \int_V \sum_{n=1}^{N_\kappa} |\mathbf{a}_n|^2 (\cos(\boldsymbol{\kappa}_n \cdot \mathbf{x}))^2 \, dV \tag{B.4}$$

and similarly for the product of sines. Therefore:

$$\begin{aligned}
\left\langle \frac{1}{2} |\mathbf{u}(\mathbf{x},t)|^2 \right\rangle &= \left[\frac{1}{2|V|} \int_V \sum_{n=1}^{N_\kappa} |\mathbf{a}_n|^2 (\cos(\boldsymbol{\kappa}_n \cdot \mathbf{x}))^2 + |\mathbf{b}_n|^2 (\sin(\boldsymbol{\kappa}_n \cdot \mathbf{x}))^2 \, dV \right] \\
&= \left[\sum_{n=1}^{N_\kappa} |\mathbf{a}_n|^2 \frac{1}{2|V|} \int_V (\cos(\boldsymbol{\kappa}_n \cdot \mathbf{x}))^2 \, dV + |\mathbf{b}_n|^2 \frac{1}{2|V|} \int_V (\sin(\boldsymbol{\kappa}_n \cdot \mathbf{x}))^2 \, dV \right] \\
&= \left[\sum_{n=1}^{N_\kappa} |\mathbf{a}_n|^2 \Big(\frac{1}{4}\Big) + |\mathbf{b}_n|^2 \Big(\frac{1}{4}\Big) \right]
\end{aligned} \tag{B.5}$$

and since $\mathbf{a}_n$ and $\mathbf{b}_n$ have the same magnitude in every realization (it is only their orientations that are random), one obtains:

$$\left\langle \frac{1}{2} |\mathbf{u}(\mathbf{x},t)|^2 \right\rangle = \frac{1}{4} \sum_{n=1}^{N_\kappa} |\mathbf{a}_n|^2 + |\mathbf{b}_n|^2 \tag{B.6}$$

Also:

$$\left\langle \frac{1}{2} |\mathbf{u}(\mathbf{x},t)|^2 \right\rangle = k = \sum_{n=1}^{N_\kappa} E(\kappa) \Delta\kappa_n \tag{B.7}$$

Equations (B.6) and (B.7) together yield:

$$\sum_{n=1}^{N_\kappa} E(\kappa) \Delta\kappa_n = \frac{1}{4} \sum_{n=1}^{N_\kappa} |\mathbf{a}_n|^2 + |\mathbf{b}_n|^2 \tag{B.8}$$

and if $|\mathbf{a}_n|^2 = |\mathbf{b}_n|^2 = 2E(\kappa)\Delta\kappa_n$, the above equation is satisfied.

B.3 Eulerian autocorrelations

The Eulerian two-point (or two-time) velocity autocorrelation tensor has the general form:

$$R_{ij}^E(\mathbf{r},\tau) = \frac{\langle u_{f,i}(\mathbf{x},t)u_{f,j}(\mathbf{x}+\mathbf{r},t+\tau)\rangle}{\sqrt{\langle u_{f,i}(\mathbf{x},t)^2\rangle}\sqrt{\langle u_{f,j}(\mathbf{x}+\mathbf{r},t+\tau)^2\rangle}} \tag{B.9}$$

Consider the one-point, two-time autocorrelation $R_{ii}^E(\tau)$:

$$R_{ii}^E(\tau) = \frac{[\frac{1}{|V|}\int_V u_{f,i}(t)u_{f,i}(t+\tau)\,dV]}{\sqrt{[\frac{1}{|V|}\int_V u_{f,i}(t)^2\,dV]}\sqrt{[\frac{1}{|V|}\int_V u_{f,i}(t+\tau)^2\,dV]}} \tag{B.10}$$

For stationary, isotropic turbulence, $[\int_V u_{f,i}(t)^2\,dV] = [\int_V u_{f,i}(t+\tau)^2\,dV] = u_{rms}^2$, where $\frac{3}{2}u_{rms}^2 = k$. The numerator of B.10 thus becomes:

$$\begin{aligned}
&\Big[\frac{1}{|V|}\int_V u_{f,i}(t)u_{f,i}(t+\tau)\,dV\Big] \qquad\qquad \text{(B.11)}\\
&= \Big[\frac{1}{|V|}\int_V \sum_{m=1}^{N_\kappa}(a_{m,i}\cos(\boldsymbol{\kappa}_m\cdot\mathbf{x}+\omega_m t) + b_{m,i}\sin(\boldsymbol{\kappa}_m\cdot\mathbf{x}+\omega_m t)\\
&\times\sum_{n=1}^{N_\kappa}(a_{n,i}\cos(\boldsymbol{\kappa}_n\cdot\mathbf{x}+\omega_n(t+\tau)) + b_{n,i}\sin(\boldsymbol{\kappa}_n\cdot\mathbf{x}+\omega_n(t+\tau))dV\Big]
\end{aligned}$$

If $m \neq n$, then

$$\frac{1}{|V|}\int_V a_{m,i}\cos(\boldsymbol{\kappa}_m\cdot\mathbf{x}+\omega_m t)a_{n,i}\cos(\boldsymbol{\kappa}_n\cdot\mathbf{x}+\omega_n(t+\tau))\,dV = 0 \tag{B.12}$$

and similarly for the terms involving the products of cosine and sine, sine and cosine, and sine and sine. If $m = n$, and if the volume integral is, without loss of generality, evaluated first over the first spatial component, then:

$$\begin{aligned}
&\frac{1}{|V|}\int_V a_{m,i}\cos(\boldsymbol{\kappa}_m\cdot\mathbf{x}+\omega_m t)a_{n,i}\cos(\boldsymbol{\kappa}_n\cdot\mathbf{x}+\omega_n(t+\tau))\,dV \\
&=\lim_{p\to\infty}\frac{a_{n,i}^2}{2p}\Big[\frac{\sin(\omega_n(\tau+2t)+2(\boldsymbol{\kappa}_n\cdot\mathbf{x}))+2\kappa_{n,1}p\cos(\omega_n\tau)}{4\kappa_{n,1}}\Big|_{-p}^{p} \\
&=\frac{2a_{n,i}^2\omega_n\cos(\omega_n\tau)}{4\omega_n} \\
&=a_{n,i}^2\frac{\cos(\omega_n\tau)}{2}
\end{aligned} \tag{B.13}$$

and similarly for the product of sine and sine. For the product of sine and cosine (or vice versa), the integral vanishes. Therefore:

$$\frac{1}{|V|}\int_V u_{f,i}(t)u_{f,i}(t+\tau)\,dV=\sum_{n=1}^{N_\kappa}(a_{n,i}^2+b_{n,i}^2)\frac{\cos(\omega_n\tau)}{2} \tag{B.14}$$

Now over an ensemble of realizations,

$$[a_{n,1}^2]=[a_{n,2}^2]=[a_{n,3}^2]=\frac{1}{3}|\mathbf{a}_n|^2=\frac{2}{3}E(\kappa_n)\Delta\kappa_n \tag{B.15}$$

and similarly for $b_{n,i}$ (and $\mathbf{b_n}$). So:

$$\Big[\frac{1}{|V|}\int_V u_{f,i}(t)u_{f,i}(t+\tau)\,dV\Big]=\frac{2}{3}\sum_{n=1}^{N_\kappa}E(\kappa_n)\Delta\kappa_n\cos(\omega\tau) \tag{B.16}$$

and finally, the general expression of a diagonal component of this tensor is:

$$R_{ii}^E(\tau)=\frac{2}{3u_{rms}^2}\sum_{n=1}^{N_\kappa}E(\kappa_n)\Delta\kappa_n\cos(\omega_n\tau) \tag{B.17}$$

Similarly to how it is defined for Lagrangian statistics, the *second-order, one-point, two-time Eulerian structure function tensor*, $S_{ij}^E(\tau)$, is defined as:

$$S_{ij}^E(\tau) = \langle (u_i(\mathbf{x}, t) - u_j(\mathbf{x}, t + \tau))^2 \rangle \tag{B.18}$$

and for homogenous, isotropic turbulence, this quantity exhibits the following straightforward relationship to the autocorrelation:

$$S_{ij}^E(\tau) = 2\langle u_i^2 \rangle (1 - R_{ij}^E(\tau)) \tag{B.19}$$

The diagonal components, $S_{ii}^E(\tau)$, were compared to that of the *corresponding* DNS. In line with a similar analysis of Osborne *et al.* (2005), $S^E(\tau) \sim \tau^2$ is obtained in the ballistic range, and $S^E(\tau) \sim \tau^{2/3}$ in the inertial range for Type B KS, which more closely resembles the scalings in DNS than Type A KS (and which corresponds to the expected Eulerian frequency spectrum scaling $\Phi^E(\omega) \sim \omega^{-5/3}$ (Tennekes (1975); Osborne *et al.* (2005))). Despite the close match of the slopes of the curves between DNS and Type B KS, the KS values are shifted upward compared with the DNS, indicating that the field becomes decorrelated more quickly at a fixed position (Fig. B.1).

Now consider the case of the *two-point, one-time Eulerian velocity autocorrelation* for homogeneous turbulence:

$$R_{ii}^E(\mathbf{r}) = \frac{\langle u_{f,i}(\mathbf{x}) u_{f,i}(\mathbf{x} + \mathbf{r}) \rangle}{\langle (u_{f,i}(\mathbf{x}))^2 \rangle} \tag{B.20}$$

When $\mathbf{r}$ is constrained to be parallel to the i-th direction, this is the *longitudinal*

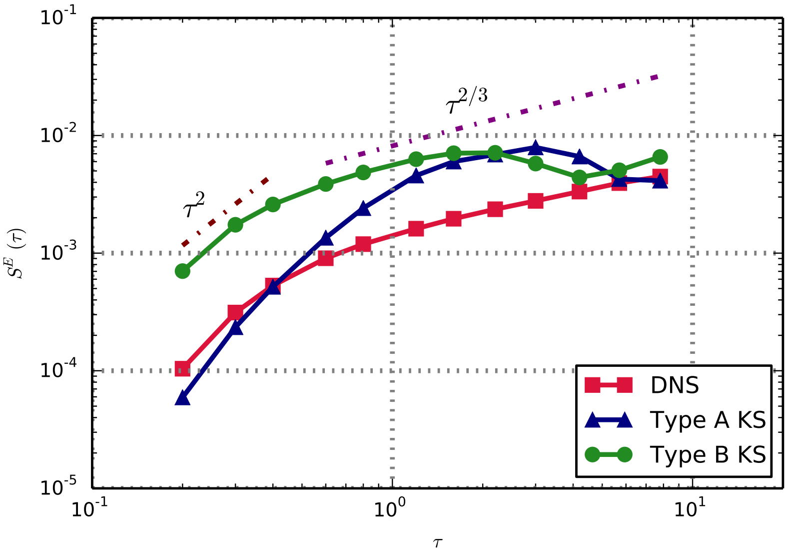

Figure B.1: Eulerian one-point, two-time velocity structure function for DNS, and the corresponding Types A and B KS. For both KS, $\lambda = 0.5$

autocorrelation (and, following Batchelor (1953), will be denoted $f(r)$ for isotropic turbulence). When $\mathbf{r}$ is constrained to be *perpendicular* to the i-th direction, it gives the *lateral* autocorrelation (similarly denoted as $g(r)$).

The numerator of $f(r)$ can be evaluated, using a similar technique as for the one-point two-time autocorrelation:

$$\left[\frac{1}{|V|}\int_V u_{f,i}(\mathbf{x})u_{f,i}(\mathbf{x}+r\mathbf{e}_i)\,dV\right] = \left[\sum_{n=1}^{N_\kappa}(a_{n,i}^2+b_{n,i}^2)\frac{\cos(\kappa_{n,i}r)}{2}\right]$$

And similarly the numerator for the lateral autocorrelation is derived as:

$$\left[\frac{1}{|V|}\int_V u_{f,i}(\mathbf{x})u_{f,i}(\mathbf{x}+r\mathbf{e}_j)\,dV\right] = \left[\sum_{n=1}^{N_\kappa}(a_{n,i}^2+b_{n,i}^2)\frac{\cos(\kappa_{n,j}r)}{2}\right]$$

where $i \neq j$. The longitudinal and lateral autocorrelations were evaluated numerically

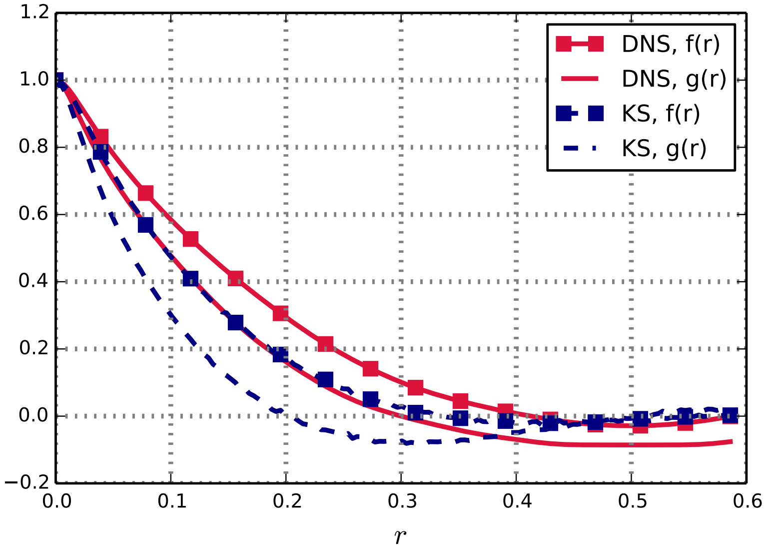

Figure B.2: One-dimensional longitudinal ($f(r)$) and lateral ($g(r)$) autocorrelations, in both DNS and KS.

for 300 realizations, with an input spectrum obtained from the DNS. Consistent with the observations of Osborne *et al.* (2005), the same qualitative behaviour is observed between DNS and KS; in particular, there exists a significant negative loop in the lateral autocorrelation - see Fig. B.2.

When the argument of the Eulerian autocorrelation is given with a scalar displacement r, the autocorrelation is interpreted as follows:

$$R^E_{ii}(r) = \int_{|\mathbf{r}|=r} \frac{\langle u_{f,i}(\mathbf{x}) u_{f,i}(\mathbf{x}+\mathbf{r})\rangle}{\langle (u_{f,i}(\mathbf{x}))^2\rangle} \tag{B.21}$$

This quantity admits the analytical description (Batchelor (1953); Malik (1991)):

$$R^E_{ii}(r) = \int_0^\infty E(\kappa)\frac{\sin(\kappa r)}{\kappa r}\, d\kappa \tag{B.22}$$

This quantity may hold clues regarding an *a priori* description of Lagrangian statistics in KS (see Sec. 5.1.2).

B.4 Large-scale anisotropy

The large-scale anisotropy of a field is given in equation (A.5). Applying the definition of KS, the correlation term is given as:

$$\langle u_{f,i}(\mathbf{x})u_{f,j}(\mathbf{x})\rangle = \Big\langle \Big(\sum_{m=1}^{N_\kappa} a_{m,i}\cos(\boldsymbol{\kappa}_m\cdot\mathbf{x}) + b_{m,i}\sin(\boldsymbol{\kappa}_m\cdot\mathbf{x})\Big)\Big(\sum_{n=1}^{N_\kappa} a_{n,j}\cos(\boldsymbol{\kappa}_n\cdot\mathbf{x}) + b_{n,j}\sin(\boldsymbol{\kappa}_n\cdot\mathbf{x})\Big)\Big\rangle \tag{B.23}$$

Once again, since correlations between $m \neq n$ terms vanish, one obtains:

$$\begin{aligned}\langle u_{f,i}(\mathbf{x})u_{f,j}(\mathbf{x})\rangle = \sum_{n=1}^{N_\kappa} & \Big\langle a_{n,i}\cos(\boldsymbol{\kappa}_n\cdot\mathbf{x})a_{n,j}\cos(\boldsymbol{\kappa}_n\cdot\mathbf{x})\Big\rangle \\ & + \Big\langle a_{n,i}\cos(\boldsymbol{\kappa}_n\cdot\mathbf{x})b_{n,j}\sin(\boldsymbol{\kappa}_n\cdot\mathbf{x})\Big\rangle \\ & + \Big\langle b_{n,i}\sin(\boldsymbol{\kappa}_n\cdot\mathbf{x})a_{n,j}\cos(\boldsymbol{\kappa}_n\cdot\mathbf{x})\Big\rangle \\ & + \Big\langle b_{n,i}\sin(\boldsymbol{\kappa}_n\cdot\mathbf{x})b_{n,j}\sin(\boldsymbol{\kappa}_n\cdot\mathbf{x})\Big\rangle \end{aligned} \tag{B.24}$$

Employing the observation directly after (B.13), only the correlations of cosine times cosine (and sine times sine) terms are preserved, yielding the following expression for large-scale anisotropy:

$$B_{ij} = \frac{1}{4k}\sum_{n=1}^{N_\kappa}[a_{n,i}a_{n,j} + b_{n,i}b_{n,j}] - \frac{1}{3}\delta_{ij} \tag{B.25}$$

Using the input spectrum obtained from the DNS, the components of B_{ij} were evaluated for 300 000 KS realizations. It was observed for the resulting distributions of B_{ij}, that the upper bound on the 99% confidence interval, for any component, did not exceed 0.0122, which compares favourably with the large-scale anisotropy of 0.01 reported for decaying DNS in Elghobashi & Trusedell (1992).

Appendix C

Particle Tracking Verification

C.1 Timestep independence for DNS

For the fourth-order Adams-Bashforth explicit solver, convergence occurs for a sufficiently small timestep, Δt. Generally speaking, the timestep should be smaller than the smallest timescale of fluid velocity variations experienced by a particle.

Two groups of simulations with identical initial conditions for the particles (and identical DNS flow fields) were carried out; one group employed $\Delta t = 0.001 (< 0.01\tau_\eta)$, and the other group, $\Delta t = 0.0005$. It was observed that between the two cases, the dispersion results were virtually indistinguishable (see Fig. C.1). Since particle inertia has the effect of filtering out the shortest timescales of the turbulent velocity signal, this criterion was deemed sufficient for confidence in inertial particle statistics as well.

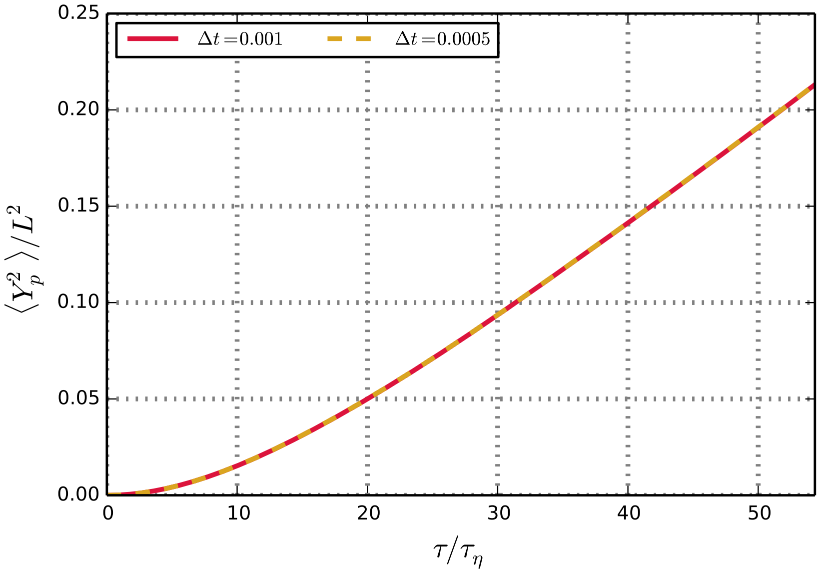

Figure C.1: Dispersion for fluid tracers in DNS, for time steps $\Delta t = 0.0005$ and $\Delta t = 0.001$.

C.2 Timestep independence in KS (with DNS spectrum input)

The $\Delta t < 0.01\tau_\eta$ criterion was also applied for the KS in Ch. 4, though of course τ_η is understood as being a property of the corresponding DNS - naturally τ_η depends on the dissipation, ϵ, and of course there is no dissipation in kinematic fields. Therefore it must be proven that the $\Delta t < 0.01\tau_\eta$ criterion is sufficient for timestep independence in KS. The dispersion of tracers in steady KS is shown in Fig. C.2, for $\Delta t = 0.005$ and $\Delta t = 0.001$. The results are virtually identical, indicating that this criterion is appropriate for the KS in Ch. 4.

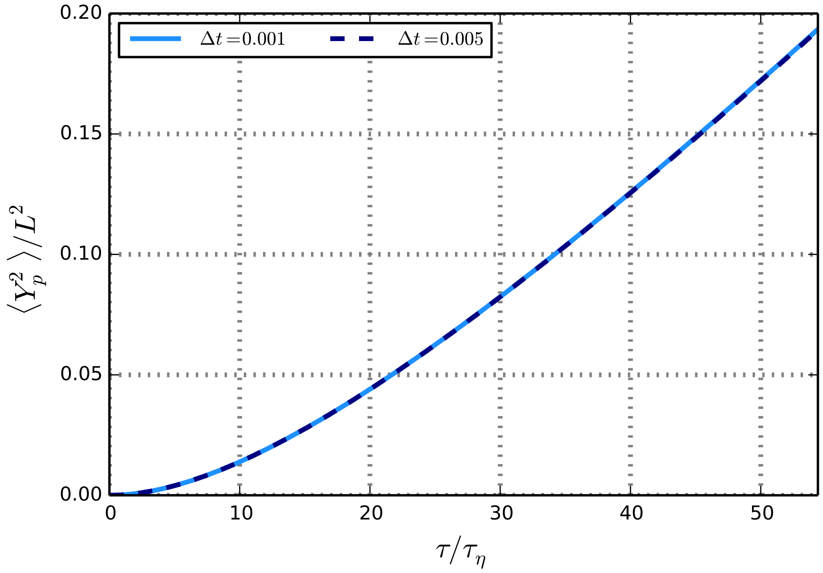

Figure C.2: Dispersion for tracers in steady KS, for time steps $\Delta t = 0.005$ and $\Delta t = 0.001$.

C.3 Timestep independence in a generalized KS method

For a generalized KS method for an arbitrary input spectrum (characterized by $u_{rms}, \tilde{\kappa}_1$ and $\tilde{\kappa}_N$ - see Fig. 5.1), some other sufficient condition is needed. Using a modified version of the criterion given in Thomson & Devenish (2005), it is hypothesized that confidence in Lagrangian statistics is granted if:

$$\Delta t \leq 0.01 \frac{1}{u_{rms}\tilde{\kappa}_1} \tag{C.1}$$

Generally speaking, the smaller the timescales of the flow, the smaller the timestep must be to ensure timestep independence. Therefore, testing criterion (C.1) with a very large $\tilde{\kappa}_N$ will demonstrate sufficiency for timestep independence, regardless of

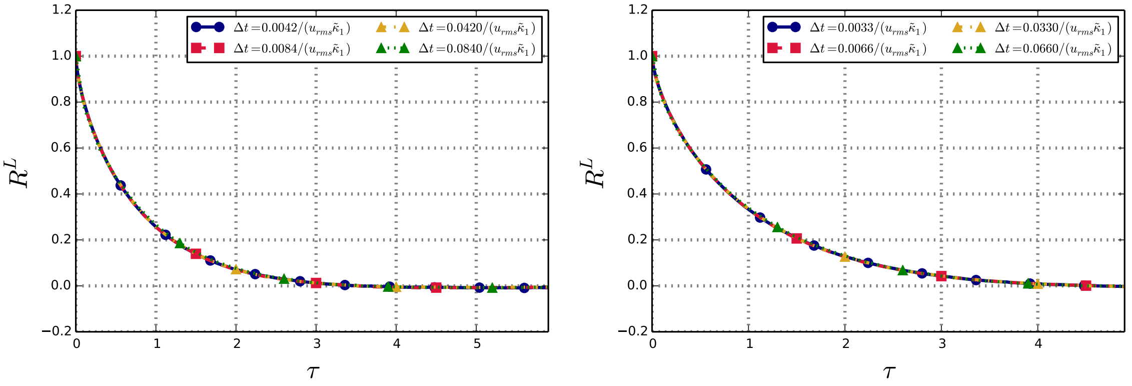

(a) $u_{rms} = 0.105, \tilde{\kappa}_1 = 8, \tilde{\kappa}_N = 80000$ (b) $u_{rms} = 0.085, \tilde{\kappa}_1 = 7.76, \tilde{\kappa}_N = 77600$

Figure C.3: Autocorrelation for KS, whose input spectra are detrained by input u_{rms}, $\tilde{\kappa}_1$ and $\tilde{\kappa}_N$.

$\tilde{\kappa}_N$. This criterion was tested for a two $u_{rms} - \tilde{\kappa}_1$ pairs (with $\tilde{\kappa}_N/\tilde{\kappa}_1 = 10^4$), and the autocorrelations are presented in Fig. C.3. The close match of the autocorrelations grants confidence that criterion (C.1) is appropriate.

C.4 Gravity

In the Lagrangian particle momentum equation (2.9), there exists a body force, **F**, which, in many real-world applications, arises due to gravity. For inertial particles, simulations were carried out with and without gravity. When comparing to the experimental benchmark (Snyder & Lumley (1971), as was done in Sec. 5.2), **F** was given the usual form:

$$\mathbf{F} = (0 \text{ m s}^{-2}, 0 \text{ m s}^{-2}, -9.81 \text{ m s}^{-2}) \tag{C.2}$$

For the DNS-KS comparison, one group of simulations was run without gravity, but another with gravity, to observe whether KS can reproduce the continuity effect. A sufficient condition for the observation of the continuity effect (Wells & Stock (1983)) is that the drift (terminal) velocity of a given inertial particle type exceeds the root mean squared turbulent fluctuating velocity (u_{rms}). Therefore, in order to test for the continuity effect in KS, gravity must be sufficiently strong such that the magnitude of the drift (terminal) velocity of the inertial particles exceeds u_{rms}. To find this critical acceleration, it is observed that for an ensemble of inertial particles traveling at a constant drift velocity (whose magnitude is u_d) due to acceleration, (2.9) becomes:

$$0 = \frac{f}{\tau_p}(0 - u_d) + g \tag{C.3}$$

where g is the magnitude of the body force vector. For a given u_d, (2.6), (2.7) and (2.8) are then used (along with the assumption that $|\mathbf{u}_f - \mathbf{u}_p| = u_d$) to solve for a corresponding acceleration (g) that yields this terminal velocity:

$$g = \frac{18 u_d \nu}{d_p^2(\rho_p/\rho_f)}\left[1 + 0.15\left(\frac{d_p u_d}{\nu}\right)^{0.687}\right] \tag{C.4}$$

For all simulations in question, a choice of $u_d = 0.1$ was sufficient to satisfy the $u_d > u_{rms}$ criterion. It is noted that the imposed body force will vary according to St.

In Sec. 5.2.2, the reverse calculation was done; equation (C.4) was used to find u_d based on a known acceleration ($g = 9.81$ m s^{-1}). This was part of the methodology for the replication of the results of Snyder & Lumley (1971) with TLKS, for which the terminal velocity of each particle was calculated *a priori*. This was done to match the initial *timestep* for the evaluation of Lagrangian statistics (t^*) with the “first camera” *position* in the original experiment.

C.5 Choice of initial time step

The discussion regarding an appropriate choice of initial timestep for evaluation of Lagrangian statistics is facilitated by the concept of the root mean-squared relative velocity, defined as:

$$u_{rel}(t) = \langle |\mathbf{u}_p(t) - \mathbf{u}_f(\mathbf{x}_p(t), t)|^2 \rangle^{1/2} \tag{C.5}$$

This quantity is simply zero for tracers (since the tracer velocity *is* the local fluid velocity), and is generally nonzero for inertial particles due to the crossing-trajectories effect. At the start of all particle tracking simulations, all particles were simply assigned the local fluid velocity (for either DNS or KS). While this initial condition is sensible for tracers (for the reason just mentioned), the mean-squared relative velocity is expected to converge to a stable equilibrium in stationary flow.

When particles are released into the flow field, a certain period must pass before the particle statistics become independent of their initial conditions. Similar to the approach employed in Strutt *et al.* (2011) and Cernick (2013), three rounds of simulations were carried out, all with the following choices of initial conditions:

- $\mathbf{u}_p(t = 0) = 0$
- $\mathbf{u}_p(t = 0) = \mathbf{u}_f(\mathbf{x}_p(0), 0)$
- $\mathbf{u}_p(t = 0) = 2\mathbf{u}_f(\mathbf{x}_p(0), 0)$

The time at which the various statistics become indistinguishable for all three initial conditions is denoted t^*. The values of t^*, for a variety of particle types, both with and without gravity were determined. Naturally larger-St particles generally exhibit a longer t^*, since such particles take longer to react to changes in the fluid velocity field. Higher St particles require longer to forget their initial conditions. Gravity had the effect of reducing the time needed to achieve independence. The higher $t^\star$ for $St \sim 1$ than $St \sim 0.5$ in the gravity case appears anomalous - since $t^\star$ is based on a *minimum* time at which particles have forgotten their initial conditions, it was elevated in both cases as a precaution; to 0.4 and 0.3 for the $St \sim 0.5$ and $St \sim 1$ cases respectively.

St		0.5	1	2	10
t^*	Without gravity	0.34	0.60	1.23	4.04
	With gravity	0.37	0.23	0.58	2.62

Table C.6: t^* (time for which Lagrangian statistics become independent of initial conditions), for a variety of particle types, both with and without gravity

C.6 Method for calculation of asymptotic correlation dimension

In Sec. 2.2.6, it was noted that the applicability of a dynamical systems treatment of preferential concentration suggests the existence of an asymptotic correlation dimension, and that the history exhibits a decaying exponential behaviour. In Fig. C.4, the history of correlation dimension for each particle type is shown. In contrast to the Lagrangian statistics, the history is displayed from the very start of the simulation, rather than waiting until t^*.

It appears that, particularly for the low St cases, $\mathcal{D}_2$ exhibits a decaying exponential behaviour (beyond an initial transient). Beyond t^*, the exponential of best fit

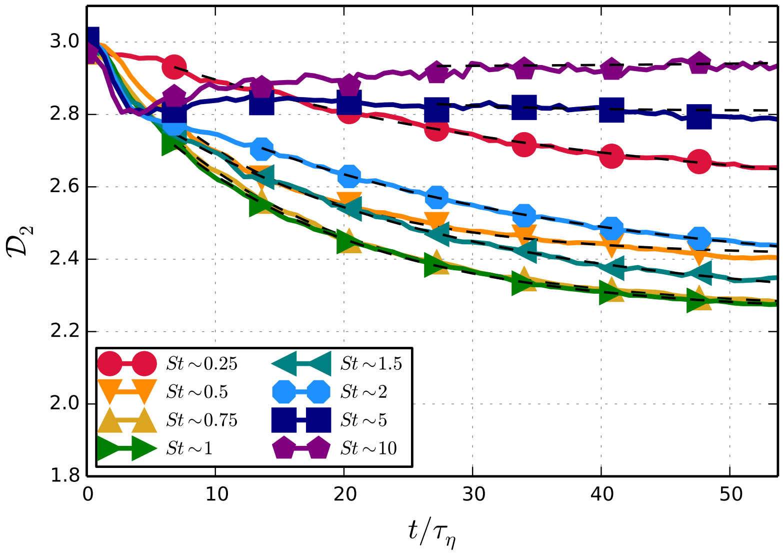

Figure C.4: History of correlation dimension, for all inertial particle types in DNS, without gravity. The black dashed lines indicate exponentials of best fit.

was found, according to the general form:

$$Ae^{-B\tau} + \overline{\mathcal{D}}_2 \tag{C.6}$$

where $\overline{\mathcal{D}}_2$ represents the asymptotic value. The dashed lines in Fig. C.4 represent these functions of best fit, and, for low St, agreement is very good. Good agreement for high St is not achieved, because in such cases the initial transient is longer. Since the function fit occurs over a small interval, it is highly prone to error, in which case the method is deemed indeterminate. It is, however, precisely in such cases that significant clustering is not expected to have occurred, and the asymptotic correlation dimension is taken as the final value of an appropriately smoothed $\mathcal{D}_2$ history.

Appendix D

Verification of KS

D.1 Pairwise dispersion

KS (as described in 2.2.4 and 3.2) was applied with an input spectrum based on the DNS spectrum of Yeung (1994), in an effort to replicate the KS results of Malik & Vassilicos (1999). The pairwise dispersion results, along with the results of Malik & Vassilicos (1999) are shown in Fig. D.1. Agreement is very good, though not exact - the discrepancy likely arises from slightly differing methods of converting the discrete DNS output spectra as input for KS, particularly in the largest scales (smallest wavenumbers).

D.2 Verification of Type II KS

A verification of the "inner domain" method of sampling particles for Type II KS (described in 3.3) is given here. The number of particles in the inner subdomain is shown for $St \sim 10$ particles in Type II KS (see Fig. D.2a) - $St \sim 10$ inertial particles,

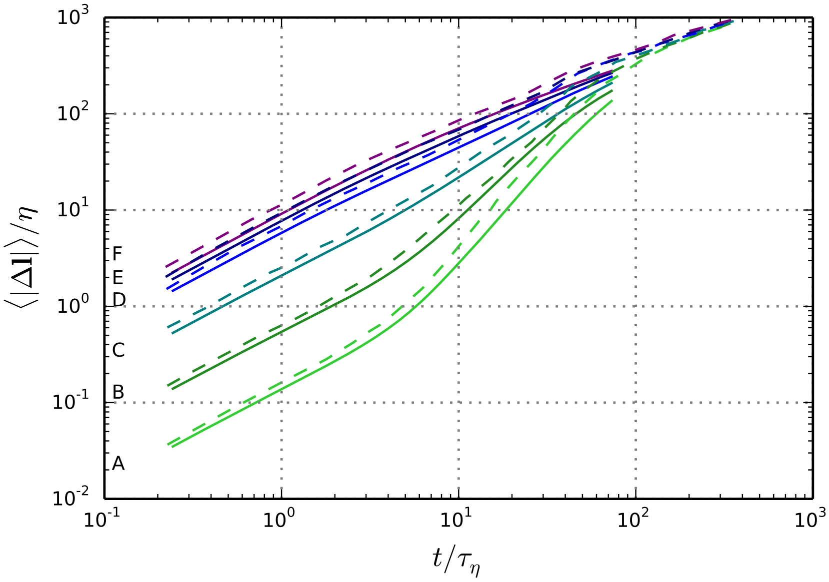

Figure D.1: Growth in pairwise separation for steady ($\lambda = 0$) KS, from the KS solver as described in 2.2.4 and 3.2 (solid lines). The results of Malik & Vassilicos (1999) are given as dashed lines. Lines A-F correspond to initial separations of $l_0/\eta = 0.25, 1, 4, 16, 32, 64$ respectively.

because such particles exhibit maximal dispersion and would soonest exhibit particle "bleed" (see Sec. 3.3). $N_p(t)$ decreases about 10% from the expected value of 50000, indicating that, in the worst case, some bleed does occur. The corresponding case for $St \sim 10$ particles in gravity is shown in Fig. D.2b, and the bleed amounts to about 2%. The dispersion for $St \sim 10$ inertial particles in Types I and II KS without gravity is shown in Fig. D.2a, and with gravity in D.2b. Particles require an initial development to forget their initial conditions, and this interval depends on whether or not gravity is present (see Sec. C.5), hence the interval lengths are different in the two cases. In either case, the curves are virtually indistinguishable, indicating that, despite the slight particle bleed, statistics are independent of the method of sampling particles for Type II KS.

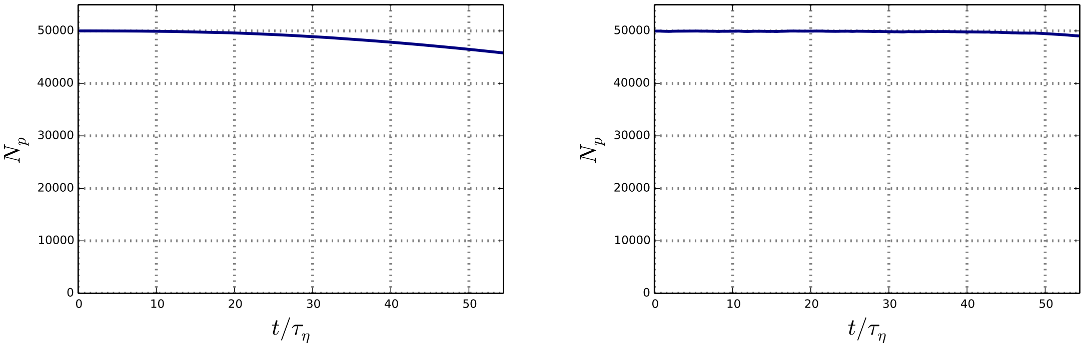

(a) Without gravity (b) With gravity

Figure D.2: Number of particles in inner subdomain vs time (for steady Type II KS), for $St \sim 10$ inertial particles, without gravity.

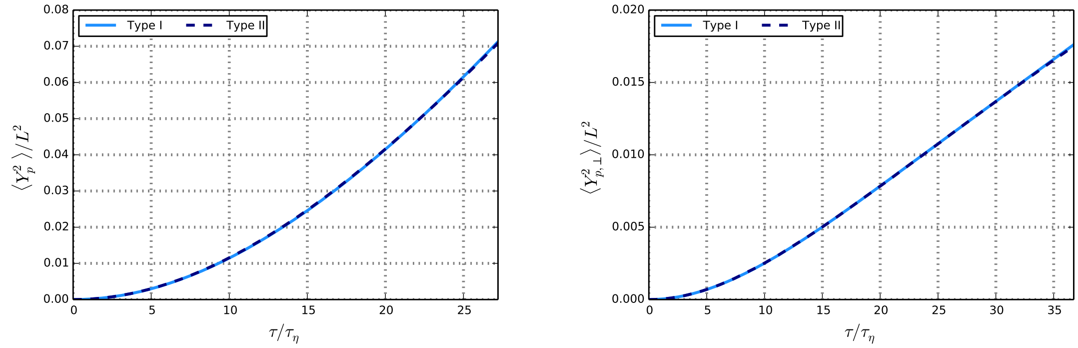

(a) Without gravity (b) With gravity

Figure D.3: Dispersion of $St \sim 10$ inertial particles in steady ($\lambda = 0$) KS, for Type I KS (unbounded domain) and Type II KS (bounded domain).

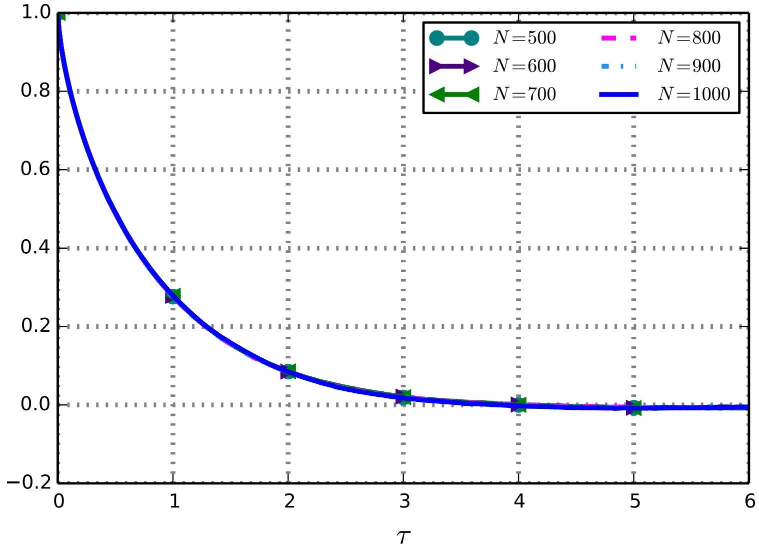

Figure D.4: Lagrangian autocorrelation for steady KS with $u_{rms} = 1.05, \tilde{\kappa}_1 = 7.5, \tilde{\kappa}_N = 75000$, with varying N_κ (number of KS modes).

D.3 Independence of statistics from number of KS modes

In a given realization of KS, the Lagrangian output statistics are affected by the mutual orientation of the KS modes. Hence a sufficiently large number of KS modes is required to ensure isotropy, as well as general confidence in Lagrangian statistics. For the simulations described in Sec. 5.1.1, a variety of simulations were run with a varying number of KS modes - the Lagrangian autocorrelation is shown in Fig. D.4. While differences in the autocorrelation are not readily discernible, the Lagrangian integral timescale is the integral of the autocorrelation (by (2.25)), and, as such, even very slight differences in the autocorrelation can be magnified in the difference of timescales. In Fig. D.5, T_L is given as a function of N_κ, and it appears that $N_\kappa = 1000$ was sufficient for granting confidence in T_L.

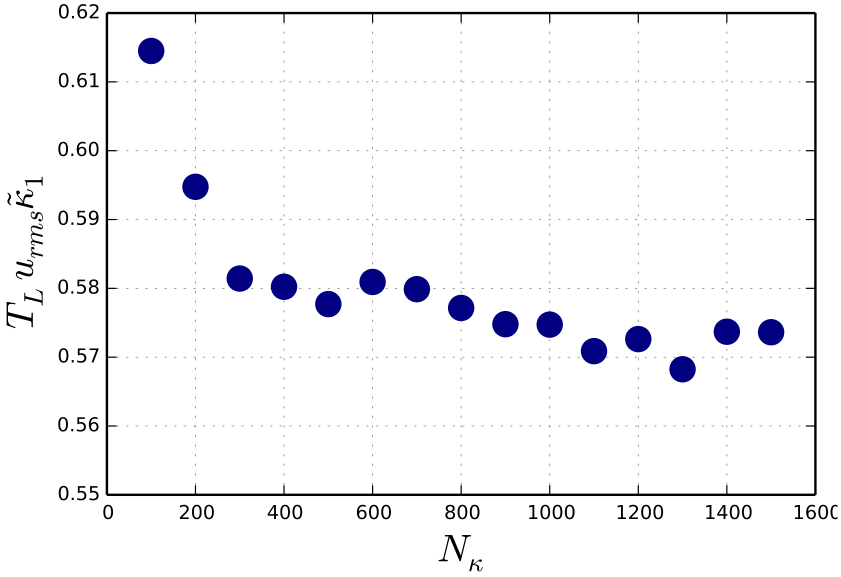

Figure D.5: Non-dimensionalized Lagrangian integral timescale vs N_κ, with $u_{rms} = 1.05, \tilde{\kappa}_1 = 7.5$, and $\tilde{\kappa}_N = 75000$.

Bibliography

Armenio, V. & Fiorotto, V. 2001 The importance of the forces acting on particles in turbulent flows . *Phys. Fluids* **13** (8), 2437–2440.

Arnold, V. 1965 Sur la topologie des écoulements stationnaires des fluides parfaits. *Comptes rednues hebdomidaires des séances de l'académie des sciences* **261** (1), 17.

Basset, A. B. 1888 *A treatise on Hydrodynamics. Vol. 1*. Ecole Polytechnique Federale de Lausanne.

Batchelor, G. K. 1953 *The theory of homogeneous turbulence*. Cambridge university press.

Bec, J. 2005 Multifractal concentrations of inertial particles in smooth random flows. *Journal of Fluid Mechanics* **528**, 255–277.

Bec, J., Biferale, L., Cencini, M., Lanotte, A., Musacchio, S. & Toschi, F. 2007*a* Heavy Particle Concentration in Turbulence at Dissipative and Inertial Scales. *Physical Review Letters* **98** (8).

Bec, J., Cencini, M. & Hillerbrand, R. 2007*b* Heavy particles in incompressible flows: the large stokes number asymptotics. *Physica D: Nonlinear Phenomena* **226** (1), 11–22.

BOCKSELL, T. L. & LOTH, E. 2006 Stochastic modeling of particle diffusion in a turbulent boundary layer. *International Journal of Multiphase Flow* **32** (10-11), 1234–1253.

BOUSSINESQ, J. 1903 *Théorie analytique de la chaleur*, , vol. 2. Gauthier-Villars, Paris, France.

BUEVICH, Y. A. 1966 Motion resistance of a particle suspended in a turbulent medium . *Mekhanika Zhidkosti i Gaza* **1** (6), 119.

CERNICK, M. 2013 *Particle subgrid scale modeling in large-eddy simulation of particle-laden turbulence*. Master's Thesis, McMaster University.

CERNICK, M. J., TULLIS, S. & LIGHTSTONE, M. 2015 Particle subgrid scale modelling in large-eddy simulations of particle-laden turbulence. *Journal of Turbulence* **16** (2), 101–135.

CHEN, L., GOTO, S. & VASSILICOS, J. 2006 Turbulent clustering of stagnation points and inertial particles. *Journal of Fluid Mechanics* **553** (1), 143–154.

CHEN, S., DOOLEN, G. D., KRAICHNAN, R. H. & SHE, Z.-S. 1993 On statistical correlations between velocity increments and locally averaged dissipation in homogeneous turbulence. *Physics of Fluids A: Fluid Dynamics* **5**, 458.

CLIFT, R., GRACE, J. & WEBER, M. 1978 Bubbles, drops & particles. *Academic, New York* pp. 171–202.

COLEMAN, S. W. & VASSILICOS, J. C. 2009 A unified sweep-stick mechanism to explain particle clustering in two- and three-dimensional homogeneous, isotropic turbulence. *Physics of Fluids* **21** (11), 113301.

CORRSIN, S. & LUMLEY, J. 1956 On the equation of motion for a particle in turbulent fluid . *Appl. Sci. Res.* **6**, 114 –116.

CSANADY, G. T. 1963 Turbulent diffusion of heavy particles in the atmosphere. *J. of the Atm. Sci.* **20**, 201– 208.

DEHBI, A. 2011 Prediction of extrathoracic aerosol deposition using rans-random walk and les approaches. *Aerosol Sci. and Tech.* **45** (5), 555 569.

ELGHOBASHI, S. 1994 On predicting particle-laden turbulent flows. *App. Sci. Res.* **52**, 309–329.

ELGHOBASHI, S. & TRUSEDELL, G. C. 1992 Direct simulation of particle dispersion in a decaying isotropic turbulence. *J. Fluid Mech.* **242**, 655– 700.

ESWARAN, V. & POPE, S. 1988 An examination of forcing in direct numerical simulations of turbulence. *Computers & Fluids* **16** (3), 257–278.

EYINK, G. L. & BENVENISTE, D. 2012 Do sweeping effects suppress particle dispersion in synthetic turbulence? *arXiv preprint arXiv:1208.3497* .

FESSLER, J. R., KULICK, J. D. & EATON, J. K. 1994 Preferential concentration of heavy particles in a turbulent channel flow. *Phys. Fluids* **6**, 3742–3749.

FLOHR, P. & VASSILICOS, J. 2000 A scalar subgrid model with flow structure for large-eddy simulations of scalar variances. *Journal of Fluid Mechanics* **407**, 315–349.

FRISCH, U. 1995 *Turbulence: the legacy of AN Kolmogorov*. Cambridge university press.

Fung, J., Hunt, J., Malik, N. A. & Perkins, R. 1992 Kinematic simulation of homogeneous turbulence by unsteady random fourier modes. *Journal of Fluid Mechanics* **236** (1), 281–318.

Fung, J. & Vassilicos, J. 1998 Two-particle dispersion in turbulentlike flows. *Physical Review E* **57** (2), 1677–1690.

Gosman, A. D. & Ioannides, E. 1983 Aspects of computer simulation of liquid-fueled combustors. *Journal of Energy* **7**.

Goto, S. & Vassilicos, J. 2006 Self-similar clustering of inertial particles and zero-acceleration points in fully developed two-dimensional turbulence. *Physics of Fluids* **18**, 115103.

Goto, S. & Vassilicos, J. 2008 Sweep-stick mechanism of heavy particle clustering in fluid turbulence. *Physical review letters* **100** (5), 54503.

Grassberger, P. & Procaccia, I. 2004 Measuring the strangeness of strange attractors. In *The Theory of Chaotic Attractors*, pp. 170–189. Springer.

Hennick, E. A. & Lightstone, M. F. 2000 A comparison of stochastic separated flow models for partice dispersion in turbulent flows. *Energy & Fuels* **14**, 95 – 103.

Ijzermans, R. H., Meneguz, E. & Reeks, M. W. 2010 Segregation of particles in incompressible random flows: singularities, intermittency and random uncorrelated motion. *Journal of Fluid Mechanics* **653**, 99–136.

Khan, M. & Vassilicos, J. 2003 A new eulerian–lagrangian length-scale in turbulent flows. *Physics of Fluids (1994-present)* **16** (1), 216–218.

Khan, M. A. I., Luo, X., Nicolleau, F., Tucker, P. & Iacono, G. 2010 Effects of LES sub-grid flow structure on particle deposition in a plane channel with a ribbed wall. *International Journal for Numerical Methods in Biomedical Engineering* **26**, 999–1015.

Kraichnan, R. H. 1970 Diffusion by a random velocity field. *Physics of Fluids* **13** (1), 22–31.

Lien, R.-C., D'ASARO, E. A. & Dairiki, G. T. 1998 Lagrangian frequency spectra of vertical velocity and vorticity in high-reynolds-number oceanic turbulence. *Journal of Fluid Mechanics* **362**, 177–198.

Lightstone, M. 2007 Self-consistency and the use of correlated stochastic separated flow models for prediction of particle-laden flows. *Int. J. CFD* **21** (9-10), 329–334.

Lu, Q. Q., Fontaine, J. R. & Aubertin, G. 1993 A Lagrangian Model for Solid Particles in Turbulent Flows . *Int. J. of Multi. Phys.* **19**, 347–367.

MacInnes, J. M. & Bracco, F. V. 1992 Stochastic particle dispersion modeling and the tracer-particle limit. *Phys. Fluids A* **4** (12), 28092824.

Malik, N. A. 1991 *Studies In Turbulent Dispersion Using Kinematic Simulation*. PhD Thesis, University of Cambridge.

Malik, N. A. 1996 Structural diffusion in 2d and 3d random flows. In *Advances In Turbulence VI* (ed. S. Gavrilakis, L. Machiels & P. A. Monkewitz), pp. 619–620. Kluwer Academic Publishers.

Malik, N. A. 2014 Turbulent particle pair diffusion, locality versus non-locality: Numerical simulations. *arXiv preprint arXiv:1405.3638* .

Malik, N. A. & Vassilicos, J. C. 1999 A Lagrangian model for turbulent dispersion with turbulent-like flow structure: Comparison with direct numerical simulation for two-particle statistics. *Physics of Fluids* **11**, 1572–1580.

Maxey, M. R. & Riley, J. J. 1983 Equation of motion for a small rigid sphere in nonuniform flow . *Phys. fluids* **26** (4), 883–889.

Mei, R., Adrian, R. J. & Hanratty, T. J. 1991 Particle dispersion in isotropic turbulence under Stokes drag and Basset force with gravitational settling . *JFM* **6**, 114 –116.

Monchaux, R., Bourgin, M. & Cartellier, A. 2012 Analyzing preferential concentration and clustering of inertial particles in turbulence. *Int. J. Multiphase Flow* **40**, 1–18.

Monin, A. & Yaglom, A. 1975 Statistical fluid mechanics: Mechanics of turbulence, vol. 2, 874 pp.

Mordant, N., Metz, P., Michel, O. & Pinton, J.-F. 2001 Measurement of lagrangian velocity in fully developed turbulence. *Physical Review Letters* **87** (21), 214501.

Murakami, S., Kato, S., Nagano, S. & Tanaka, S. 1992 Turbulence modeling for cfd. *ASHRAE transactions* **98**, 82–97.

Nicolleau, F. & Abou El-Azm Aly, A. 2012 Can kinematic simulation predict richardson's regime? **18**, 43–57.

Nicolleau, F. & Vassilicos, J. 2003 Turbulent pair diffusion. *Physical review letters* **90** (2), 024503.

Oesterlé, B. & Zaichik, L. I. 2004 On Lagrangian time scales and particle dispersion modeling in equilibrium turbulent shear flows. *Physics of Fluids* **16**, 3374–3384.

Osborne, D., Vassilicos, J. & Haigh, J. 2005 One-particle two-time diffusion in three-dimensional homogeneous isotropic turbulence. *Physics of Fluids* **17** (3), 035104.

Osborne, D., Vassilicos, J., Sung, K. & Haigh, J. 2006 Fundamentals of pair diffusion in kinematic simulations of turbulence. *Physical Review E* **74** (3), 036309.

Oseen, C. W. 1927 *Hydrodynamik*. Akademische Verlagsgesellschaft, Leipzig, Germany.

Posner, J. D., Buchanan, C. R. & Dunn-Rankin, D. 2005 Measurement and prediction of indoor air flow in a model room. *Energy and Buildings* **35**, 515–526.

Reeks, M. 1977 On the dispersion of small particles suspended in an isotropic turbulent fluid. *Journal of fluid mechanics* **83** (03), 529–546.

Shotorban, B. & Balachandar, S. 2007 A eulerian model for large-eddy simulation of concentration of particles with small stokes numbers. *Phys. Fluids* **19**, 118107–1.

Snyder, W. & Lumley, J. L. 1971 Some measurements of particle velocity autocorrelation functions in a turbulent flow. *J Fluid Mech* **48**, 41–71.

Squires, K. D. & Eaton, J. K. 1990 Particle response and turbulence modification in isotropic turbulence. *Physics of Fluids* **2**, 1191–1203.

Squires, K. D. & Eaton, J. K. 1991 Measurements of particle dispersion obtained from direct numerical simulations of isotropic turbulence. *Journal of Fluid Mechanics* **226**, 1–35.

Strutt, H., Tullis, S. & Lightstone, M. 2011 Numerical methods for particle-laden dns of homogeneous isotropic turbulence. *Computers & Fluids* **40** (1), 210–220.

Taylor, G. I. 1921 Diffusion by continuous movements. *Proc. London. Math. Soc.* **20**, 196 – 212.

Tchen, C. M. 1947 *Mean value and correlation problems connected with the motion of small particles suspended in a turbulent fluid*. PhD Thesis, University of Delft.

Tennekes, H. 1975 Eulerian and lagrangian time microscales in isotropic turbulence. *Journal of Fluid Mechanics* **67** (03), 561–567.

Tennekes, H. & Lumley, J. L. 1972 *A first course in turbulence*. MIT press.

Thomson, D. 1984 Random walk modelling of diffusion in inhomogeneous turbulence. *Quarterly Journal of the Royal Meteorological Society* **110** (466), 1107–1120.

Thomson, D. 1987 Criteria for the selection of stochastic models of particle trajectories in turbulent flows. *Journal of Fluid Mechanics* **180**, 529–556.

Thomson, D. & Devenish, B. 2005 Particle pair separation in kinematic simulations. *Journal of Fluid Mechanics* **526**, 277–302.

Townsend, A. A. 1980 *The structure of turbulent shear flow*. Cambridge University Press.

TURFUS, C. & HUNT, J. 1987 A stochastic analysis of the displacements of fluid elements in inhomogeneous turbulence using kraichnans method of random modes. In *Advances in turbulence*, pp. 191–203. Springer.

WANG, L.-P. & MAXEY, M. R. 1993 Settling velocity and concentration distribution of heavy particles in homogeneous isotropic turbulence. *Journal of Fluid Mechanics* **256**, 27–68.

WANG, L.-P. & STOCK, D. E. 1993 Dispersion of Heavy Particles by Turbulent Motion. *Journal of Atmospheric Sciences* **50**, 1897–1913.

WELLS, M. R. & STOCK, D. E. 1983 The effects of crossing trajectories on the dispersion of particles in a turbulent flow. *Journal of Fluid Mechanics* **136**, 31–62.

YEUNG, P. 1994 Direct numerical simulation of two-particle relative diffusion in isotropic turbulence. *Physics of Fluids (1994-present)* **6** (10), 3416–3428.

YEUNG, P. K. & POPE, S. B. 1988 An algorithm for tracking fluid particles in numerical simulations of homogeneous turbulence. *J. Comput. Phys.* **79**, 373–416.

ZHAO, B., LI, X. & ZHANG, Z. 2005 Numerical study of particle deposition in two differently ventilated rooms. *Indoor and Built Env.* **13**, 443451.

ZHAO, B., YANG, C., YANG, X. & LIU, S. 2008 Particle dispersion and deposition in ventilated rooms: Testing and evaluation of different eulerian and lagrangian models. *Building and Env.* **43**, 388397.

ZHOU, Q. & LESCHZINER, M. A. 1991 A lagrangian particle dispersion model based on a time-correlated stochastic approach. , vol. 121, pp. 255–260.